

# **Surface passivation of crystalline silicon solar cells by amorphous silicon films**

Von der Fakultät für Mathematik und Physik  
der Gottfried Wilhelm Leibniz Universität Hannover

zur Erlangung des Grades

Doktor der Naturwissenschaften

Dr. rer. nat.

genehmigte Dissertation

von

Dipl.-Phys. Heiko Plagwitz

geboren am 03.02.1977 in Fürth

2007

Referent: Prof. Dr. Rolf Brendel  
Korreferent: Prof. Dr. Michael Oestreich  
Tag der Promotion: 11.07.2007

# Abstract

The energy conversion efficiency of high-quality crystalline silicon (c-Si) solar cells is mainly controlled by the recombination probability of photogenerated carrier pairs at the surfaces. The deposition of intrinsic, hydrogenated amorphous silicon (a-Si:H), results in the same excellent passivation of surface recombination centers as state-of-the-art thermal oxidation, but at a much lower process temperature that reduces both, energy consumption and the risk of impurity diffusion into the c-Si bulk. This work focuses on investigating the physical properties of carrier recombination centers at the interface between amorphous and crystalline silicon, and their impact on the performance of crystalline silicon solar cells that feature surface passivation by a-Si:H. Whereas the high quality of a-Si:H-passivation of lowly-doped c-Si surfaces is described in literature, this work shows the first-time surface passivation of highly-doped c-Si by amorphous silicon.

A defect model is developed that allows for a quantitative analysis of the passivation and formation of interface defects during illumination and thermal annealing, from measured surface recombination rates. The surface passivation by a-Si:H shows a light-induced degradation, that is reversible by thermal annealing. This degradation is due to the formation of dangling bond states at the a-Si:H/c-Si interface by the dissociation of weak Si-Si bonds, analogously to the Staebler-Wronski effect that is described in literature only for a-Si:H bulk material. The passivation reaches a stable state with the density of dangling bond defects being about an order of magnitude larger than in the initial state. The diffusivity of hydrogen atoms within the a-Si:H film is found to control the thermal stability of the surface passivation: Annealing of a-Si:H-passivated c-Si wafers at 300°C maintains the excellent passivation quality of as-deposited a-Si:H films, and restores their passivation quality after illumination, due to the re-arrangement of Si-H bonds which reduces the bulk and interface defect densities. In contrast, annealing at temperatures higher than 400°C leads to desorption of hydrogen atoms from the a-Si:H film, thus increasing the defect densities. An anti reflective SiN<sub>x</sub> capping layer applied on top of the passivating a-Si:H layer acts as a source of hydrogen atoms, thus reducing the rate of defect formation by a factor of 15 when compared to a-Si:H single-layer passivation.

The COSIMA technique for the formation of local contacts to a-Si:H-passivated solar cells by means of annealing at low temperatures  $T < 300^\circ\text{C}$  is developed, together with an analytic model that allows for the optimization of local contact layouts for minimum surface recombination and series resistance of solar cells. The optical properties of thin a-Si:H films are studied with respect to their impact on the energy conversion efficiency of solar cells that feature an a-Si:H-passivated front side. An optimum a-Si:H thickness of  $6.5\text{ nm} < d < 10\text{ nm}$  ensures both, optimum surface passivation and minimum absorption in the a-Si:H film. Finally, the results of this work are applied to fabricate solar cells that feature a-Si:H-passivation of the emitter and base, exceeding an energy conversion efficiency of 20%.

# Kurzzusammenfassung

Der Wirkungsgrad von Solarzellen aus hochwertigem kristallinem Siliziummaterial wird vor allem von der Rekombinationswahrscheinlichkeit für photogenerierte Ladungsträger an den Oberflächen bestimmt. Oberflächenrekombinationszentren lassen sich mittels einer Schicht aus intrinsischem, amorphem Silizium (a-Si:H) ebenso gut passivieren wie durch thermische Oxidation, dem Standardverfahren der Mikroelektronik. Der Vorteil der Oberflächenbeschichtung mit a-Si:H liegt jedoch in einer deutlich geringeren Prozesstemperatur, die zu einem reduzierten Energieverbrauch, sowie einem geringeren Risiko der Eindiffusion von Verunreinigungen in das Siliziumvolumen führt. Die vorliegende Arbeit befasst sich mit der Untersuchung der physikalischen Eigenschaften von Ladungsträgerrekombinationszentren an der Grenzfläche zwischen amorphem und kristallinem Silizium (c-Si), sowie deren Einfluss auf den Wirkungsgrad von Solarzellen, deren Oberfläche mit amorphem Silizium passiviert ist. Während die hohe Qualität der Oberflächenpassivierung für niedrigdotierte Siliziumsubstrate bereits in der Literatur beschrieben wurde, zeigt die vorliegende Arbeit die Anwendbarkeit von amorphem Silizium zur Passivierung von hochdotierten Siliziumoberflächen.

Im Rahmen der Arbeit wurde ein analytisches Modell entwickelt, das eine Bestimmung der Defektdichte an der a-Si:H/c-Si-Grenzfläche aus gemessenen Ladungsträger-Rekombinationsraten erlaubt. Die quantitative Auswertung der Defektkonzentration bei Beleuchtung zeigt eine lichtinduzierte Degradation der Oberflächenpassivierung mit a-Si:H, welche durch Erwärmen rückgängig gemacht werden kann. Grund für die Degradation ist die Zunahme der Dichte offener Bindungen an der Grenzfläche durch das Aufbrechen gestreckter Si-Si Bindungen analog zum Staebler-Wronski-Effekt, der jedoch bisher nur für das amorphe Silizium-Volumenmaterial beschrieben wurde. Die thermische Stabilität der a-Si:H-Passivierung beim Erhitzen wird durch die Diffusivität von Wasserstoffatomen in der a-Si:H-Schicht bestimmt: Erwärmen auf 300°C führt zum Absättigen noch vorhandener offener Siliziumbindungen durch Wasserstoffatome, sowohl an der Grenzfläche als auch im a-Si:H-Volumen. Deshalb bleibt die hervorragende Oberflächenpassivierung erhalten, und kann auch nach lichtinduzierter Degradation durch Tempern wiederhergestellt werden. Im Gegensatz dazu führt Erhitzen auf über 400°C zum Ausdiffundieren von Wasserstoff aus der a-Si:H-Schicht, und damit zum Anwachsen der Defektdichte. Durch das zusätzliche Abscheiden einer Siliziumnitridschicht, die sowohl als Wasserstoffquelle, als auch als Antireflexschicht dient, kann die Defektbildungsrate an der a-Si:H/c-Si-Grenzfläche um den Faktor 15 verringert werden.

Darüberhinaus wurde das COSIMA-Verfahren (contact formation to a-Si:H-passivated solar cells by means of annealing) zur lokalen Kontaktierung a-Si:H-passivierter Solarzellen bei Prozesstemperaturen unter 300°C entwickelt, sowie ein analytisches Modell zur Optimierung der Geometrie lokaler Kontakte, um sowohl eine geringe Oberflächenrekombinationsrate, als auch geringen Serienwiderstand der fertigen Solarzelle zu erreichen. Die optischen Eigenschaften dünner Schichten amor-



phen Siliziums, speziell deren Einfluss auf den Wirkungsgrad a-Si:H-passivierter Solarzellen, wurden untersucht. Die optimale Schichtdicke im Bereich von  $6.5 \text{ nm} < d < 10 \text{ nm}$  gewährleistet sowohl optimale Oberflächenpassivierung, als auch minimale parasitäre Absorption des einfallenden Lichts. Schließlich wurden die Ergebnisse der vorliegenden Arbeit zur Herstellung von Solarzellen mit Wirkungsgraden über 20% angewendet.

**Schlagwörter:** Silizium, Oberflächenpassivierung, Ladungsträgerlebensdauer  
**Keywords:** silicon, surface passivation, carrier lifetime



# Contents

<b>1</b>	<b>Introduction</b>	<b>11</b>
<b>2</b>	<b>Carrier recombination in silicon solar cells</b>	<b>15</b>
2.1	Definitions . . . . .	15
2.2	Bulk recombination . . . . .	16
2.2.1	Radiative band-to-band recombination . . . . .	17
2.2.2	Auger recombination . . . . .	17
2.2.3	Recombination through defects . . . . .	18
2.3	Surface recombination . . . . .	20
2.3.1	Recombination through surface states . . . . .	20
2.3.2	Effective surface recombination velocity . . . . .	21
2.4	Measurement of the effective carrier lifetime . . . . .	22
2.5	Diode saturation current . . . . .	25
2.5.1	Determination of base and emitter saturation current . . . . .	26
2.5.2	Contributions to the emitter saturation current . . . . .	27
2.6	Analytic model for the base saturation current of locally contacted cells . . . . .	29
2.6.1	Definition of the problem . . . . .	29
2.6.2	Previous work: small-scale case . . . . .	31
2.6.3	Parallel-diode approximation: large-scale case . . . . .	34
2.6.4	Model for the base series resistance . . . . .	37
2.6.5	Interpolation between small-scale case and large-scale case . . . . .	44
2.6.6	Conclusion . . . . .	48
<b>3</b>	<b>A-Si:H-passivation and contact formation to solar cells: COSIMA</b>	<b>51</b>
3.1	Deposition parameters . . . . .	51
3.2	COSIMA contact formation . . . . .	55
3.2.1	Aluminum-induced crystallization of amorphous silicon . . . . .	55
3.2.2	Microstructure of COSIMA contacts . . . . .	56
3.2.3	Contact resistivity . . . . .	60
3.2.4	Discussion . . . . .	63
3.3	Saturation current of the COSIMA-processed base . . . . .	64

3.3.1	Experimental determination of the saturation current . . . .	65
3.3.2	Comparison to theory . . . . .	67
3.4	Summary . . . . .	70
<b>4</b>	<b>Surface passivation by a-Si:H single- and a-Si:H/SiN<sub>x</sub> double-layers</b>	<b>71</b>
4.1	Optimum thickness of the a-Si:H film . . . . .	71
4.1.1	A-Si:H single layer passivation . . . . .	72
4.1.2	A-Si:H/SiN <sub>x</sub> double layer passivation . . . . .	73
4.1.3	Discussion . . . . .	74
4.2	Passivation of diffused emitters . . . . .	75
4.2.1	Sample preparation . . . . .	76
4.2.2	Passivation of phosphorus-diffused emitters . . . . .	77
4.2.3	Passivation of boron-diffused emitters . . . . .	79
4.2.4	Stability under UV irradiation . . . . .	81
4.3	Passivation of textured surfaces . . . . .	83
4.3.1	Contributions to the surface recombination rate . . . . .	83
4.3.2	Passivation of lowly-doped surfaces . . . . .	85
<b>5</b>	<b>Model of the a-Si:H/c-Si heterojunction</b>	<b>89</b>
5.1	The heterostructure simulation package AFORS-HET . . . . .	89
5.2	Model of the a-Si:H bulk defects . . . . .	91
5.2.1	Distribution function of the density of states . . . . .	91
5.2.2	Carrier capture cross sections . . . . .	97
5.3	Model of the a-Si:H/c-Si interface defects . . . . .	98
5.3.1	Distribution function of the density of states . . . . .	98
5.3.2	Carrier capture cross sections . . . . .	101
<b>6</b>	<b>Stability under illumination: Staebler-Wronski effect</b>	<b>103</b>
6.1	Experimental . . . . .	103
6.1.1	A-Si:H single layer passivation . . . . .	104
6.1.2	A-Si:H/SiN <sub>x</sub> double layer passivation . . . . .	105
6.1.3	Discussion . . . . .	106
6.2	Formation of defects during illumination . . . . .	108
6.2.1	Prerequisites . . . . .	108
6.2.2	Results and discussion . . . . .	109
6.3	Summary . . . . .	115
<b>7</b>	<b>Thermal stability</b>	<b>117</b>
7.1	Passivation of lowly-doped surfaces . . . . .	117
7.1.1	Results . . . . .	117
7.1.2	Discussion . . . . .	118

---

7.2	Formation of defects during annealing . . . . .	119
7.2.1	Results . . . . .	119
7.2.2	Discussion . . . . .	121
7.3	Defect density at the a-Si:H/c-Si interface of passivated emitters . . . . .	122
7.3.1	Assumptions . . . . .	122
7.3.2	Results . . . . .	123
7.3.3	Discussion . . . . .	123
<b>8</b>	<b>Application to solar cells</b>	<b>127</b>
8.1	Rear-COSIMA solar cells . . . . .	127
8.1.1	Contact layout . . . . .	127
8.1.2	Processing sequence . . . . .	129
8.1.3	Current-voltage characteristics . . . . .	130
8.1.4	Internal quantum efficiency . . . . .	131
8.2	Symmetric-COSIMA solar cells . . . . .	135
8.2.1	Processing sequence . . . . .	135
8.2.2	Optimum thickness of the front a-Si:H film . . . . .	136
8.2.3	Front-textured symmetric-COSIMA solar cells . . . . .	141
8.3	Conclusion . . . . .	142
<b>9</b>	<b>Summary</b>	<b>143</b>
	<b>References</b>	<b>147</b>
	<b>Symbols and acronyms</b>	<b>159</b>
	<b>List of publications</b>	<b>163</b>



# 1 Introduction

The energy conversion efficiency of crystalline silicon (c-Si) solar cells is mainly controlled by the recombination probability of photogenerated carrier pairs, both in the bulk and at the surfaces. Since the thickness of silicon wafers as the starting material in solar cell production has been reduced over the last years to save silicon feedstock, the increased surface-to-volume ratio of solar cells demands for an improved electronic passivation of surface recombination centers.

Thermal oxidation is the state-of-the-art process for the passivation of surface defects in crystalline silicon, that is used both in microelectronics, and in the laboratory-scale fabrication of high-efficiency silicon solar cells. However, thermal oxidation requires high process temperatures around  $1000^{\circ}\text{C}$ , that result in a high energy consumption and a high risk of impurity diffusion into the c-Si bulk. It is therefore not suitable for the surface passivation of solar cells in industrial fabrication lines.

The deposition of hydrogenated, amorphous silicon nitride ( $\text{SiN}_x$ ) films by plasma enhanced chemical vapor deposition (PECVD) as a passivation layer, has the advantage of a lower process temperature  $T \approx 400^{\circ}\text{C}$ . Silicon nitride deposition is thus used as a standard process for both, passivation and anti reflective coating of the emitter surface in industrial solar cell production. However, a high density of fixed positive charges in the  $\text{SiN}_x$  film leads to the formation of an inversion layer at the surface of the lowly-doped  $p$ -type base of solar cells [1, 2]. Shunting of the inversion layer and the base contacts generates an additional recombination path at the rear surface. This effect reduces the maximum possible energy conversion efficiency of such cells when compared to cells with a thermally oxidized base surface.

Surface passivation of c-Si by intrinsic, hydrogenated amorphous silicon (a-Si:H) deposited by PECVD at  $T < 250^{\circ}\text{C}$ , combines the excellent passivation quality of thermally grown  $\text{SiO}_2$ , with an even lower process temperature than for  $\text{SiN}_x$  deposition. Furthermore, a-Si:H films deposited on c-Si exhibit no fixed charges, as  $\text{SiN}_x$  films would [3]. Therefore, shunting of a charge-induced floating junction with the base contacts, which is a significant loss mechanism in solar cells with a  $\text{SiN}_x$ -passivated base, does not occur in a-Si:H-passivated cells.

The excellent electronic passivation of lowly-doped crystalline silicon surfaces by a thin a-Si:H film is exploited in the industry for the fabrication of high-efficiency a-Si:H/c-Si *heterojunction* solar cells, like Sanyo's HIT<sup>TM</sup> cell [4, 5]. However,

no literature exists about the suitability of a-Si:H for the surface passivation of highly-doped silicon, such as emitters of *homojunction* c-Si solar cells.

This work focuses on the surface passivation of both, highly and lowly-doped crystalline silicon surfaces by amorphous silicon. In order to gain a deeper understanding of the physical nature of defect states at the a-Si:H/c-Si interface, a defect model is developed that allows for the determination of the defect density and carrier capture cross sections, by fitting measured injection-dependent surface recombination rates with the device simulation software AFORS-HET. The passivation and formation of recombination centers are studied quantitatively during illumination and thermal annealing processes by use of the model, in order to improve the microscopic understanding of the passivation mechanisms by a-Si:H, and to technologically improve the thermal stability of the surface passivation.

A technique for the formation of local contacts to a-Si:H-passivated solar cells is developed, together with an analytic model that allows for the optimization of local contact layouts for minimum surface recombination and series resistance of solar cells. The optical properties of thin a-Si:H films are studied with respect to their impact on the energy conversion efficiency of solar cells that feature an a-Si:H-passivated front side. Finally, the results of this work are applied to fabricate solar cells that feature a-Si:H-passivation of the emitter and base.

**Chapter 2** reviews the recombination paths for photogenerated carriers in silicon solar cells, the impact of carrier recombination in the bulk and at the surfaces on the current-voltage characteristics of solar cells, and the measurement techniques which are used in this work to obtain the effective surface recombination velocity as a measure for the quality of the surface passivation. An analytic model for the base saturation current of solar cells with passivated, locally contacted base is developed, that is suitable for optimizing the base contact layout for a maximum energy conversion efficiency.

**Chapter 3** presents the COSIMA technique, which is a two-step process comprising a-Si:H surface passivation, and the formation of local aluminum contacts through the amorphous silicon passivation layer. The basic mechanism as well as the technologically relevant contact resistances to base and emitter, are determined.

**Chapter 4** deals with the quality of the amorphous silicon passivation on crystalline silicon surfaces. Besides the passivation by a-Si:H single layers, an a-Si:H/SiN<sub>x</sub> double layer passivation scheme is developed. The successful passivation of diffused emitters, and of textured surfaces by a-Si:H is shown. The stability of the passivation under UV irradiation is determined.

**Chapter 5** shows the electronic properties of the a-Si:H/c-Si interface, and of



---

the a-Si:H bulk material. A model for the recombination centers in the a-Si:H bulk and at the a-Si:H/c-Si interface is developed, which is based on measurements of the distribution function of the density of states.

**Chapter 6** examines the stability of the a-Si:H surface passivation during illumination, in order to investigate the long-term stability of a-Si:H passivated solar cells. The model which is derived in Chapter 5 is fitted to the experimental data in order to further characterize the interface defect states in terms of their capture cross sections for electrons and holes, and to separate the contribution of the recombination through the interface defects from the recombination through the a-Si:H bulk defects.

**Chapter 7** discusses the stability of the a-Si:H surface passivation during annealing, as it occurs in solar cell fabrication processes during the firing of metal contacts, and during soldering and lamination of cells in a module. The formation of defect states during the annealing is investigated by fitting the defect model to the experimental data.

**Chapter 8** describes the successful application of a-Si:H passivation and of the COSIMA contacting scheme to solar cells. Starting from symmetrically silicon nitride-passivated cell developed at ISFH [6], the benefit of the introduction of a-Si:H for the base passivation is shown. The thickness of the a-Si:H passivation layer is further optimized to provide an optimum of both, surface passivation and transparency when applied to the front side of the solar cell. Finally, a solar cell that features a-Si:H passivation on both sides is developed.



## 2 Carrier recombination in silicon solar cells

This chapter reviews the recombination paths for photogenerated carriers in silicon solar cells, the impact of the bulk and surface recombination on the current-voltage characteristics of the solar cell, and the measurement techniques which are used in this work to obtain the effective surface recombination velocity as a measure for the quality of the surface passivation.

Section 2.2 discusses the intrinsic and defect-related contributions to the carrier recombination in the crystalline silicon bulk material. In Section 2.3, the recombination through surface states is described by the extended Shockley-Read-Hall formalism. Section 2.4 reviews the methods for measuring the effective carrier lifetime which are used in this work. The separation of the contributions of bulk- and surface recombination to the measured recombination rate is described. The impact of carrier recombination in the base and in the emitter on the current-voltage characteristics of solar cells is discussed in Section 2.5. The contributions of bulk and surface recombination to the emitter saturation current are shown. High-efficiency solar cells feature a passivated rear surface with local contacts, and thus exhibit a spatially inhomogeneous rear surface recombination rate. Section 2.6 shows a model for the calculation of the base saturation current of such devices, which was developed in this work.

### 2.1 Definitions

Carrier recombination in a semiconductor is the transition of an electron from the conduction band to the valence band, which can also be described as the annihilation of an electron-hole pair. In a non-illuminated semiconductor in thermal equilibrium, the concentrations of free carriers are constant,  $n = n_0$  for electrons in the conduction band and  $p = p_0$  for holes in the valence band. The balance between thermal generation and recombination is expressed by the law of mass action,  $n_0 p_0 = n_{i,\text{eff}}^2$ , where  $n_{i,\text{eff}} = 9.65 \times 10^9 \text{ cm}^{-3} \times \exp(\Delta E_{\text{gap}}/kT)$  is the effective intrinsic carrier concentration in silicon,  $\Delta E_{\text{gap}}$  is the doping-dependent band-gap narrowing, and  $kT$  is the thermal energy [7]. For  $p$ -type silicon with a dopant concentration of  $N_A = 1 \times 10^{16} \text{ cm}^{-3}$  as it is used in the carrier lifetime analysis shown in this work, the effective intrinsic carrier concentration is  $n_{i,\text{eff}} = 1.05 \times 10^{10} \text{ cm}^{-3}$

[7]. Assuming complete ionization of the doping atoms, which is a good approximation for silicon at room temperature,

$$\begin{aligned} n_0 &= N_D, & p_0 &= \frac{n_i^{\text{eff}}}{N_D} & \text{for n-type semiconductors} \\ p_0 &= N_A, & n_0 &= \frac{n_i^{\text{eff}}}{N_A} & \text{for p-type semiconductors.} \end{aligned} \quad (2.1)$$

Under illumination, an excess concentration  $\Delta n$  of electron-hole pairs are generated by absorption of incident photons. Therefore,  $n = n_0 + \Delta n$  and  $p = p_0 + \Delta n$ . After turning off the illumination, the excess carrier concentration decays with the net recombination rate

$$U(\Delta n(t), n_0, p_0) = -\frac{\partial \Delta n(t)}{\partial t}. \quad (2.2)$$

Different mechanisms contribute to the carrier recombination. Assigning an individual recombination rate to each independent recombination path, the net recombination rate can be rewritten as the sum of all individual recombination rates

$$U(\Delta n(t), n_0, p_0) = \sum_i U_i(\Delta n(t), n_0, p_0). \quad (2.3)$$

If the recombination probability of a single carrier is independent of the excess carrier concentration,  $U \propto \Delta n$ . Equation 2.2 then describes a mono-exponential decay of  $\Delta n(t) = \Delta n(0) \exp(-\frac{t}{\tau})$ . The time constant  $\tau$  is the *carrier lifetime*

$$\tau = \frac{\Delta n(t)}{U(\Delta n(t), n_0, p_0)} = \left( \sum_i \frac{1}{\tau_i} \right)^{-1}. \quad (2.4)$$

The mean distance a charge carrier travels within the lifetime  $\tau$  is the *diffusion length*

$$L = \sqrt{D\tau}, \quad (2.5)$$

with  $D$  being the diffusion constant which depends on the doping concentration [8]. The Equations 2.4 and 2.5 are also used in the case of  $U$  being a non-linear function in  $\Delta n$ . Both,  $\tau$  and  $L$  are then functions of  $\Delta n$ .

## 2.2 Bulk recombination

In solar cells, the term *bulk* is applied to the region of the base where the gradient of the electrostatic potential vanishes,  $\nabla\Psi = 0$ , which means that the valence and conduction band edges are flat, and charge neutrality prevails. Recombination

in the emitter is treated as surface recombination, as described in Section 2.5.1. Carrier recombination in the crystalline silicon bulk occurs via two intrinsic, and one extrinsic recombination paths. Intrinsic recombination paths are the radiative band-to-band recombination, and the non-radiative band-to-band Auger recombination, which is a three-particle process including an electron or hole to carry off the momentum and energy of the recombining carrier pair.

Impurity atoms or defects in the crystal lattice can form energy levels within the bandgap of the semiconductor. The carrier recombination through such extrinsic energy levels is described by the Shockley-Read-Hall (SRH) formalism.

The effective bulk carrier lifetime is calculated from the radiative recombination lifetime  $\tau_{\text{rad}}$ , the Auger lifetime  $\tau_{\text{Auger}}$ , and the SRH lifetime  $\tau_{\text{SRH}}$  according to Equation 2.4:

$$\frac{1}{\tau_b} = \frac{1}{\tau_{\text{rad}}} + \frac{1}{\tau_{\text{Auger}}} + \frac{1}{\tau_{\text{SRH}}}. \quad (2.6)$$

### 2.2.1 Radiative band-to-band recombination

Radiative recombination is the reverse process of photo-induced carrier generation. An electron-hole pair annihilates, emitting a photon that carries the excess energy. However, in an indirect semiconductor like silicon, an additional phonon is needed for momentum conservation. Therefore the probability of radiative recombination is much lower than in direct semiconductors. As one electron and one hole participate in the recombination process, the total recombination rate is proportional to the product of their densities. To calculate the net recombination rate of photo-generated excess carriers, the recombination rate of the non-illuminated case has to be subtracted:

$$U_{\text{rad}} = B (np - n_i^2). \quad (2.7)$$

The temperature dependent coefficient  $B$  has been determined by Schlagenotto [9]. For silicon at room temperature,  $B = 9.5 \times 10^{-15} \text{ cm}^3 \text{ s}^{-1}$  has been found.

The effective lifetime  $\tau_{\text{rad}}$  associated with the radiative recombination process is calculated from the Equations 2.4 and 2.7:

$$\tau_{\text{rad}} = \frac{1}{B (n_0 + p_0 + \Delta n)}. \quad (2.8)$$

### 2.2.2 Auger recombination

Auger recombination is the second intrinsic recombination mechanism in the bulk of semiconductors. The excess energy is not emitted as a photon but is transferred to a third carrier, which is either an electron in the conduction band (eeh-process), or a hole in the valence band (ehh-process). The recombination rates are proportional

to the product of the densities of the involved carriers,  $n$  and  $p$ , respectively. In the idealized case of the involved carriers being non-interacting free particles

$$U_{\text{Auger,ideal}} = C_n (n^2 p - n_i^2 n_0) + C_p (np^2 - n_i^2 p_0), \quad (2.9)$$

with  $C_n$  and  $C_p$  being the Auger coefficients for the eeh- and the ehh-process, respectively. Dziewior and Schmid determined the Auger coefficients  $C_n = 2.8 \times 10^{-31} \text{ cm}^6 \text{ s}^{-1}$ , and  $C_p = 9.9 \times 10^{-32} \text{ cm}^6 \text{ s}^{-1}$  by fitting experimental lifetime data for silicon with a doping concentration  $N_{\text{dop}} > 5 \times 10^{18} \text{ cm}^{-3}$  [10].

While the idealized case of Equation 2.9 fits quite well with measured recombination rates in highly doped silicon, the recombination rate in material with lower doping densities is found to be considerably higher, as the recombination is enhanced by Coulomb-attraction between the recombining electrons and holes. For high doping concentrations, this effect is negligible due to screening of the minority carriers. Furthermore, additional effects like phonon-assisted Auger recombination add to the total Auger recombination rate. Due to the variety of the involved processes, a complete theoretical approach to describe Auger recombination is difficult. Kerr and Cuevas have deduced a parameterization for the Auger recombination rate in  $n$ - and  $p$ -type silicon based on measurements of the bulk lifetime for doping concentrations between  $10^{13} \text{ cm}^{-3}$  and  $10^{20} \text{ cm}^{-3}$  [11]:

$$U_{\text{Auger}} = np (1.8 \times 10^{-24} n_0^{0.65} + 6.0 \times 10^{-25} p_0^{0.65} + 3.0 \times 10^{-27} \Delta n^{0.8}). \quad (2.10)$$

With the radiative recombination rate from Equation 2.7, the parameterization of the intrinsic carrier lifetime in silicon is

$$\tau_{\text{intr}} = \frac{\Delta n}{np (1.8 \times 10^{-24} n_0^{0.65} + 6.0 \times 10^{-25} p_0^{0.65} + 3.0 \times 10^{-27} \Delta n^{0.8} + 9.5 \times 10^{-15})}, \quad (2.11)$$

which is the upper limit for the carrier lifetime in monocrystalline silicon. Equation 2.11 is used for the calculation of the intrinsic bulk lifetime of crystalline silicon throughout this work.

Figure 2.1 shows  $\tau_{\text{intr}}$  as a function of the excess carrier density  $\Delta n$  of  $p$ -type silicon with the acceptor concentration  $N_A = 1.0 \times 10^{16} \text{ cm}^{-3}$  and  $N_A = 6.5 \times 10^{13} \text{ cm}^{-3}$  (specific resistance  $\rho = 1.5 \text{ } \Omega\text{cm}$  and  $\rho = 200 \text{ } \Omega\text{cm}$ ). In low-level injection (*lli*),  $\Delta n \ll N_A$  and therefore  $pn \approx N_A \Delta n$ , the intrinsic carrier lifetime is independent of the excess carrier density:  $\tau_{\text{intr,lli}}^{-1} \approx (1.8 \times 10^{-25} N_A^{0.65} + 9.5 \times 10^{-15}) N_A$ .

### 2.2.3 Recombination through defects

Defects in the silicon crystal lattice, like dislocations or impurity atoms can induce energy levels within the silicon bandgap. These additional energy levels may

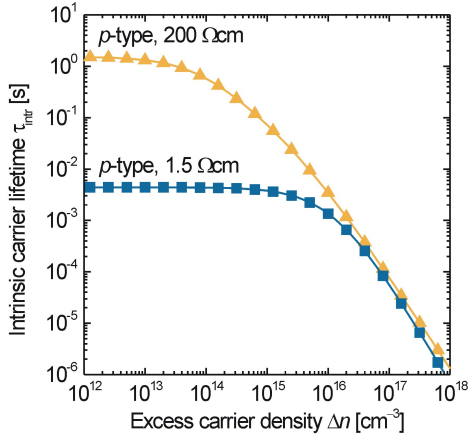


Figure 2.1: *Intrinsic carrier lifetime  $\tau_{\text{intr}}$  of p-type silicon with  $N_{\text{A}} = 1.0 \times 10^{16} \text{ cm}^{-3}$  (1.5  $\Omega\text{cm}$ ) and  $N_{\text{A}} = 6.5 \times 10^{13} \text{ cm}^{-3}$  (200  $\Omega\text{cm}$ ). In lli, the intrinsic lifetime is independent of  $\Delta n$ .*

enhance carrier recombination, depending on their capture cross sections  $\sigma_{\text{n}}$  for electrons, and  $\sigma_{\text{p}}$  for holes. The statistical model for the recombination rate was developed by Shockley and Read [12], and Hall [13] for defects with a fixed energy level  $E_{\text{t}}$ , and density  $N_{\text{t}}$ . The net Shockley-Read-Hall (SRH) recombination rate

$$U_{\text{SRH}} = \frac{(np - n_{\text{i}}^2)}{\tau_{\text{n0}}(p + p_1) + \tau_{\text{p0}}(n + n_1)}, \quad (2.12)$$

with the capture time constants

$$\begin{aligned} \tau_{\text{n0}} &= \frac{1}{N_{\text{t}}\sigma_{\text{n}}v_{\text{th,n}}} \quad \text{for electrons, and} \\ \tau_{\text{p0}} &= \frac{1}{N_{\text{t}}\sigma_{\text{p}}v_{\text{th,p}}} \quad \text{for holes,} \end{aligned} \quad (2.13)$$

and the densities of occupied states

$$\begin{aligned} n_1 &= n_{\text{i}} \exp\left(\frac{E_{\text{t}} - E_{\text{i}}}{kT}\right) \quad \text{for electrons, and} \\ p_1 &= n_{\text{i}} \exp\left(\frac{E_{\text{i}} - E_{\text{t}}}{kT}\right) \quad \text{for holes,} \end{aligned} \quad (2.14)$$

where  $E_{\text{i}}$  is the intrinsic Fermi level. The mean thermal carrier velocity is  $v_{\text{th}} = \sqrt{8kT/\pi m_{\text{th}}^*}$ , where  $m_{\text{th}}^*$  is the thermal velocity effective mass. At 300 K,  $m_{\text{th,n}}^* =$

$0.28m_0$ , and  $m_{\text{th},p}^* = 0.41m_0$  with  $m_0$  being the electron rest mass [14]. Hence  $v_{\text{th},n}^* = 2.0 \times 10^7$  cm/s and  $v_{\text{th},p}^* = 1.7 \times 10^7$  cm/s. The SRH carrier lifetime is then

$$\tau_{\text{SRH}} = \frac{\tau_{p0} (n_0 + n_1 + \Delta n) + \tau_{n0} (p_0 + p_1 + \Delta n)}{p_0 + n_0 + \Delta n}. \quad (2.15)$$

## 2.3 Surface recombination

For simplicity, the term *surface* is applied to both, the non-passivated and the passivated crystalline silicon surface in this section, although the term *interface* might be more appropriate in the latter case. Besides the recombination through actual surface states, also enhanced bulk recombination due to surface band bending and recombination within the amorphous silicon passivation layers will be summarized by the term *effective surface recombination*.

### 2.3.1 Recombination through surface states

The surface terminates the periodicity of the crystal lattice that is the basis of the formation of bonding and antibonding energy bands from the electronic orbitals of silicon atoms. Therefore, localized electronic states exist at the surface, which form recombination-active energy levels within the bandgap. From the chemical point of view, these energy levels can be identified with non-bonded orbitals called *dangling bonds* of surface atoms that can capture or release electrons. Due to fluctuations in the bonding angle and in the distance to neighboring atoms, the energy levels of these dangling bonds are distributed continuously over the energy bandgap [15, 16, 17]. The net recombination rate through non-interacting surface states is obtained by extending the SRH formalism shown in Section 2.2.3 by integrating over all energy levels within the bandgap:

$$U_{\text{it}} = (n_{\text{s}}p_{\text{s}} - n_{\text{i}}^2) \int_{E_{\text{V}}}^{E_{\text{C}}} \frac{v_{\text{th}} D_{\text{it}}(E) dE}{\sigma_{\text{p}}^{-1}(E) (n_{\text{s}} + n_1(E)) + \sigma_{\text{n}}^{-1}(E) (p_{\text{s}} + p_1(E))} \quad (2.16)$$

where  $n_{\text{s}}$  and  $p_{\text{s}}$  are the concentrations of electrons and holes at the surface, respectively. The density of states per energy interval,  $D_{\text{it}}(E)$  is the distribution function of the surface states (or interface states, if the surface is passivated).

It is obvious from Equation 2.16 that there are two possible ways of surface passivation:



- **Reduction of  $D_{it}$**

by chemically saturating the dangling bonds with hydrogen or oxygen atoms. This effect is exploited when passivating the surface with dielectric layers like  $\text{SiO}_2$  and hydrogenated  $\text{SiN}$ , or with hydrogenated amorphous silicon.

- **Reduction of  $n_s$  or  $p_s$**

by inducing an electric field, which can be caused by fixed charges in the  $\text{SiO}_2$  or  $\text{SiN}$  film (*field effect passivation*), or by the introduction of a highly doped surface layer (*back surface field BSF*, or *floating junction / emitter*).

Equations 2.12–2.14 show that the actual distribution of the dangling bond levels  $D_{it}(E)$  has a significant influence on  $U_{it}$ , since states near midgap (deep states) contribute more to the recombination rate than states near the band edges (shallow states). Therefore, an effective surface passivation method has to eliminate mainly the deep surface energy levels.

### 2.3.2 Effective surface recombination velocity

The formation of a space charge region at the crystalline silicon surface is usually observed due to charges that are captured in the surface states, or due to fixed charges in dielectric passivation layers. The electric field of a a-Si:H/c-Si heterojunction, or a BSF layer also leads to the formation of a surface space charge region. As charge neutrality does not prevail within this sub-surface region, the recombination of charge carriers there cannot be described with the expressions derived in Section 2.2. For convenience, an *effective surface* is defined at the edge of the surface space charge region. All recombination that is due to surface effects is then lumped into the effective surface recombination rate  $U_{s,\text{eff}}$ , which is the sum of three contributions:

- recombination through the surface states,  $U_{it}$ ,
- recombination in the space charge region,  $U_{\text{scr}}$ , and
- recombination in the surface layer,  $U_{\text{sl}}$ .

As  $U_{s,\text{eff}}$  is a recombination rate per unit area, the definition of a surface lifetime along the lines of Equation 2.4 is not possible. Instead, an *effective surface recombination velocity* (SRV) is defined by

$$S = \frac{U_{s,\text{eff}}}{\Delta n_s} = \frac{U_{it} + U_{\text{scr}} + U_{\text{sl}}}{\Delta n_s}, \quad (2.17)$$

with  $\Delta n_s$  being the excess carrier density at the edge of the surface space charge region. Obviously, this concept also applies to the emitter of a solar cell, if the effective surface is defined at the edge of the pn-junction within the base.

In low-level injection (*lli*) conditions,  $\Delta n \ll n_0$  (*n*-type silicon), or  $\Delta n \ll p_0$  (*p*-type silicon), a simple relation can be given for the recombination velocity through interface states with energy-independent capture cross sections  $\sigma_{n/p}$ , and energy-independent density of states  $D_{it}$ , by integrating Equation 2.16:

$$\begin{aligned} S_{it,lli,n} &= v_{th} D_{it} \sigma_p && \text{for } n\text{-type semiconductors, and} \\ S_{it,lli,p} &= v_{th} D_{it} \sigma_n && \text{for } p\text{-type semiconductors.} \end{aligned} \quad (2.18)$$

This means that under *lli* conditions, the surface recombination rate is determined by the capture of the minority carriers.

Girisch et al. developed an extended SRH formalism to numerically calculate  $U_{it}$  in the presence of surface charges [18]. Dauwe has also found an analytic expression for  $U_{scr}$ , by integrating the SRH-recombination rate described by Equation 2.12 in the space charge region of SiN-passivated crystalline silicon [19]. In this work, a model is developed for the distribution functions and the carrier capture cross sections of defects at the a-Si:H/c-Si and in the a-Si; bulk material. The defect densities at the a-Si:H/c-Si interface, and in the a-Si:H surface layer of a-Si:H passivated crystalline silicon are determined by fitting the model to measurements of the injection-dependent lifetime with the finite-element simulation tool AFORS-HET [20].

## 2.4 Measurement of the effective carrier lifetime

The effective carrier lifetime in crystalline silicon is determined by both, recombination in the bulk and at the surfaces. In this work, silicon wafers with a high bulk lifetime are used to investigate the surface passivation properties of amorphous silicon layers. Measurement techniques to determine  $\tau_{eff}$  are based on the time- or injection-dependent detection of the photogenerated excess carrier concentration, by interaction of the free carriers with electromagnetic fields, e.g. inductive coupling, microwave reflection, or absorption of infrared light. Therefore, only the *average* excess carrier density  $\Delta n_{av}$  over the sample thickness can be determined. For an excitation light pulse of arbitrary duration, the effective carrier lifetime

$$\tau_{eff} = \frac{\Delta n_{av}(t)}{U(t)} = \frac{\Delta n_{av}(t)}{G_{av}(t) - \frac{\partial \Delta n_{av}}{\partial t}}, \quad (2.19)$$

where  $G_{av}$  is the carrier photogeneration rate, and  $U$  is the total recombination rate [21]. In steady state conditions, the recombination rate equals the generation rate,  $U = G_{av}$ . The term  $\partial \Delta n_{av} / \partial t$  describes the transient decay of  $\Delta n_{av}$  if the

generation changes too fast for the test structure to remain in thermal equilibrium. Two measurement techniques are used in this work:

- **Quasi-steady state photoconductance (QSSPC):**

Charge carriers are excited by a photo flash lamp whose decay time is larger than the carrier lifetime, so that the recombination rate  $U \approx G_{\text{av}}$ , and  $\partial \Delta n_{\text{av}} / \partial t$  is a small correction. The excess carrier density is determined from the inductively measured photoconductance [22]. This is a large-signal technique, which means that the injection level  $\Delta n_{\text{av}}$  is set by the light intensity of the decaying flash. The measured lifetime values are absolute ones, because the sample is (quasi) in thermal equilibrium. The determined lifetimes are therefore representative for illuminated solar cells [23, 24]. A wide injection range can be covered with a single measurement.

- **Transient microwave-detected photoconductance decay (MWPCD):**

Carriers are excited by a short laser pulse. During the measurement,  $G_{\text{av}} = 0$ . The free carriers change the microwave reflectivity of the sample, and the transient decay of  $\Delta n_{\text{av}}$  is determined from the decay of the microwave reflectivity. This is a small-signal technique, which means that the injection level of  $\Delta n_{\text{av}}$  has to be set by shining bias light onto the sample, while the pulse-shaped photoexcitation has to be a small perturbation. The measured lifetimes are therefore differential values which are not necessarily the same as in a solar cell in thermal equilibrium [23, 24]. However, spatially resolved measurements of  $\tau_{\text{eff}}$  are possible. Therefore, MWPCD is a helpful characterization tool mainly for multicrystalline silicon wafers.

The general expression for the effective carrier lifetime

$$\frac{1}{\tau_{\text{eff}}} = \frac{1}{\tau_{\text{b}}} + \frac{1}{\tau_{\text{s}}} \quad \text{with} \quad \frac{1}{\tau_{\text{s}}} = \frac{\Delta n_{\text{f}}}{\Delta n_{\text{av}}} \times \frac{S_{\text{f}}}{W} + \frac{\Delta n_{\text{r}}}{\Delta n_{\text{av}}} \times \frac{S_{\text{r}}}{W}, \quad (2.20)$$

is obtained by solving the semiconductor transport Equations [25].  $\tau_{\text{s}}$  is the surface lifetime,  $W$  is the width of the wafer,  $\Delta n_{\text{f}}$  and  $\Delta n_{\text{r}}$  are the excess carrier densities at the front and rear (effective) surface, and  $S_{\text{f}}$  and  $S_{\text{r}}$  are the front and rear effective surface recombination velocities, respectively. For a silicon wafer with identically passivated front and rear side as it is used in this work,  $S = S_{\text{f}} = S_{\text{r}}$ , and

$$\frac{1}{\tau_{\text{s}}} = \frac{\Delta n_{\text{f}} + \Delta n_{\text{r}}}{2 \Delta n_{\text{av}}} \times \frac{2S}{W} \equiv \chi \times \frac{2S}{W}, \quad (2.21)$$

with  $0 \leq \chi \leq 1$ . Therefore, the commonly used estimate

$$S \approx \frac{W}{2\tau_{\text{s}}} \quad (2.22)$$

is the lower limit of the actual SRV. Obviously, it is the exact solution of Equation 2.21 when  $\chi = 1$ , i.e. when the excess carrier profile is uniform over the whole width of the wafer. Fischer has shown that this is the case for transient and QSSPC measurements regardless of the generation profile, as long as the SRV is small and the bulk lifetime is large. Quantitatively, Equation 2.22 is accurate to  $\Delta S/S < 0.1$  as long as  $S < W/D_a$  and  $\tau_b > W^2/D_a$ , with  $D_a$  being the ambipolar diffusion constant [25].<sup>1</sup>

In order to extract SRVs larger than  $S = W/D_a$  correctly from lifetime measurements, care must be taken as to how the measurement is set up. For *QSSPC*,  $\Delta n_f$  and  $\Delta n_r$  have to be determined by solving the diffusion equation for the generation profile that corresponds to the wavelength spectrum of the illuminating flash lamp. Then, Equations 2.21 and 2.20 can be used to determine the SRV. Small bulk lifetimes also have an impact on the parameter  $\chi$ , because the carrier profile will assume the shape of the generation profile, if  $\tau_b \ll W^2/D_a$  [25]. Therefore, infrared light with  $\lambda > 800$  nm is mostly used in order to obtain a uniform generation profile also in lifetime samples with a low bulk lifetime.

The best accuracy of Equation 2.22 for large surface recombination velocities,  $S > W/D_a$ , is achieved in QSSPC measurements of samples with a large bulk lifetime, and photogeneration only at the front surface of the wafer, as can be achieved by illumination with blue light. The reason for this effect is that a skew-symmetric excess carrier profile develops, and therefore  $\chi = 1$  regardless of the surface recombination velocity [25, 26].

In this work, an infrared filter transmitting only wavelengths  $\lambda > 700$  nm is used for the QSSPC measurements, in order to prevent the generation of carriers within the a-Si:H passivation layer. Amorphous silicon is mostly transparent for wavelengths that correspond to photon energies that are smaller than the optical bandgap, which is around  $E_{g,a-Si:H} \approx 1.76$  eV ( $\lambda_{g,a-Si:H} \approx 730$  nm) for PECVD-deposited a-Si:H [27, 28, 29]. Therefore, excess carriers are mostly generated in the c-Si bulk. Recombination in the amorphous silicon layer is then restricted to carriers that tunnel or diffuse from the c-Si bulk into the a-Si:H bulk.

The exact, yet transcendent equation for the *transient surface lifetime* is found by solving the transport Equations in Fourier space [30, 31, 32]:

$$\tau_{s,\text{trans}} = \frac{1}{\beta_0^2 D_a} \quad \text{with} \quad \tan(\beta_0 W) = \frac{2SD_a\beta_0}{D_a^2\beta_0^2 - S^2}. \quad (2.23)$$

The measured value of  $\tau_{s,\text{trans}}$  has to be extracted from Equation 2.20. Then Equation 2.23 can be used to analytically determine the effective surface recombination

<sup>1</sup>For the lifetime samples used in this work,  $W = 300 \mu\text{m}$ ,  $D = 30 \text{ cm}^2/\text{s}$  in low-injection, and  $\tau_b \approx \tau_{\text{Auger}} = 3$  ms. Equation 2.22 is therefore valid as long as  $S < 1000 \text{ cm/s}$ .

velocity  $S$ . Alternatively, Equation 2.23 can be approximated by

$$\tau_{s,\text{trans}} \approx \frac{W}{2S} + \frac{W^2}{\pi^2 D_a}, \quad (2.24)$$

with an error of less than 5% for all values of  $S$  [33].

## 2.5 Diode saturation current

The diode saturation current density as a measure for the impact of carrier recombination on the efficiency of a solar cell is discussed in the one-dimensional diode model. Section 2.5.1 reviews the determination of the base- and the emitter-saturation current densities from lifetime measurements. The contribution of intrinsic bulk recombination to the emitter saturation current density is shown in Section 2.5.2.

In case of negligible series- and shunt-resistances, the current-voltage characteristics of a solar cell in the multi-diode model is [34, 35]:

$$J(V) = \sum_i J_{0,i} \left[ \exp\left(\frac{qV}{m_i kT}\right) - 1 \right] - J_L = J_{\text{rec}} - J_L, \quad (2.25)$$

where  $J$  is the current density,  $V$  is the terminal voltage,  $kT/q$  is the thermal voltage.  $J_{\text{rec}}$  is the recombination current density, and  $J_L$  is the photogenerated current density. Each recombination path  $i$  is characterized by its saturation current  $J_{0,i}$ , and its ideality factor  $m_i$ . *Ideal* recombination processes with  $U \propto \Delta n^2$  result in the ideality factor  $m = 1$ , which is approximately true for surface and bulk recombination. Recombination in the space charge region shows a voltage dependence with  $m \leq 2$ , but is negligible for most high-efficiency solar cells. Therefore, the one-diode model can be applied with  $m \equiv 1$ , i. e. the summation in Equation 2.25 becomes obsolete and the recombination current density is rewritten as

$$J_{\text{rec}}(V) = J_0 \left[ \exp\left(\frac{qV}{kT}\right) - 1 \right] = J_0 \frac{pn - n_i^2}{n_i^2}. \quad (2.26)$$

No external current flows in open circuit conditions, therefore  $J_{\text{rec}} = J_L$ . The open-circuit voltage is then

$$V_{\text{oc}} = \frac{kT}{q} \ln\left(\frac{J_L}{J_0} + 1\right), \quad (2.27)$$

where the photogenerated current density is usually approximated by the short-circuit current,  $J_L \approx J_{\text{sc}}$  [35].

### 2.5.1 Determination of base and emitter saturation current

The diode saturation current density  $J_0$  is the sum of the emitter saturation current density and the base saturation current density,  $J_0 = J_{0e} + J_{0b}$ . Recombinative losses due to bulk recombination and recombination at the surface of the base are lumped in the **base saturation current density**  $J_{0b}$ , which can be calculated analytically [36]. If the base is in low-injection conditions  $\Delta n \ll N_{\text{dop}}$ ,

$$J_{0b} = \frac{qDn_i^2}{L_{\text{eff}}N_{\text{dop}}} \quad \text{with} \quad L_{\text{eff}} = L_b \frac{1 + SL_b/D \tanh(W/L_b)}{SL_b/D + \tanh(W/L_b)}, \quad (2.28)$$

where  $L_{\text{eff}}$  is the effective carrier diffusion length in the base, and  $L_b = \sqrt{D\tau_b}$  is the bulk diffusion length. The surface recombination velocity  $S$  can be determined from lifetime measurements, as has been shown in Section 2.4.

The **emitter saturation current density**  $J_{0e}$  cannot be calculated analytically due to the non-uniform diffusion profile. It has to be calculated numerically, or determined from lifetime measurements of suitable test structures. In lifetime measurements of samples with a diffused emitter, photoconductance within the emitter is negligible because the emitter is thin compared to the substrate, and because the emitter is always in low-injection conditions due to its high doping level. Therefore, the emitter is to be treated as a surface layer that is characterized by an effective SRV,  $S_e$ , which corresponds to the emitter recombination current density:  $J_{\text{rec,e}} = q\Delta n_s S_e$ . For a  $p$ -type base ( $p_0 \approx N_A \ll n_0$ ), Equation 2.26 then becomes

$$S_e = \frac{J_{0e}}{qn_i^2} (N_A + \Delta n_s), \quad (2.29)$$

and  $J_{0e}$  can be determined from the effective lifetime of a sample that features an emitter on both surfaces, by using the Equations 2.20 and 2.21. When assuming  $\Delta n_s = \Delta n_{\text{av}}$  and  $\chi = 1$ ,

$$\frac{1}{\tau_{\text{eff}}} - \frac{1}{\tau_{\text{Auger}}} = \frac{1}{\tau_{\text{SRH}}} + \frac{2J_{0e}}{qn_i^2 W} (N_A + \Delta n_{\text{av}}). \quad (2.30)$$

In this work, the high-injection measurement of  $J_{0e}$  has been performed, as proposed by Kane and Swanson [37], and Cuevas [38]: A lowly doped high-lifetime silicon wafer is used as substrate, which ensures that the injection level in QSSPC measurements can be set such that the substrate is in high injection conditions  $\Delta n \gg N_{\text{dop}}$ , while the emitter is in low injection. The high-injection SRH lifetime is independent of the injection level. The emitter saturation current  $J_{0e}$  can be therefore determined by Equation 2.30 from the slope of a plot of  $(\tau_{\text{eff}}^{-1} - \tau_{\text{Auger}}^{-1})$  versus  $\Delta n_{\text{av}}$ , as shown in Figure 2.2.

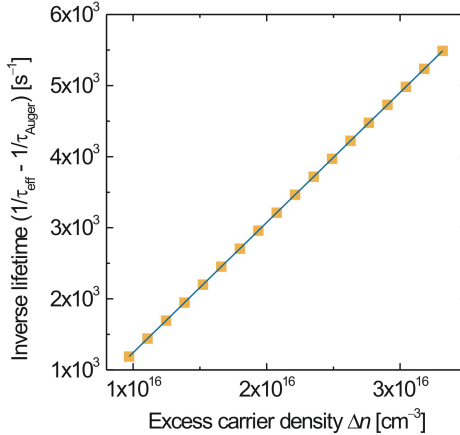


Figure 2.2: Illustration of the Kane-Swanson method for the determination of the emitter saturation current. The inverse lifetime  $\tau_{\text{eff}}^{-1} - \tau_{\text{Auger}}^{-1}$  of a c-Si wafer that features an emitter on both sides, is plotted against  $\Delta n_{\text{av}}$ . The emitter saturation current is extracted from the slope of a linear fit to the measured data, by Equation 2.30. In this example,  $W = 300 \mu\text{m}$  and  $J_{0e} = 40 \text{ fA/cm}^2$ .

## 2.5.2 Contributions to the emitter saturation current

All carrier recombination that occurs on the emitter side of the  $pn$ -junction is lumped in the emitter saturation current density  $J_{0e}$  which therefore depends on both, the emitter surface recombination velocity that is subject to the emitter surface passivation, and on the emitter bulk recombination.

In order to separate the carrier recombination rate in the bulk of the emitter from that at the surface, the transport and recombination processes have to be analyzed, accounting for the doping-dependence of the bulk carrier lifetime, the carrier mobility and the bandgap narrowing in highly doped silicon [7, 39, 40]. This has to be done numerically because the non-uniform emitter diffusion profile prohibits an analytical description. Finite-element simulation tools like SENTAURUS (formerly named DESSIS) are mostly employed, which is also used in the microelectronics industry [39, 41]. However, such analysis would exceed the scope of this work, which therefore concentrates on the emitter saturation current as a combined measure

of both, the quality of the emitter surface passivation and the suitability of the diffusion process for manufacturing high-efficiency solar cells.

Depending on the carrier diffusion length  $L_{\text{emitter}}$  in the emitter bulk, three different regimes are distinguished [42]:

- **Opaque emitter:** The bulk diffusion length in the emitter is much smaller than the junction depth,  $L_{\text{emitter}} \ll z_{\text{jct}}$ , hence electron-hole pairs that are photogenerated in the emitter will recombine before they reach the  $pn$ -junction. The emitter saturation current is then determined by the bulk recombination rate, and the passivation of the emitter surface has no effect.
- **Semi-transparent emitter:**  $L_{\text{emitter}} \approx z_{\text{jct}}$ . This is the case in most industrial solar cells. Both, surface and bulk recombination contribute to  $J_{0e}$ .
- **Transparent emitter:**  $L_{\text{emitter}} \gg z_{\text{jct}}$ . Bulk recombination can be neglected, so photogenerated electron-hole pairs only recombine at the surface. The emitter saturation current is therefore determined by the surface recombination rate, which also means that the efficiency of the surface passivation is highest with a transparent emitter. A well-passivated transparent emitter allows for the highest short-circuit current of the solar cell.

The dopant concentration within the emitter region is not uniform but decreases from the surface towards the  $pn$ -junction. Depending on the diffusion process, the near-surface region of the emitter can have dopant concentrations near the solubility limit, which accounts for an intrinsic carrier recombination rate that makes this region opaque. This is called a *dead layer*, because carrier pairs that are photogenerated there will recombine and hence do not contribute to the cell current. Therefore, an emitter diffusion process that is suitable for the production of high-efficiency solar cells has to be designed such that the formation of a dead layer is prohibited.

Equation 2.11 shows that the Auger recombination rate in low-level injection,  $\Delta n \ll N_{\text{dop}}$ , is proportional to the dopant concentration  $N_{\text{dop}}^{1.65}$ . The intrinsic carrier lifetime corresponding to the solubility limits ( $1.0 \times 10^{21} \text{ cm}^{-3}$  for boron and  $1.3 \times 10^{21} \text{ cm}^{-3}$  for phosphorus [43]) is in the  $10^{-2}$  ns range for both  $n^+$ - and  $p^+$ -Si, leading to bulk diffusion lengths in the  $10^{-2} \mu\text{m}$  range. Such a highly-doped emitter surface region is therefore detrimental for the performance of a solar cell, even if its thickness is only in the order of 1% of the emitter depth (which is usually in the order of  $1 \mu\text{m}$ ).



## 2.6 Analytic model for the base saturation current of locally contacted cells

Highly efficient silicon solar cells with a front  $pn$ -junction feature a passivated rear surface with locally defined, dot- or stripe-shaped contacts [44]. The passivated surface area shows a low recombination velocity, while the area below the metal contacts, which is usually a few percent of the total cell area, exhibits a higher SRV. This rear side structure is usually combined with a passivated emitter, and called passivated emitter and rear cell (PERC) [45]. The spatially inhomogeneous SRV leads to a spatially inhomogeneous carrier concentration at the surface of the base, and to a spatially inhomogeneous recombination current. A transport model for locally contacted solar cells therefore has to consider three dimensions in space to describe both, lateral current flow and current flow perpendicular to the surface. Finite element device simulation programs, such as SENTAURUS have thus been commonly used for optimizing the geometry of local base contact schemes to achieve both, a low series resistance and a low overall rear surface recombination velocity [41, 46, 47]. Another technique was used by Rau, who developed a three-dimensional transport model based on the Fourier decomposition of the transport equations [48].

Analytic solutions of the transport problem can be derived for particular contact layouts, like narrow-spaced or widely-spaced dot- or stripe-shaped contacts. Fischer developed a closed analytic expression for the base saturation current density of a locally contacted solar cell, that holds particularly for small lateral dimensions and narrow spacing of the local contacts when compared to the thickness of the cell [49]. The derivation of his model is sketched in Section 2.6.2. In Section 2.6.3 Fischer's theory is adapted to the case of widely-spaced, large contacts. In Section 2.6.5 the large-scale and the small-scale approximation are combined to a model that holds in both extreme cases, and analytically approximates the base saturation current density, for arbitrary recombination rates in the passivated and the metalized rear surface areas.

The model requires the calculation of the series resistance from the locally contacted rear side to the  $pn$ -junction of the solar cell. Analytic approximations of the series resistance are shown for dot- and stripe-shaped contacts in Section 2.6.4. The experimental verification of the model is performed using a-Si:H for surface passivation, and is the topic of Section 3.3.

### 2.6.1 Definition of the problem

For a full-area contacted solar cell with a spatially homogeneous rear surface recombination velocity  $S$ , the carrier transport is one-dimensional, and the base saturation current density in  $lli$  condition can be rewritten from Equation 2.28

[50, 35]:

$$J_{0b} = \frac{qDn_0}{L_b} \frac{SL_b + D \tanh(W/L_b)}{D + SL_b \tanh(W/L_b)} = \frac{qDn_0}{L_{\text{eff}}} \quad (2.31)$$

with  $D$  being the minority carrier diffusion constant,  $n_0 = n_i^2/N_{\text{dop}}$  the equilibrium minority carrier density, and  $L_{\text{eff}}$  the effective diffusion length. All recombinative losses in the base are lumped in the base saturation current density, which determines the current-voltage characteristics after Equations 2.25 and 2.26. Carrier recombination at the rear surface controls the rear SRV  $S$ , and carrier recombination in the bulk controls the bulk diffusion length  $L_b$ .

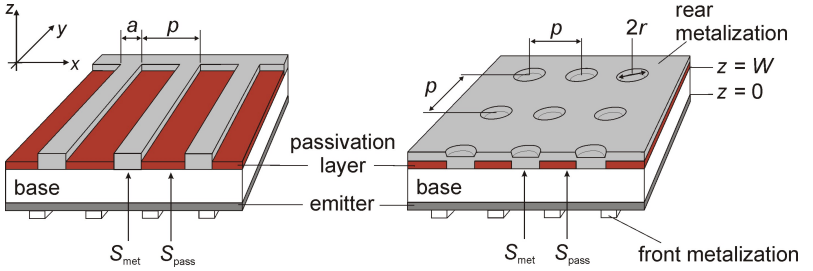


Figure 2.3: *Schematic structure of solar cells with passivated rear side and (a) stripe-contacts or (b) dot-contacts.*

Figure 2.3 schematically sketches two solar cells with their locally contacted rear sides facing upwards. The contacted fraction of the device area is  $f_{\text{stripes}} = a/p$  for the stripe contacts, and  $f_{\text{dots}} = \pi r^2/p^2$  for the dot contacts, with  $p$  being the period length of the contact pattern,  $a$  being the stripe width, and  $r$  being the dot radius.  $S_{\text{pass}}$  is the carrier recombination velocity of the passivated surface area between the contacts, and  $S_{\text{met}}$  is the SRV of the area below the contacts. The surface parameters  $S_{\text{pass}}$ ,  $S_{\text{met}}$ ,  $f$ , and  $p$  control the overall carrier recombination rate at the rear surface, and thus the base saturation current density  $J_{0b}$ .

The base saturation current density is determined by the effective carrier diffusion length  $L_{\text{eff}}$  in the base, as shown in Equation 2.31. The effective diffusion length can also be obtained in case of a spatially inhomogeneous rear SRV, by solving the minority carrier diffusion equation in dark conditions, i. e. without carrier generation,

$$\nabla^2 n(\mathbf{r}) - \frac{n(\mathbf{r})}{L_b^2} = 0 \quad (2.32)$$

with boundary conditions that comply with the contact design of the solar cell [36]. In case of a large bulk diffusion length compared to the thickness of the base,

$L_b/W \rightarrow \infty$ , Equation 2.32 simplifies to the Laplace equation

$$\nabla^2 n(\mathbf{r}) = 0. \quad (2.33)$$

However, numerical techniques are necessary to solve even Equation 2.33 for an arbitrary set of boundary conditions, if the current flow in the solar cell is more than one-dimensional. A theoretical model of the saturation current density  $J_{0b}$  as a function of  $S_{\text{pass}}$ ,  $S_{\text{met}}$ ,  $f$ , and  $p$  is therefore required to predict the impact of the rear contact geometry on the efficiency potential of a solar cell.

Schöfthaler found a scaling law that permits the calculation of the base saturation current of locally contacted solar cells with  $L_b \gg W$ , in two extreme cases [51]:

- In the **small-scale limit**, where the period length of the contact layout is much smaller than the thickness of the base,  $p \ll W$ , the excess carrier concentration at the rear surface is spatially homogeneous, and the base saturation current  $J_{0b}$  is therefore determined by the area-averaged rear surface recombination velocity,  $S_{\text{eff}} = fS_{\text{met}} + (1 - f)S_{\text{pass}}$ , via the Equation 2.31.
- In the **large-scale limit**, where both the contact spacing and the lateral dimensions of the contacts are larger than the base thickness ( $p, a \gg W$  for contact stripes and  $p, 2r \gg W$  for contact dots), lateral current flow is negligible. The solar cell can be therefore described as two diodes connected in parallel: One with the area fraction  $f$  and the rear SRV  $S_{\text{met}}$ , and another one with the area fraction  $(1 - f)$  and the rear SRV  $S_{\text{pass}}$ . In this case, the base saturation current is the area-weighted sum of the base saturation currents  $J_{0b,\text{met}}$  and  $J_{0b,\text{pass}}$  that are calculated from  $S_{\text{met}}$  and  $S_{\text{pass}}$  by the Equation 2.31:  $J_{0b} = fJ_{0b,\text{met}} + (1 - f)J_{0b,\text{pass}}$ .

The model for the saturation current density  $J_{0b}$  that is derived in the following Sections interpolates between the small-scale case, and the large-scale case.

### 2.6.2 Previous work: small-scale case

Fischer developed a fully analytic technique to calculate the base saturation current density of a locally contacted solar cell that holds independently of the lateral contact sizes and period length of the contact layout, if the following requirements are fulfilled [49]:

1.  $S_{\text{pass}} = 0$ : Ideal passivation of the surface areas between the local contacts.
2.  $L_b \gg W$ : Large bulk diffusion length when compared to the thickness of the base.

3. The emitter is approximated by an equipotential surface, which means that the sheet resistance of the emitter is negligible, and therefore no lateral voltage drop occurs.

Fischer's idea was to solve the two-dimensional transport problem by exploiting the formal equivalence between two physically very different entities [49]: (i) The minority carrier concentration  $n(\mathbf{r})$  under reverse injection in the dark, which is determined by Equation 2.33, and (ii) the electrostatic potential  $\Psi(\mathbf{r})$  that drives the majority carrier current. Both,  $n(\mathbf{r})$  and  $\Psi(\mathbf{r})$  are determined by the Laplace equation with equivalent boundary conditions, if the requirements 1–3 are fulfilled. This formal equivalence permits to express the base saturation current density  $J_{0b}$  in terms of the series resistance  $R_b$  for the majority carrier current in the base, and in terms of the SRV  $S_{\text{met}}$  of the surface area below the contacts:

$$J_{0b,\text{cont}} = qDn_0 \left( \frac{R_b}{\rho} + \frac{D}{fS_{\text{met}}} \right)^{-1}. \quad (2.34)$$

The index “cont” denotes that the model includes only carrier recombination below the contacts, and neglects recombination in the passivated rear surface areas ( $S_{\text{pass}} = 0$ ). Although the model was originally only developed for dot-like rear contacts, Equation 2.34 holds independently of the actual contact geometry, which enters only indirectly via the metalized surface fraction  $f$  and the resistance term  $R_b$ .

The resistance term  $R_b$  is defined as the series resistance from the locally contacted rear surface of the base with thickness  $W$  and resistivity  $\rho$ , to an equipotential surface at the front side of the base (which is the idealized emitter). Per definition, all local rear contacts have the same electrostatic potential, in order to ensure that the majority-carrier current-flow pattern that defines the series resistance  $R_b$ , is the same as the flow pattern of the diffusion-driven minority carrier current. A simple way to experimentally deduce  $R_b$  is to prepare a wafer of the same resistance and thickness as the base, with local contacts on one side, and with a full-area ohmic contact on the opposite side that represents the equipotential surface.

### Effective rear surface recombination velocity

If the bulk diffusion length is large,  $L_b \gg W$ , as is the case in Fischer's approximation, Equation 2.31 simplifies to

$$J_{0b} = qDn_0 \frac{S}{D + WS}. \quad (2.35)$$

Analogously to Equation 2.35, Fischer defines the *effective* rear surface recombination velocity of a locally contacted solar cell,

$$S_{\text{cont}} := \left( \frac{qn_0}{J_{0\text{b,cont}}} - \frac{W}{D} \right)^{-1}, \quad (2.36)$$

which lumps all surface recombination paths of one particular rear surface design. The value of  $S_{\text{cont}}$  depends on the contact geometry via the series resistance term  $R_{\text{b}}$ , just like the diode saturation current density.

Although Equation 2.36 was derived only for negligible bulk recombination,  $L_{\text{b}} \gg W$ , Fischer proposed to approximate the diode saturation current density of a solar cell with non-negligible bulk recombination ( $L_{\text{b}} \leq W$ ) by first calculating  $S_{\text{cont}}$  from the Equations 2.34 and 2.36, where bulk recombination is neglected. The obtained value is then used to calculate the total base saturation current density  $J_{0\text{b}}$  from the one-dimensional Equation 2.31. This method accounts for both, laterally inhomogeneous rear surface recombination and carrier recombination in the bulk, in the calculation of the diode saturation current density. The accuracy is better than  $\pm 5\%$  when compared to saturation currents obtained with Rau's three-dimensional Fourier-decomposition method [48, 49].

### Approximation of the base saturation current in the small-scale case

Equation 2.34 accounts only for carrier recombination below the local base contacts, while the recombination rate at the passivated rear surface areas is neglected. However, even well-passivated surfaces contribute to the saturation current, and it is therefore desirable to have a model that accounts also for a non-vanishing recombination rate at the passivated rear surface areas,  $S_{\text{pass}} > 0$ . In order to include carrier recombination ( $S_{\text{pass}} > 0$ ) in the passivated rear surface areas in the model, Fischer approximated the effective rear SRV by adding the area-weighted SRV of the passivated regions to  $S_{\text{cont}}$ ,

$$S_{\text{eff,small}} = S_{\text{cont}} + (1 - f) S_{\text{pass}}, \quad (2.37)$$

which is correct in the small-scale case  $p \ll W$ , where  $S_{\text{cont}} = f S_{\text{met}}$  (see Section 2.6.4 for the calculation of  $R_{\text{b}}$ ). The base saturation current is calculated analogously to Equation 2.35,

$$J_{0\text{b,small}} = qDn_0 \frac{S_{\text{eff,small}}}{D + WS_{\text{eff,small}}}. \quad (2.38)$$

The Equation 2.37 was shown in Reference [49] to deviate less than 1% from effective SRVs that were obtained by Rau's three-dimensional Fourier-transform method, even if the period length  $p$  is of the same order as the base thickness  $W$ ,

as long as the contact coverage is smaller than  $f < 50\%$ , and  $S_{\text{met}} > S_{\text{pass}}$ . However, Equation 2.37 fails in the large-scale case  $p \gg W$ , where the recombination currents of the passivated and non-passivated areas add, and not the recombination velocities. Fischer's model therefore covers the range from small-scale,  $p \ll W$ , to  $p \approx W$ .

### 2.6.3 Parallel-diode approximation: large-scale case

Figure 2.4a shows the sketch of a solar cell with its locally contacted rear side facing upwards. The local surface recombination velocities are  $S_{\text{met}}$  below the contacts, which cover a fraction  $f = a/p$  of the rear surface, and  $S_{\text{pass}}$  in the passivated surface areas, which cover the fraction  $(1 - f) = (p - a)/p$  of the rear surface. The busbar is not shown for the sake of simplicity.<sup>1</sup>

If bulk recombination is neglected ( $L_b/W \rightarrow \infty$ ), the total recombination current that flows through the rear surface is the sum of the recombination current through the surface areas below the local contacts, and of the recombination current through the passivated rear surface areas. The total base saturation current density is therefore, after Equation 2.26,

$$J_{0b} = J_{0b,f} + J_{0b,(1-f)}, \quad (2.39)$$

where  $J_{0b,f}$  lumps all carrier recombination below the contacts that cover the area fraction  $f$ , and the saturation current density  $J_{0b,(1-f)}$  lumps all carrier recombination at the passivated rear surface areas that cover the area fraction  $(1 - f)$ .

Equation 2.39 holds independently of the lateral sizes and period length of the contact layout. However, exact analytic solutions for the contributions  $J_{0b,f}$  and  $J_{0b,(1-f)}$  exist only if the passivated rear surface areas and the contact-covered parts can be regarded as separate diodes that are connected in parallel. That is the case in the large-scale limit when both the contact spacing and the lateral contact dimensions are large compared to the thickness of the base,  $p, a \gg W$  for stripe-shaped contacts and  $p, 2r \gg W$  for dot-shaped contacts. In this case,  $J_{0b,f} = f J_{0b,\text{met}}$  and  $J_{0b,(1-f)} = (1 - f) J_{0b,\text{pass}}$ .

The idea of the **parallel-diode model** is to approximate the minority carrier concentration  $n(\mathbf{r})$  of the solar cell shown in Figure 2.4a, by the sum (modulo the carrier concentration at the  $pn$ -junction  $n_0 \exp(-qV/kT)$ ) of the carrier concentrations of two separate diodes that only show carrier recombination either (i) at the local contacts ( $S_{\text{pass}} = 0$ ,  $S_{\text{met}} > 0$ ) or (ii) at the passivated surface areas ( $S_{\text{pass}} > 0$ ,  $S_{\text{met}} = 0$ ). These two hypothetical devices are sketched in Figures

<sup>1</sup>The derivation of the model is independent of the contact geometry. However, the illustrations shown in this Section are restricted to a stripe-contact layout to provide more clarity.

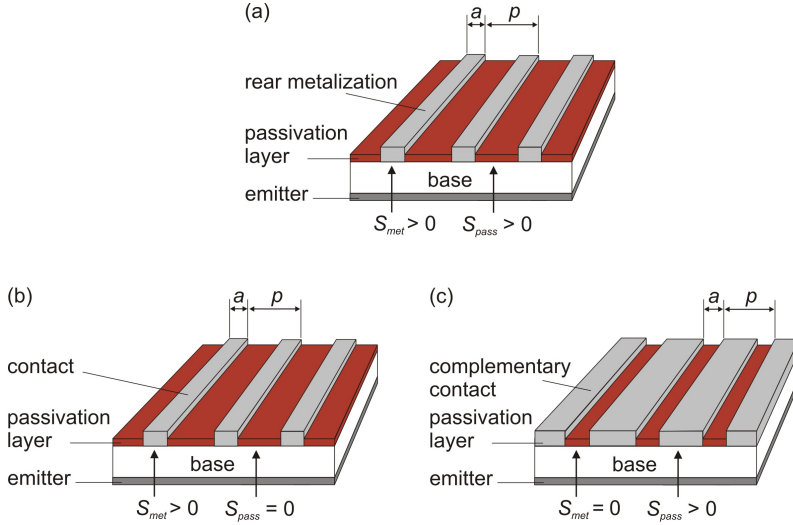


Figure 2.4: (a) Sketch of a solar cell with its stripe-contacted rear side facing upwards. The SRV below the contacts is  $S_{met} > 0$ , and  $S_{pass} > 0$  in between the contacts. (b) The same device as in (a), featuring no carrier recombination in the non-metalized part of the rear surface. (c) Diode with a metalization scheme that is complementary to the one in (a). The SRV below the contacts is  $S_{pass} > 0$ , and  $S_{met} = 0$  in between the contacts.

2.4b and 2.4c, respectively. Due to the linearity of the Laplace equation 2.33, the recombination current of the solar cell shown in Figure 2.4a is then the sum of the recombination currents of the devices shown in the Figures 2.4b and 2.4c.

Therefore, the model allows to separate the contributions  $J_{0b,f}$  and  $J_{0b,(1-f)}$  to the total base saturation current density according to Equation 2.39:

- $J_{0b,f}$  is approximated by the base saturation current density of the device shown in Figure 2.4b, because this device exhibits only carrier recombination in the metalized rear surface areas, and
- $J_{0b,(1-f)}$  is approximated by the base saturation current density of the device shown in Figure 2.4c, because this device features only carrier recombination in those rear surface areas that are non-metalized in the original solar cell.

### Contribution of the metalized areas to the base saturation current

Figure 2.4b shows a device that features carrier recombination only below the contact stripes, where the local SRV is  $S_{\text{met}} > 0$ . The local SRV of the passivated rear surface areas is  $S_{\text{pass}} = 0$ . The device therefore fulfills the requirements for Equation 2.34 to be valid, and its base saturation current density is

$$J_{0\text{b,cont}} = qDn_0 \left( \frac{R_{\text{b}}}{\rho} + \frac{D}{fS_{\text{met}}} \right)^{-1}. \quad (2.40)$$

The saturation current density  $J_{0\text{b},f}$  is approximated by  $J_{0\text{b,cont}}$  in the model,

$$J_{0\text{b},f} \approx J_{0\text{b,cont}}, \quad (2.41)$$

as described above.

### Contribution of the passivated areas to the base saturation current

The contribution of carrier recombination at the passivated rear surface areas to the total base saturation current density is denoted by  $J_{0\text{b},(1-f)}$ . It is approximated by the saturation current density of a device that features *only* recombination at the passivated fraction of the surface ( $S_{\text{pass}} > 0$ ), and no recombination below the metalization ( $S_{\text{met}} = 0$ ). In order to apply Equation 2.34 to such a device, the series resistance term  $R_{\text{b}}$  has to be calculated as if the area that shows the non-vanishing SRV, was electrically contacted. The local contacts and the non-contacted regions of the original solar cell shown in Figure 2.4a are therefore simply interchanged, and a contact layout that is complementary to the original one results. However, the allocation of the SRVs  $S_{\text{met}}$  and  $S_{\text{pass}}$  to the respective regions of the rear surface of the device, is the same as in the original cell.

Figure 2.4c shows a device with the complementary rear side layout, where contacted and non-contacted parts are interchanged. The “complementary contacts” cover the fraction  $(1 - f) = (p - a) / p$  of the rear surface area. By definition, the SRV below the complementary contacts is  $S_{\text{pass}} > 0$ , and no carrier recombination occurs in the non-contacted areas ( $S_{\text{met}} = 0$ ). The base saturation current density of the complementary structure is then calculated analogously to Equations 2.40 and 2.41:

$$J_{0\text{b},(1-f)} \approx qDn_0 \left( \frac{\tilde{R}_{\text{b}}}{\rho} + \frac{D}{(1-f)S_{\text{pass}}} \right)^{-1}. \quad (2.42)$$

The series resistance term  $\tilde{R}_{\text{b}}$  is defined analogously to  $R_{\text{b}}$  as the resistance from the rear surface featuring the complementary contact geometry, to an equipotential surface at the front side of the base.



### Total base saturation current

The total base saturation current  $J_{0b}$  is calculated from Equation 2.39 as the sum of the approximations for  $J_{0b,f}$  and  $J_{0b,(1-f)}$  given by the Equations 2.41 and 2.42,

$$J_{0b,\text{large}} = qDn_0 \left[ \left( \frac{R_b}{\rho} + \frac{D}{fS_{\text{met}}} \right)^{-1} + \left( \frac{\tilde{R}_b}{\rho} + \frac{D}{(1-f)S_{\text{pass}}} \right)^{-1} \right]. \quad (2.43)$$

The corresponding effective rear surface recombination velocity  $S_{\text{eff}}$  is defined analogously to Equation 2.35,

$$S_{\text{eff},\text{large}} = \left( \frac{qn_0}{J_{0b,\text{large}}} - \frac{W}{D} \right)^{-1}. \quad (2.44)$$

Equations 2.38 and 2.43 hold independently of the actual contact geometry, which enters only implicitly via the metalized fraction  $f$  of the rear surface, and the series resistance terms  $R_b$  and  $\tilde{R}_b$ . Therefore, all that is needed for calculating the diode saturation current density  $J_{0b}$  are analytic approximations for the base series resistance  $R_b$  of dot- and stripe-contacted solar cells, and of the respective resistances  $\tilde{R}_b$  of the complementarily contacted structures.

The parallel-diode approximation is designed to be valid in the mid- to large-scale range,  $p \approx W$  to  $p \gg W$ , that is not covered by the approach shown in Section 2.6.2. Since Equation 2.34 is used for the approximations of  $J_{0b,f}$  and  $J_{0b,(1-f)}$ , the requirements 2 and 3 of Fischer's model shown in Section 2.6.2 also hold for this model, i. e. the bulk diffusion length is assumed to be large compared to the base thickness,  $L_b \gg W$ , and the emitter is approximated by an equipotential surface.

#### 2.6.4 Model for the base series resistance

The base series resistance  $R_b$  is defined as the electrical resistance from the locally contacted rear surface of the base, to an equipotential surface at the front side of the base (which approximates a highly conductive emitter). Since a full-area metallic contact at the front surface of the base also forms an equipotential surface, a simplified structure is used as a model for the calculation of  $R_b$ : A wafer of the same resistance  $\rho$  and thickness  $W$  as the base, with local contacts on one side and with a full-area contact on the other side, as shown in Figure 2.5.

Following previous work [49], the base series resistance is approximated regardless of the specific dot- or stripe-contact geometry by

$$R_b = \rho W (1 - e^{-W/p}) + A_{\text{unit}} R_{\text{spreload}}, \quad (2.45)$$

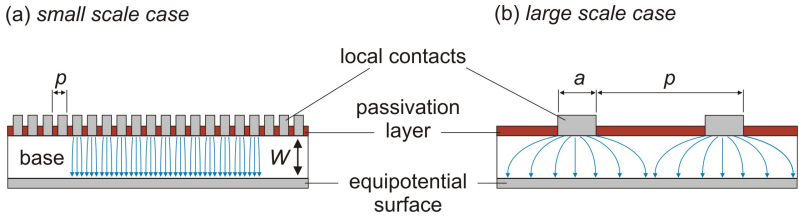


Figure 2.5: *Cross-sectional view of a wafer with local contacts on one side, and a full-area contact (equipotential surface) on the opposite side. The series resistance across the wafer is  $R_b$ . (a) Small-scale case ( $p \ll W$ ):  $R_b$  is determined by the resistivity  $\rho$  of the wafer. (b) Large-scale case ( $p \gg W$ ):  $R_b$  is determined by the spreading resistance  $R_{\text{spread}}$ . The current flow is sketched by blue lines in both cases.*

where  $\rho$  and  $W$  are the resistivity and the width of the base, respectively. The spreading resistance  $R_{\text{spread}}$  is defined as the resistance from a single disk- or stripe-shaped contact on one side of an infinitely extended conducting slab, to the full-area contacted opposite side [52]. The unit area  $A_{\text{unit}}$  of the contact pattern is  $A_{\text{unit}} = lp$  for a pattern of equidistant contact stripes with spacing  $p$  and length  $l$ , and  $A_{\text{unit}} = p^2$  for a square pattern of dot contacts. Equation 2.45 results in the specific base series resistance in  $[\Omega\text{cm}^2]$ , which is independent of the actual size of the solar cell. All that is needed to calculate the base series resistance is therefore the spreading resistance of the respective rear contact design.

Equation 2.45 interpolates between the two asymptotic limits for the base series resistance, the “small-scale case”,  $p \ll W$ , and the “large-scale case”,  $p \gg W$ . The **small-scale case** is represented by the first term on the right-hand side: If the contact spacing is small compared to the width of the base, the current will flow only perpendicular to the wafer surface, as is sketched in Figure 2.5a. The current flow pattern is therefore the same as in a full-area contacted wafer [49]. The base series resistance is then determined by Ohm’s law, and approaches

$$R_b = \rho W \quad \text{for } p \ll W, \quad (2.46)$$

regardless of the coverage  $f$  of the local contacts.<sup>1</sup>

The **large-scale case** is represented by the second term on the right hand side of Equation 2.45. If the contact spacing is large compared to the thickness of the base,  $p \gg W$ , the current paths from neighboring contacts towards the front

<sup>1</sup>The contact resistivity from metal to semiconductor is not accounted for in this model.

surface do not interfere, as sketched in Figure 2.5b. The base series resistance in the large scale case,

$$R_b = A_{\text{unit}} R_{\text{spread}} \quad \text{for } p \gg W, \quad (2.47)$$

is then determined by the spreading resistance and by the contact spacing. However, the contact width  $a$  must increase with increasing contact spacing  $p$ , for a given contact coverage  $f$ , and the spreading resistance eventually approaches its geometrical limit

$$R_{\text{spread}} = \frac{\rho W}{A_{\text{contact}}} = \frac{\rho W}{f A_{\text{unit}}} \quad \text{for } p, a \gg W, \quad (2.48)$$

because the effect of the current “spreading” in the edge region of the contact becomes negligible due to the increasing lateral dimensions of the contact [52]. The base series resistance in the large-scale limit therefore finally approaches

$$R_b = \frac{\rho W}{f} \quad \text{for } p, a \gg W, \quad (2.49)$$

which can be simply understood as the contacted and non-contacted areas of the base being connected in parallel. Any approximative analytic model for the spreading resistance must therefore satisfy Equation 2.48 to be suitable for modeling the base series resistance, and hence the base saturation current of locally contacted solar cells.

The base series resistance  $R_b$  approximates the contribution of carrier transport in the base, to the total series resistance  $R_s$  of a non-illuminated solar cell. In order to model the total series resistance of a solar cell, the contribution of carrier transport in the emitter, the resistances of the contact grids, the contact resistances to the emitter and the base, as well as the impact of illumination on the series resistance have to be considered. Former investigations showed that the base series resistance of high-efficiency PERC solar cells is mostly independent of the actual illumination intensity and operating point of the cell, since the current-flow pattern is governed by spreading resistance and not by injection effects [46, 53, 34]. Thus,  $R_b$  may also be considered as an approximation for the base series resistance under illumination.

### Base series resistance for stripe-shaped contacts

In case of equidistantly spaced, stripe-shaped rear contacts, an analytic approximation for the spreading resistance is used that was derived by Gelmont and Shur [54, 55],

$$R_{\text{spread,stripe}} = \frac{\rho}{2l} \gamma(\alpha) \quad \text{with } \alpha = \frac{\pi a}{4W}, \quad (2.50)$$

where

$$\gamma(\alpha) = \frac{K(1/\tanh\alpha)}{K(\tanh\alpha)}, \quad (2.51)$$

and  $l$  is the length of the contact stripes. The function  $K$  is the complete elliptic integral of the first kind. Its solution can be looked up, e.g. in Reference [56]. However, the function  $\gamma(\alpha)$  is approximated analytically following Reference [55], in order to provide a fully analytic model for the diode saturation current in this work:

$$\begin{aligned} \gamma(\alpha) &= \frac{1}{\pi} \ln \left( \frac{2(\sqrt{\cosh\alpha} + 1)}{\sqrt{\cosh\alpha} - 1} \right) && \text{if } \tanh\alpha \leq \frac{1}{\sqrt{2}}, \\ \gamma(\alpha) &= \pi \left[ \ln \left( \frac{2(1 + \sqrt{\tanh\alpha})}{1 - \sqrt{\tanh\alpha}} \right) \right]^{-1} && \text{if } \frac{1}{\sqrt{2}} < \tanh\alpha < 1. \end{aligned} \quad (2.52)$$

The base series resistance for a pattern of equidistant contact stripes is then obtained from Equation 2.45,

$$R_{b,\text{stripes}} = \rho W (1 - e^{-W/p}) + \frac{p\rho}{2} \gamma(\alpha), \quad (2.53)$$

where the contacts are assumed to extend until the edges of the device, as shown in the inset of Figure 2.6. The series resistance  $R_{b,\text{stripes}}$  is therefore independent of the length  $l$  of the stripes.

Figure 2.6 shows  $R_{b,\text{stripes}}$  for contact coverages  $f = 1\%$  and  $10\%$  of the rear side of the base, in the range  $10^{-3} < p/W < 10^3$ . In the large scale-limit  $p, a \gg W$ , Equations 2.50 and 2.52 lead to

$$R_{\text{spread,stripe}} = \frac{\rho W}{lpf} \quad \text{for } p, a \gg W, \quad (2.54)$$

and thus  $R_{b,\text{stripes}} = \rho W/f$ , as is demanded by Equation 2.49. In the small-scale limit, the base series resistance is  $R_{b,\text{stripes}} = \rho W$  for all contact coverages  $f$ , as described above.

Therefore, Equations 2.50, 2.52, and 2.53 provide an analytic model for the base series resistance of locally stripe-contacted solar cells, that holds analytically exact in both, the small-scale limit and the large-scale limit.

The series resistance  $\tilde{R}_{b,\text{stripes}}$  of the **complementary contact layout** is needed together with  $R_{b,\text{stripes}}$  to calculate the base saturation current density of a stripe-contacted solar cell from Equation 2.43. The calculation of  $\tilde{R}_{b,\text{stripes}}$  is simple in case of stripe-contacts, because the complementary structure consists again of equidistant stripes, as is illustrated in Figure 2.4. Therefore, Equation 2.53 also

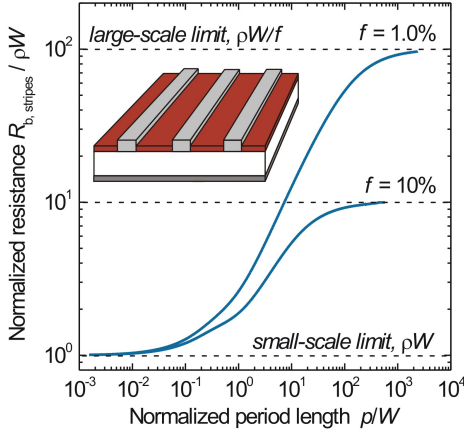


Figure 2.6: Normalized base series resistance  $R_b/\rho W$  for stripe contacts, as a function of the normalized spacing  $p/W$  of the contact stripes.

holds for the complementary-contact structure, if the stripe width  $a$  is replaced by  $(p - a)$ :

$$\tilde{R}_{b,\text{stripes}} = \rho W \left(1 - e^{-W/p}\right) + \frac{p\rho}{2} \gamma(\tilde{\alpha}) \quad \text{with} \quad \tilde{\alpha} = \frac{\pi(p-a)}{4W}. \quad (2.55)$$

Again, Equation 2.55 interpolates between the small-scale case

$$\tilde{R}_{b,\text{stripes}} = \rho W \quad \text{for} \quad p \ll W, \quad (2.56)$$

and the large-scale case

$$\tilde{R}_{b,\text{stripes}} = \frac{\rho W}{1-f} \quad \text{for} \quad p, (p-a) \gg W, \quad (2.57)$$

as demanded by the Equations 2.46 and 2.49.

### Base series resistance for dot-shaped contacts

In case of dot-shaped base contacts, an approximation for the spreading resistance  $R_{\text{spread,dot}}$  is used that was derived by Fischer [49]:

$$R_{\text{spread,dot}} = \rho \left[ \left(\frac{1}{4r}\right)^{-n} + \left(\frac{W}{\pi r^2}\right)^{-n} \right]^{-1/n}, \quad (2.58)$$

where  $r = p \sqrt{f/\pi}$  is the radius of the contact dot. Equation 2.58 approximates the exact solution that was found by Brooks and Mattes [52], but which has to be solved numerically. Reference [49] shows that the relative deviation of Equation 2.58 from the exact solution by Brooks and Mattes, is less than 2% for all values of the dot radius  $r$ . The smallest deviation is achieved with  $n = 1.72$ , which is therefore used throughout this work. Equation 2.58 interpolates the spreading resistance between the two asymptotes for small radius  $r \ll W$  where  $R_{\text{spread,dot}} = \rho/4r$ , and for large radius compared to the wafer width,  $r \gg W$ , where the spreading resistance approaches its geometrical limit  $R_{\text{spread,dot}} = \rho W/\pi r^2$  [52].

The base series resistance for a square pattern of circular contact dots is then, after Equation 2.45,

$$R_{\text{b,dots}} = \rho W (1 - e^{-W/p}) + p^2 R_{\text{spread,dot}}, \quad (2.59)$$

which is shown in Figure 2.7a as a function of the ratio of period length  $p$  to wafer thickness  $W$ , for coverages  $f = 1\%$  and  $10\%$ .

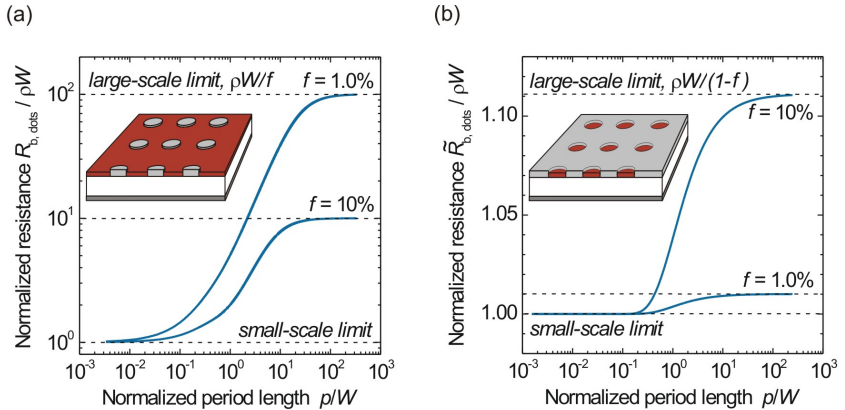


Figure 2.7: (a) Normalized base series resistance  $R_{\text{b}}/\rho W$  for dot-shaped contacts in a square pattern, as a function of the normalized period length  $p/W$ . (b) Base series resistance  $\hat{R}_{\text{b}}/\rho W$  for the complementary contact layout.

Just like the approximative formula for stripe contacts, Equation 2.59 meets the asymptotic limits of the small-scale case,

$$R_{\text{b,dots}} = \rho W \quad \text{for} \quad p \ll W, \quad (2.60)$$

and in the large-scale case,

$$R_{\text{b,dots}} = \frac{\rho W}{f} \quad \text{for } p, 2r \gg W, \quad (2.61)$$

as demanded by the Equations 2.46 and 2.49.

The accuracy of Equation 2.59 was checked in Reference [49] against three-dimensional modeling of the base series resistance using the Fourier transform method [48]. A maximum deviation of less than 2% was obtained for  $f \leq 10\%$ , and  $10^{-2} < p/W < 10^3$ . Commonly applied metal coverages are below  $f \leq 5\%$  for high-efficiency solar cells [44, 47], which means that the Equations 2.58 and 2.59 represent a generally valid analytic model for the base series resistance of dot-contacted solar cells.

The series resistance  $\tilde{R}_{\text{b,dots}}$  of the **complementary contact layout** has to be calculated for a device that features a rear-side contact that is perforated with holes of spacing  $p$  and radius  $r$  in the place of the original contact dots, as shown in the inset of Figure 2.7b. Since this contact structure is connected over the whole device area, and thus cannot be separated into local contacts featuring a simple symmetry like stripes or dots,  $\tilde{R}_{\text{b,dots}}$  cannot be calculated via the spreading-resistance approach from Equation 2.45. However, the reasoning which leads to the Equations 2.46 and 2.47 that describe the small-scale and large-scale limits of the base series resistance, holds independently of the rear contact geometry. Obviously, the current flow from the rear surface to the front surface will be parallel for  $p \ll W$  as sketched in Figure 2.5a, which leads to the small-scale limit

$$\tilde{R}_{\text{b,dots}} = \rho W \quad \text{for } p \ll W \quad (2.62)$$

of the complementary-contact series resistance. If the period length  $p$  increases such that the distance between the edges of neighboring holes becomes large when compared to the thickness of the wafer,  $(p - 2r) \gg W$ , the contacted and non-contacted areas can be regarded as connected in parallel. The resistance then reaches its large-scale limit

$$\tilde{R}_{\text{b,dots}} = \frac{\rho W}{1 - f} \quad \text{for } p, (p - 2r) \gg W. \quad (2.63)$$

An expression that is similar to Equation 2.45, and interpolates between the small-scale and the large-scale limit is used in this work as an approximation for the base series resistance of the complementary-contact structure in case of dot-contacted solar cells:

$$\tilde{R}_{\text{b,dots}} = \rho W (1 - f e^{-W/p})^{-1}, \quad (2.64)$$

which is shown in Figure 2.7b as a function of the ratio of period length  $p$  to wafer thickness  $W$ , for coverages  $f = 1\%$  and  $10\%$ .

The relative error of the resistance calculated from Equation 2.64 approaches zero in the small-scale case and in the large-scale case, where the value of  $\tilde{R}_{b,dots}$  is independent of the contact layout. The error is  $\Delta\tilde{R}_{b,dots}/\tilde{R}_{b,dots} < (1-f)^{-1}$  in the intermediate range  $p \approx W$ . However, the only use of the parameter  $\tilde{R}_{b,dots}$  in this work is to calculate the contribution  $J_{0b,(1-f)}$  to the base saturation current of dot-contacted solar cells from Equation 2.42, which is robust against variations of  $\tilde{R}_{b,dots}$ . In case of a solar cell with well-passivated base,  $S_{pass} \approx 10^{-2}D/W$  and contact coverage  $f < 10\%$ , which are typical values for high-efficiency solar cells [45, 47], a variation of  $\Delta\tilde{R}_{b,dots}/\tilde{R}_{b,dots} = 10\%$  would result in a variation of the saturation current of only  $\Delta J_{0b,(1-f)}/J_{0b,(1-f)} < 0.1\%$ .

The approximation of  $\tilde{R}_{b,dots}$  by Equation 2.64 is therefore suitable to be used for the calculation of the base saturation current in the analytic parallel-diode model, by the Equation 2.43.

## 2.6.5 Interpolation between small-scale case and large-scale case

The models shown in Sections 2.6.2 and 2.6.3 for the base saturation current density of PERC solar cells, hold only for small or large dimensions of the local base contacts, when compared to the thickness of the cell: Fischer's model (Equation 2.38) holds in the small-scale case of  $p \ll W$ , and the parallel-diode model (Equation 2.43) holds in the large-scale case of  $p, a \gg W$  or  $p, 2r \gg W$ , respectively. However, none of the models holds in both extreme cases, so one has to interpolate between the Equations 2.38 and 2.43 to obtain an approximation for the base saturation current density that is valid, both in the small-scale limit and in the large-scale limit.

### Interpolation method

The small-scale model represented by Equation 2.38 was shown in Reference [49] to deviate less than 1% from saturation currents that were obtained by Rau's three-dimensional Fourier-transform method, in the range from  $p \ll W$  to  $p \approx W$ , and for  $S_{pass} < W/D$ , which is the case in high-efficiency PERC solar cells. The large-scale parallel-diode approximation requires that the metalized and the passivated areas of the solar cell can be regarded as connected in parallel, which is the case if the lateral dimensions of the contacts are large when compared to the thickness of the base:  $x \gg W$ , with  $x = a$  for stripe-shaped contacts, and  $x = 2r$  for dot-shaped contacts.<sup>1</sup>

<sup>1</sup>Actually, both the contact spacing and the contact width must be larger than  $W$ , for the same reasons as discussed in Section 2.6.4. However, a successful contact layout for PERC solar



Therefore, the model proposed in this Section switches from the approximation of  $J_{0b}$  by Equation 2.38 to Equation 2.43 when the lateral size of the local contacts is  $x = W$ :

$$J_{0b} = J_{0b,\text{small}} \times \xi_{\text{small}}(x) + J_{0b,\text{large}} \times \xi_{\text{large}}(x), \quad (2.65)$$

where  $J_{0b,\text{small}}$  and  $J_{0b,\text{large}}$  are defined by Equations 2.38 and 2.43, respectively. The functions  $\xi_{\text{small}}$  and  $\xi_{\text{large}}$  interpolate between 0...1 with  $\xi_{\text{small}} = \xi_{\text{large}} = 0.5$  if  $x = W$ :

$$\begin{aligned} \xi_{\text{small}} &= 0.5 \left[ 1 + \tanh \left( -\ln \frac{x}{W} \right) \right], \text{ and} \\ \xi_{\text{large}} &= 0.5 \left[ 1 + \tanh \left( \ln \frac{x}{W} \right) \right]. \end{aligned} \quad (2.66)$$

## Discussion

The model shown above allows to analytically calculate the base saturation current  $J_{0b}$  of solar cells with passivated, locally contacted rear sides from the Equations 2.65, 2.53, and 2.55 in case of stripe-contacted solar cells, and from the Equations 2.65, 2.59, and 2.64 in case of dot-contacted solar cells. The model requires that bulk recombination is negligible,  $L_b \gg W$ .

Figure 2.8 shows the base saturation current density of stripe-contacted solar cells as a function of the period length  $p$ , and of the contact coverage  $f$ . Dimensionless expressions for the surface recombination velocity  $s = SW/D$  and for the diode saturation current  $j_0 = J_0 W (qDn_0)^{-1}$  are introduced in order to discuss the results of the model independently of the dopant type, the resistivity, and the thickness of the base. In case of negligible bulk recombination, the Equation 2.35 then simplifies to

$$j_{0b} = \frac{s_{\text{eff}}}{1 + s_{\text{eff}}}, \quad (2.67)$$

where  $s_{\text{eff}}$  is the effective rear surface recombination velocity times  $W/D$ .

Figure 2.8a illustrates the interpolation between the small-scale part and the large-scale part of Equation 2.65. It shows the base saturation current density  $j_{0b}$  of stripe-contacted solar cells as a function of the normalized period length  $p/W$ . The local surface recombination velocities are chosen such that the deviations of the parallel-diode approximation from the small-scale limit, and of Fischer's model from the large-scale limit, become obvious. The value  $s_{\text{met}} = 100$  corresponds to a non-passivated crystalline silicon surface,  $S_{\text{met}} = 10^5$  cm/s for a 300  $\mu\text{m}$ -thick  $p$ -type wafer with  $p = 10^{16}$   $\text{cm}^{-3}$ .

---

cells features in any case  $f < 10\%$  to achieve a low surface recombination rate. Therefore  $x \gg W$  implies that the spacing is  $(p - x) \gg W$ .

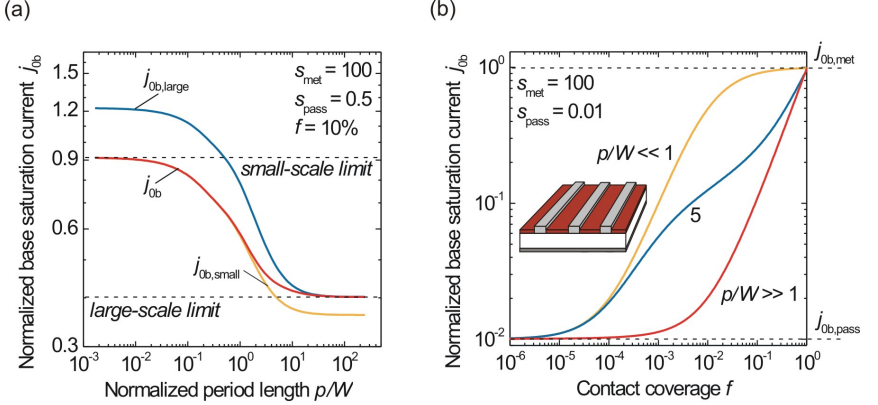


Figure 2.8: Normalized base saturation current density  $j_{ob} = J_{ob}W (qDn_0)^{-1}$  calculated for stripe-shaped contacts. (a) Saturation current densities as a function of the normalized period length  $p/W$ . The parallel-diode approximation  $j_{ob,large}$  is shown as the blue curve, and Fischer's model  $j_{ob,small}$  as the orange curve. The base saturation current density  $j_{ob}$  (red curve) that is calculated from Equation 2.65, meets both asymptotic limits for  $p \ll W$  and for  $p \gg W$ . (b) Base saturation current density  $j_{ob}$  as a function of the contact coverage  $f$ . The contact spacing is varied from small-scale to large-scale. A typical value for high-efficiency PERC solar cells is  $p \approx 5W$ .

The limits for the base saturation current density can be calculated independently of the contact layout: In the **small-scale limit**  $p \ll W$ , the carrier concentration at the rear surface becomes spatially homogeneous, so that the diffusion equation 2.33 becomes one-dimensional. The effective rear surface recombination velocity is then the area-weighted sum of the local SRVs,

$$s_{eff,small} = fs_{met} + (1-f)s_{pass} \quad \text{if} \quad p \ll W, \quad (2.68)$$

and the respective base saturation current density  $j_{ob,small}$  is given by Equation 2.67. For  $s_{met} = 100$ ,  $s_{pass} = 0.5$ , and  $f = 10\%$ , the result is  $j_{ob,small} = 0.91$ , which is met within  $\pm 0.1\%$  by the interpolation model.

In the **large-scale limit**  $p, x \gg W$ , lateral current flow becomes negligible. The solar cell can be regarded as two diodes connected in parallel: One with rear SRV  $s_{met}$  and area fraction  $f$ , and the other with rear SRV  $s_{pass}$  and area

fraction  $(1 - f)$ . Consequently, the total base saturation current density is the area-weighted sum

$$j_{0b,\text{large}} = f j_{0b,\text{met}} + (1 - f) j_{0b,\text{pass}} \quad \text{if} \quad p, x \gg W, \quad (2.69)$$

where the local base saturation current densities are given by

$$j_{0b,\text{met}} = \frac{s_{\text{met}}}{1 + s_{\text{met}}} \quad \text{and} \quad j_{0b,\text{pass}} = \frac{s_{\text{pass}}}{1 + s_{\text{pass}}}, \quad (2.70)$$

analogously to Equation 2.67. For  $s_{\text{met}} = 100$ ,  $s_{\text{pass}} = 0.5$ , and  $f = 10\%$ , the result is  $j_{0b,\text{large}} = 0.40$ , which is met within  $\pm 0.1\%$  by the interpolation model.

Figure 2.8b shows the base saturation current density  $j_{0b}$  of stripe-contacted solar cells as a function of the contact coverage  $f$ , in the small-scale limit, in the large-scale limit, and for  $p/W = 5$ . The value  $p/W \approx 5$  is typically found for high-efficiency solar cells (e. g.  $p = 1.5 \text{ mm}$  for  $W = 300 \mu\text{m}$ ) [47]. In each case, the base saturation current density is  $j_{0b} = j_{0b,\text{pass}}$  for  $f = 0$ , and  $j_{0b} = j_{0b,\text{met}}$  for  $f = 1$ . In the large-scale limit, the saturation current  $j_{0b}$  is a linear function of the contact coverage  $f$  as shown by Equation 2.69. The curve for  $p/W = 5$  follows the small-scale limit for  $f < 10^{-4}$ , where  $x \ll W$ , and approaches the large-scale limit for  $f \rightarrow 1$ .

Figure 2.8 shows that the base saturation current decreases with increasing contact spacing, for any given contact coverage  $f$ . However, Figures 2.6 and 2.7 show that the base series resistance increases with increasing contact spacing. Since the energy conversion efficiency of a solar cell increases with both, decreasing saturation current, and decreasing resistance, the period length and the contact coverage have to be optimized to achieve the optimum efficiency of PERC solar cells. The model shown in this Section can be used to implement such an optimization routine in one-dimensional device simulations by using the base saturation current and the base series resistance calculated from the Equations 2.65, 2.53, and 2.59, respectively.

Figure 2.9a shows the normalized base saturation current densities  $j_{0b}$  for dot- and stripe-contact layouts, as a function of the period length  $p$ . In both cases, the large-scale limit and the small-scale limit are correctly reproduced by the model. The parameters  $s_{\text{met}} = 10^2$ ,  $s_{\text{pass}} = 10^{-2}$ , and  $f = 5\%$  are chosen to meet typical values of PERC solar cells [47]. The dot-contact layout leads to a base saturation current that is up to a factor of 1.8 smaller than with the stripe-contact layout, when compared at the same period length in the range  $p/W = 1 \dots 10$ .

Figure 2.9b shows the normalized base series resistance  $R_b (\rho W)^{-1}$  for dot- and stripe-contact layouts, as a function of the period length  $p$ , again for  $f = 5\%$ . The base series resistance is larger with the dot-contact layout than with the stripe-contact layout, when compared again at the same period length. The range of

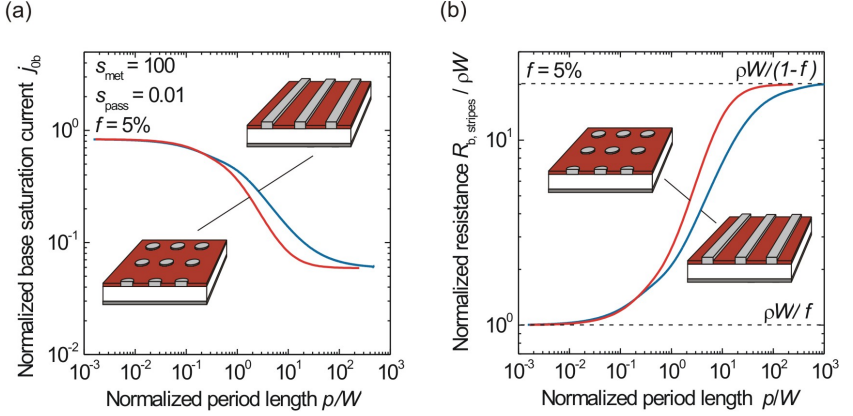


Figure 2.9: (a) Normalized base saturation current  $j_{0b} = J_{0b}W (qDn_0)^{-1}$  for dot- and stripe contacted solar cells. (b) Normalized base series resistance  $R_b (\rho W)^{-1}$  for dot- and stripe-contacted solar cells. Dot-contacted solar cells show a smaller base saturation current density, but a larger base series resistance than stripe-contacted ones with the same contact coverage and period length.

$j_{0b}$  and  $R_b$  that results in the maximum solar cell efficiency for a certain contact coverage  $f$ , is therefore obtained with a smaller period length for dot contacts, than for stripe contacts. This result was also found by Catchpole and Blakers [47], who used finite-element numerical modelling to calculate the efficiency of PERC solar cells as a function of  $f$  and  $p$ . In their calculations, dot- and stripe-contact layouts led to the same maximum efficiency, however at a 2–3 times larger period length for stripe-contacts than for dot-contacts.

## 2.6.6 Conclusion

The model derived in this Section allows to analytically calculate the base saturation current  $J_{0b}$  and the base series resistance  $R_b$  of solar cells with passivated, locally contacted rear sides from the Equations 2.65, 2.53, and 2.55 in case of stripe-contacted solar cells, and from the Equations 2.65, 2.59, and 2.64 in case of dot-contacted solar cells. The results obtained from the model can be used to optimize the rear contact layout for a maximum energy conversion efficiency, in one-dimensional device simulations.

The model is an extension of previous work [49], that allows to fit the asymptotic limits to the base saturation current for  $p \rightarrow 0$ ,  $p \rightarrow \infty$ ,  $f \rightarrow 0$ , and  $f \rightarrow 1$ , as is shown in Section 2.6.5. The experimental verification of the model is shown in Section 3.3, by using amorphous silicon for surface passivation.



## 3 A-Si:H-passivation and contact formation to solar cells: COSIMA

The COSIMA technique (contact formation to a-Si:H-passivated solar cells by means of annealing) which was developed in this work, is a two-step process that comprises (i) the deposition of an amorphous silicon film onto the emitter- and/or the base-side of a solar cell, for surface passivation, and (ii) the deposition and annealing of aluminum, for the formation of local contacts.

This chapter starts with a description of the plasma enhanced chemical vapor deposition system which is used at ISFH for the formation of amorphous silicon (a-Si:H) and silicon nitride ( $\text{SiN}_x$ ) films, in Section 3.1. The quality of the surface passivation by a-Si:H films is reviewed. Section 3.2 shows the mechanism of the COSIMA contact formation. Contact resistivities to lowly- and highly-doped crystalline silicon are determined. The impact of carrier recombination at the surface of the COSIMA-processed, locally contacted base on the base saturation current density, is the topic of Section 3.3.

### 3.1 Deposition parameters

Plasma enhanced chemical vapor deposition (PECVD) is used for the deposition of a-Si:H single films and of a-Si:H/ $\text{SiN}_x$  double layers on monocrystalline silicon solar cells, and on samples designed for the determination of the quality of the surface passivation. The detailed layout of the reactors, and the respective deposition parameters are shown in References [3, 19, 57]. The deposition of a-Si:H films is carried out in an *Oxford Plasma Technology Plasmalab 80* direct-plasma CVD reactor, which is sketched in Figure 3.1a. The plasma is generated by a high-frequency (13.56 MHz) electric field applied between the temperature-controlled sample stage and the perforated upper electrode, through which the  $\text{SiH}_4$  precursor gas enters the reactor. Due to the high plasma frequency, the acceleration periods are too short for the ions in the plasma to cause noticeable surface damage, which is the advantage of this method over the low-frequency plasma excitation [57]. The deposition rate is  $r_{\text{a-Si:H}} = 10 \text{ nm/min}$ .

(a) Direct-PECVD: a-Si:H deposition

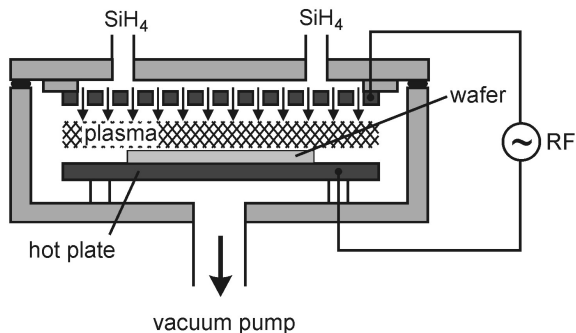
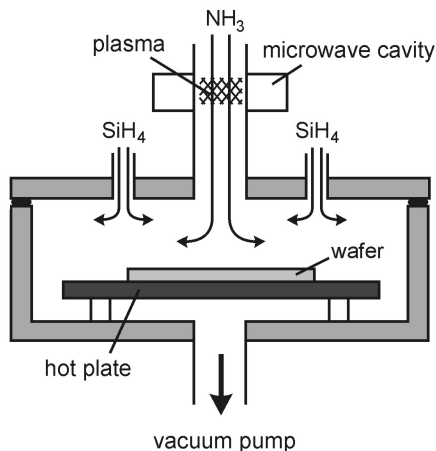
(b) Remote-downstream PECVD:  $\text{SiN}_x$  deposition

Figure 3.1: Sketch of the PECVD reactors used for a-Si:H and  $\text{SiN}_x$  deposition. (a) Direct-plasma enhanced CVD reactor for a-Si:H deposition. The  $\text{SiH}_4$  plasma is generated by the 13.56 MHz electric field applied between the gas inlet and the hot plate. (b) Remote-plasma enhanced CVD reactor for  $\text{SiN}_x$  deposition. The  $\text{NH}_3$  plasma is generated in the microwave resonator outside the reactor. Figures adapted from Reference [58].



The thickness of the deposited a-Si:H layers is determined from cross-sectional scanning-electron micrographs of a-Si:H-covered c-Si wafers. No dopant gases are added during the deposition. Therefore, the amorphous silicon films are nominally intrinsic.

Remote downstream PECVD with microwave excitation in an *Oxford Plasma Technology Plasmalab 80+* reactor is used for the deposition of amorphous, hydrogenated silicon nitride ( $\text{SiN}_x$ ). Figure 3.1b shows a sketch of the reactor. This technique also eliminates the bombardment of the surface by accelerated ions during the deposition, because the  $\text{NH}_3$  plasma is generated in the microwave resonator outside the reactor. The  $\text{SiH}_4$  precursor gas is added downstream.

Table 3.1 shows the parameters used for the low-temperature deposition of the a-Si:H and  $\text{SiN}_x$  films that are investigated in this work. The samples are cleaned in  $\text{NH}_4\text{OH}$ - and in  $\text{HCl}$ -solution prior to the a-Si:H deposition. A 1 min dip in 2% HF immediately before the deposition removes the native oxide from the c-Si surface. The samples which are passivated by a-Si:H/ $\text{SiN}_x$  double layers are transferred without further treatment from the direct-plasma reactor to the remote-plasma reactor after the a-Si:H deposition.

Table 3.1: *Substrate temperature  $T_{\text{sub}}$ , plasma power  $P_{\text{plasma}}$ , pressure  $p_{\text{plasma}}$ , and  $\text{SiH}_4$  to  $\text{NH}_3$  gas flow ratio  $R$  used for the deposition of a-Si:H and  $\text{SiN}_x$  in this work.*

	$T_{\text{sub}}$ [°C]	$P_{\text{plasma}}$ [W]	$p_{\text{plasma}}$ [Torr]	$R$
a-Si:H	225	100	450	–
$\text{SiN}_x$	230	150	150	0.15

### Optimum deposition temperature

Dauwe found experimentally that the optimum deposition temperature of a-Si:H for surface passivation is  $T_{\text{sub,opt}} = (225 \pm 25)^\circ\text{C}$  in the PECVD system which is used at ISFH [3]. The substrate temperature used for a-Si:H deposition is therefore  $225^\circ\text{C}$  throughout this work.

The major kind of structural defects in the a-Si:H bulk and at the a-Si:H/c-Si interface, are non-saturated electronic orbitals of silicon atoms [17, 59, 60, 1, 61]. These *dangling bonds* form electronic states within the silicon bandgap that act as recombination centers. The saturation of a Si dangling bond by a hydrogen atom or by another silicon atom removes the respective electronic state from the bandgap, and therefore decreases the number of recombination centers.

The amount and the mobility of hydrogen atoms that are incorporated in the passivating a-Si:H layer during the deposition are essential for the passivation of the dangling bond defects, both, in the a-Si:H bulk and at the a-Si:H/c-Si interface. While the hydrogen concentration decreases with increasing deposition temperature, the mobility of the hydrogen atoms increases and makes the passivation of the dangling bonds more effective [60, 61].

In order to achieve the optimum surface passivation, the number of non-passivated defects that contribute to the effective surface recombination rate has to be minimized. At low deposition temperatures  $T_{\text{sub}} < 200^\circ\text{C}$ , the low mobility of the hydrogen and silicon atoms that are adsorbed at the c-Si surface results in a less effective passivation of the dangling bond states, and therefore in a higher defect concentration than at  $200^\circ\text{C} < T_{\text{sub}} < 250^\circ\text{C}$ . At higher temperatures than  $250^\circ\text{C}$ , the decreasing total hydrogen content also leads to a higher defect density at the a-Si:H/c-Si interface than at the optimum deposition temperature [19, 62].

The surface passivation of c-Si solar cells by a-Si:H single layers or by a-Si:H/SiN<sub>x</sub> double layers, is a low-temperature process when compared to the typical deposition temperature of  $400^\circ\text{C}$  for the surface passivation by PECVD-SiN<sub>x</sub> [57], or by thermally grown oxide at around  $1000^\circ\text{C}$ . Therefore, the energy consumption and the risk of impurity diffusion are lower with a-Si:H surface passivation. The SiN<sub>x</sub> films which are deposited at  $230^\circ\text{C}$  in this work do not passivate the c-Si surface, but act only as anti reflective coating and capping layer for the underlying passivation layer of a-Si:H. The refractive index of the SiN<sub>x</sub> is 2.0...2.1 at  $\lambda = 633\text{ nm}$ , when prepared with the settings listed in Table 3.1.

Dauwe has shown that the quality of the surface passivation by thin a-Si:H films on *p*- and *n*-type crystalline silicon, is comparable to the surface passivation that is achieved by dielectric films that are commonly applied to high-efficiency solar cells, i. e. by thermally grown SiO<sub>2</sub>, or by SiN<sub>x</sub> that is deposited at  $400^\circ\text{C}$  [63, 64, 65, 66]. Dauwe found minimum values for the effective SRV with a-Si:H surface passivation of  $S_p = 3\text{ cm/s}$  on *p*-type c-Si with  $p = 1.5 \times 10^{16}\text{ cm}^{-3}$ , and of  $S_n = 7\text{ cm/s}$  on *n*-type c-Si with  $p = 1.5 \times 10^{15}\text{ cm}^{-3}$ , at an excess carrier concentration of  $\Delta n = 10^{15}\text{ cm}^{-3}$  in both cases [19]. The PECVD-deposition of amorphous silicon is therefore the best means for the surface passivation of high-efficiency solar cells, at low temperatures  $T < 300^\circ\text{C}$  [67].

## 3.2 COSIMA contact formation

Dielectric films like  $\text{SiN}_x$ ,  $\text{SiO}_2$  or  $\text{SiC}_x$  that are applied for the surface passivation of solar cells, are electrically insulating or feature only a small conductivity. There are two main approaches to form electric contacts to the emitter and the base of dielectrically coated solar cells: First, the dielectric passivation layers are opened locally, either directly e. g. by lasers, or indirectly by lithographic techniques. Second, screen-printed metalization pastes are fired through the passivation layers at high temperatures, 800–900°C, in order to form local contacts to the underlying emitter or base of the solar cell.

The COSIMA technique replaces dielectric surface passivation with subsequent high-temperature contact firing, by a-Si:H-surface passivation and low-temperature annealing of evaporated aluminum contacts. An overview of the literature on the interaction of Al and Si at low temperatures is given in Section 3.2.1. Section 3.2.2 describes the mechanism of the COSIMA contact formation. In Section 3.2.3, the specific resistances of COSIMA contacts to both, highly-doped and lowly-doped crystalline silicon are shown.

### 3.2.1 Aluminum-induced crystallization of amorphous silicon

The silicon/aluminum alloy is an eutectic system with finite solid-state solubilities of the components. The solubility of Si in the Al phase has its maximum of  $(1.5 \pm 0.1)$  at.% at the eutectic temperature  $T_{\text{eu}} = 577^\circ\text{C}$ , and decreases to about 0.05 at.% at  $T = 300^\circ\text{C}$ . The solubility of Al in the Si phase is much lower, and reaches its maximum of  $(0.016 \pm 0.003)$  at.% at  $1190^\circ\text{C}$  [68]. The solid-state solubility of Si in Al has been exploited for the aluminum-induced crystallization of amorphous silicon in several approaches for the production of solar cells:

- **The layer exchange process** was used by e. g. Nast et al. [69, 70], Gall et al. [71], and Ornaghi et al. [72] to form polycrystalline silicon layers for solar cell production by low-temperature annealing of an aluminum/amorphous silicon dual layer structure. Typically, a glass substrate is covered by an aluminum layer of about 500 nm thickness. An amorphous silicon film of the same thickness is deposited on top of the Al, and the layer structure is annealed for several minutes to hours at  $400 \dots 600^\circ\text{C}$ . During the annealing, the amorphous silicon dissolves in the aluminum layer and forms crystallites once the maximum solubility is reached. If the amorphous Si film and the Al film are of the same thickness, a closed polycrystalline, Al-doped Si film forms in the place of the Al film. The aluminum is displaced and lies on top of the recrystallized silicon layer after the process is completed. Since the annealing temperature is too low for a direct transition from amorphous to

crystalline silicon, the crystallization takes place only in the Al layer that serves as a kind of catalyst for the transition from the amorphous silicon to the crystalline phase that is the system with the lower free energy [70].

- **Counterdoping and crystallization of a-Si:H** was observed by Haque et al. who annealed a dual layer structure of  $n^+$ -doped amorphous silicon films and Al at low temperatures ( $150 \dots 300$ )°C [73, 74]. They showed that an Al-rich mixed  $\text{Al}_x\text{Si}$  phase forms at the Al/a-Si:H interface even at low temperatures  $T = (150 \dots 200)$ °C. Al-doped silicon crystallites form at the a-Si:H/mixed phase interface, and also on top of the Al contacts, which shows that Si atoms diffuse within the aluminum even at low temperatures. The thickness of the a-Si:H layer was ( $130 \dots 300$ ) nm, and the Al contacts were 650 nm thick in their experiments.

The COSIMA technology developed in this work also takes advantage of the solid-state solubility of amorphous silicon in aluminum. In order to form electric contacts to the a-Si:H-passivated base or emitter of a c-Si solar cell, aluminum contacts are deposited onto the passivation layer. Annealing at low temperatures,  $T \geq 200$ °C leads to the dissolution of the a-Si:H into the Al, as described in the references mentioned above. In contrast to the layer-exchange and counter-doping processes, the thickness ratio of a-Si:H to Al is very small: The width of the passivating a-Si:H layer is in the order of 10 nm, and the aluminum contacts are ( $3 \dots 15$ )  $\mu\text{m}$  high. Therefore, the ratio of the number of Si atoms to Al atoms is roughly 1:1000, while it is 1:1 in the layer-exchange process described by Nast.

### 3.2.2 Microstructure of COSIMA contacts

Samples are prepared to monitor the process of COSIMA contact formation: A 50 nm thick a-Si:H films are deposited onto  $p$ -type FZ-Si wafers with a resistivity of  $0.5 \Omega\text{cm}$ . Electron-beam evaporation of aluminum lines through shadow masks forms contact lines on top of the a-Si:H. The line height is  $15 \mu\text{m}$ , and the line width is  $100 \mu\text{m}$ .

The samples are then annealed for 3 h at  $210$ °C, which is still lower than the deposition temperature of the a-Si:H film. The structural properties and the local elemental composition of the a-Si:H/Al layer structure are examined by transmission electron microscopy (TEM), and by energy dispersive x-ray (EDX) analysis before and after the annealing step. While the TEM images mainly show the different electron diffraction contrasts of amorphous and crystalline material, the EDX results show the local concentration of Al and Si atoms.

### Transmission electron microscopy

Figure 3.2 shows cross sectional transmission electron microscopical (TEM) images of the metalized region of two samples, before and after annealing.<sup>1</sup> The micro-

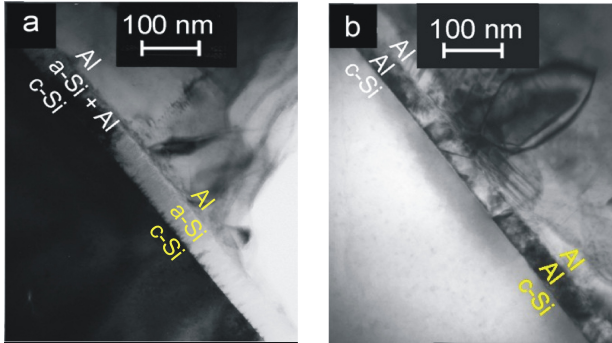


Figure 3.2: *Cross-sectional TEM images of an Al contact finger on an a-Si:H-passivated c-Si wafer. (a) Before annealing, and (b) after annealing at 210°C for 3 h. The elemental composition of the distinct layers is obtained from EDX measurements, and is indicated qualitatively.*

graphs show three distinct regions: A polycrystalline Al layer (the contact line) in the upper right half of the image, a 50 nm thick interlayer (the original a-Si:H film) in the center, and the single crystalline Si substrate in the lower left half of the image. The contrast within the interlayer changes during annealing.

Figure 3.2a shows the c-Si/a-Si:H/Al layer structure before annealing. The image is taken at the rim region of an Al contact line. At the edge of the Al line in the lower right corner of the image, the interlayer consists of amorphous silicon, which is indicated by the bright contrast. Dark contrasts which indicate crystalline material, show within the interlayer region towards the center of the Al contact.

Figure 3.2b shows the c-Si/a-Si:H/Al layer structure after annealing at 210°C for three hours. The 50 nm thick interlayer shows the dark contrast that indicates crystalline material. No change is visible in the Al layer after annealing.

### Energy-dispersive x-ray analysis

Energy dispersive x-ray (EDX) measurements are performed for a quantitative analysis of the local elemental composition of the samples. Figure 3.3 shows the

<sup>1</sup>The TEM microscopy and EDX analysis were performed by M. Nerding and N. Ott at the Central Facility for High Resolution Electron Microscopy of the University of Erlangen.

results of a line scan perpendicular to the layers, before and after annealing. The position of the original a-Si:H layer is determined by TEM imaging, and is indicated by vertical lines.

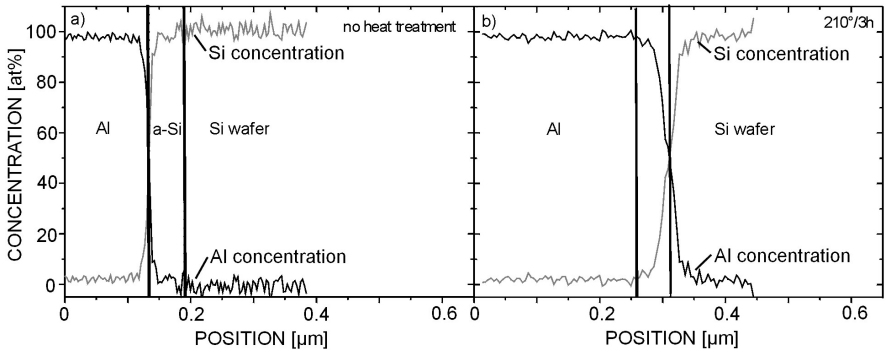


Figure 3.3: EDX elemental analysis obtained from the samples shown in 3.2. (a) Before annealing. The line scan is taken at the edge of the contact line (lower right corner of Figure 3.2a). (b) After annealing at 210°C for 3 h. The position of the interlayer is determined by TEM imaging. The origin of the position-axis is at different depths of the contact in (a) and (b).

Figure 3.3a shows the local Al and Si concentrations of the non-annealed sample, as measured in the lower right half of the area shown in Figure 3.2a (i. e. at the edge of the Al line). There is a sharp transition from the evaporated aluminum with 100% Al concentration, to the a-Si:H layer that shows a silicon content of 100%. The situation is different underneath the center part of the Al line (not shown in Figure 3.3a): The Al concentration at the Al/a-Si:H interface is 50% even without annealing, and decreases towards zero at the a-Si:H/c-Si interface.

The line scans in Figure 3.3b are obtained from the annealed sample shown in Figure 3.2b. The concentration of Al atoms in the former a-Si:H interlayer is 100% after annealing. The amorphous silicon film is thus replaced by an Al layer. An EDX measurement of a different region (not shown in the figure) shows local Si contents as high as 35% up to 1  $\mu\text{m}$  deep in the Al contact, which is attributed to the formation of Si precipitates in the Al layer.

The replacement of a-Si:H by aluminum occurs only in those areas that were originally covered by the Al stripes. No lateral transport of a-Si:H is observed over distances larger than 200 nm from the edge of an Al contact. The non-metalized

regions of the a-Si:H film do not change their structure or elemental composition during annealing at 210°C. The resistance of the Al lines (measured from one end of the line to the other) does not change during the annealing.

## Discussion

The COSIMA contact formation as observed by the TEM and EDX analysis is explained by thermally activated interdiffusion of Al and Si atoms, along the lines of the publications by Nast et al. and Haque et al. [69, 70, 73, 74]:

- The original a-Si:H film dissolves into the overlying Al layer during annealing at 210°C: Haque et al. showed that an Al-rich  $\text{Al}_x\text{Si}$  phase forms at the Al/a-Si:H interface at  $T \geq 150^\circ\text{C}$ . Silicon atoms diffuse from this intermediate phase into the Al layer, where they have a solid-state solubility of  $\leq 0.05\%$  [74].
- Silicon crystallites form within the aluminum, if the Si concentration locally reaches the maximum solubility. Due to the different layer widths, the average concentration of Si in the Al contact is about 0.3% if the a-Si:H layer is completely dissolved. This value is higher than the maximum solubility at the annealing temperature, and therefore Si crystallites must form in any case. These Si precipitates are identified by EDX elemental analysis.
- Haque et al. showed that the higher free energy of the amorphous silicon phase compared to the crystalline phase acts as a driving force for the transport of Si atoms into the Al layer [74]. The minimization of the mean free energy of the layer system therefore leads to the complete dissolution and recrystallization of the a-Si:H within the Al. The average Si content within the Al layer is only about 0.3% after annealing. The silicon precipitates within the Al contact therefore hardly affect its conductivity, which is verified by measurements of the resistance of the Al lines.
- After the contact annealing, the original a-Si:H film is completely replaced by aluminum, as shown in Figure 3.2b. Therefore, the Al layer contacts the c-Si substrate.
- The reaction is restricted to those regions of the sample that are covered by the aluminum stripes. Thus, local contacts to the c-Si substrate form. The non-metalized areas remain passivated by the a-Si:H film.

The high Al concentration of up to 50% even before annealing, which is found within the a-Si:H layer under the center region of the Al lines, is attributed to the radiative heating of the sample during the contact evaporation. The elevated

temperature already causes the  $\text{Al}_x\text{Si}$  phase to form. The sample is partly shielded from heat radiation by the shadow mask at the edges of the contact lines. Therefore, no interdiffusion occurs in the edge regions before annealing, as shown in Figure 3.2a.

### 3.2.3 Contact resistivity

The resistivity of COSIMA contacts to both, the lowly-doped base and the highly doped emitter are shown in this Section, as a function of the annealing temperature. The obtained values are compared to literature data for Al/c-Si contact formation without an a-Si:H interlayer.

The contact resistivities are measured by the transfer length method (TLM) with a variable-gap contact geometry, as sketched in Figure 3.4. Details on the measurement technique and the analysis of the results are shown in References [75, 76]. Contact stripes of width  $b$  and length  $l$ , and varying distance  $d$ , are applied to a substrate, as shown in Figure 3.4a. The total resistance  $R$  between neighboring stripes is then [75]

$$R(d) = \frac{d\rho_{\text{sheet}}}{l} + 2\frac{\rho_c}{lL_T}, \quad (3.1)$$

if the width  $b$  of the stripes is large,  $b \gg L_T$ , when compared to the *transfer length*  $L_T = \sqrt{\rho_c/\rho_{\text{sheet}}}$ . This requirement is fulfilled for the contact layouts that were used in this work.

The total resistance  $R_i$  between each pair of neighboring stripes with distance  $d_i$  is measured in a four-point probe setup, and plotted as a function of the stripe

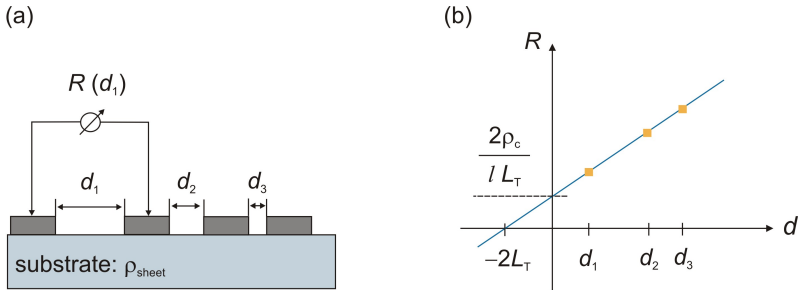


Figure 3.4: (a) Measurement setup for the determination of the contact resistivity by the TLM method. The total resistance  $R$  between neighboring contact stripes of length  $l$  is measured. The stripe distance  $d_i$  varies. (b) Sketched results of a TLM measurement. The contact resistivity is obtained from the linear extrapolation of the resistance  $R$  to  $d = 0$ .



distance, as shown in Figure 3.4b. The extrapolation of a linear fit to the measured values then yields the contact resistivity  $\rho_c = lL_T/2R_0$ , and the transfer length  $L_T = -0.5d_0$ , where the values  $R_0 = R(d = 0)$  and  $d_0 = d(R = 0)$  are the intercepts of the linear fit curve with the respective axes in Figure 3.4.

### COSIMA-contacts to lowly-doped silicon

Two sets of samples are prepared for measuring the resistivity of the COSIMA contacts on *p*-type crystalline silicon wafers with a specific resistance of  $0.5 \Omega\text{cm}$ : The first set of wafers is covered by a 10 nm thick a-Si:H film. Subsequently, aluminum contact stripes are deposited onto the a-Si:H layer by electron-beam evaporation through shadow masks with variable-gap layout. The stripe width is  $b = 490 \mu\text{m}$ , the length  $l = 20 \text{ mm}$ , and the distance varies in the range  $0.1 \text{ mm} < d < 1 \text{ mm}$ .

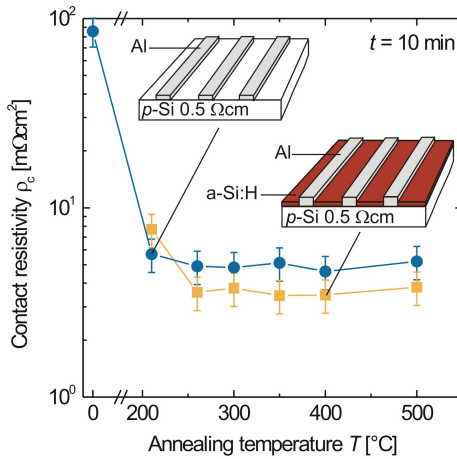


Figure 3.5: Contact resistivity of aluminum COSIMA contacts and of Al contacts that are evaporated directly onto the *c*-Si substrate, after annealing for 10 min at  $210^\circ\text{C} \leq T \leq 500^\circ\text{C}$ . The optimum resistivity of the COSIMA contacts  $\rho_{c,\text{COSIMA}} = (3.5 \pm 0.7) \text{ m}\Omega\text{cm}^2$  is achieved by annealing at  $T \geq 260^\circ\text{C}$ . The lowest contact resistivity without COSIMA is  $\rho_{c,\text{Al}/\text{cSi}} = (5.5 \pm 1.0) \text{ m}\Omega\text{cm}^2$ .

A second set of samples is prepared as reference, by omitting the a-Si:H interlayer and evaporating the Al lines onto the c-Si surface. Native oxide is removed from the c-Si surface by a dip in 2% HF prior to the contact evaporation. The samples are annealed for 10 min each, at various temperatures  $210^{\circ}\text{C} \leq T \leq 500^{\circ}\text{C}$ .

Figure 3.5 shows the contact resistivity of both sets of samples. Before annealing, the COSIMA contacts feature a high resistivity of  $\rho_c > 1\ \Omega\text{cm}^2$  (not shown in the figure for the sake of better resolution). The lowest contact resistivity  $\rho_{c,\text{COSIMA}} = (3.5 \pm 0.7)\ \text{m}\Omega\text{cm}^2$  is achieved by annealing at  $T \geq 260^{\circ}\text{C}$  for 10 min. Annealing at  $210^{\circ}\text{C}$  for 3 h, as it was carried out in Section 3.2.2, leads to the same low contact resistivity.

The contact resistivity of the reference samples without the a-Si:H interlayer is  $\rho_{c,\text{Al/cSi}} = (85 \pm 15)\ \text{m}\Omega\text{cm}^2$ , before annealing, and decreases to its lowest level of  $\rho_{c,\text{Al/cSi}} = (5.5 \pm 1.0)\ \text{m}\Omega\text{cm}^2$  after annealing at  $T \geq 210^{\circ}\text{C}$  for 10 min. Annealing at higher temperatures leads to the same values of  $\rho_c$ , within the uncertainty interval of the measurement.

### COSIMA-contacts to diffused $n^+$ -emitters

Crystalline silicon wafers with a resistivity of  $\rho = 0.5\ \Omega\text{cm}$  are phosphorus-diffused in order to generate an  $n^+$ -emitter with a sheet resistivity of  $90\ \Omega/\square$ . The surface dopant concentration is  $n = 2 \times 10^{19}\ \text{cm}^{-3}$ , and the junction depth is  $0.6\ \mu\text{m}$ . A 10 nm thick a-Si:H film is deposited onto the wafers, and aluminum contact stripes of  $15\ \mu\text{m}$  thickness are evaporated through shadow-masks, in a variable-gap geometry for measuring the contact resistivity. For comparison, phosphorus-diffused wafers without a-Si:H passivation receive contact patterns that consist of a Ti/Pd/Ag triple layer structure, which is typically used at ISFH to form electric contacts to the  $n^+$ -emitter of solar cells. The specific resistance  $\rho_c$  of both kinds of contacts is measured after annealing at  $210^{\circ}\text{C} \leq T \leq 400^{\circ}\text{C}$ .

Figure 3.6 shows the contact resistivity of both sets of samples. The resistivity of the COSIMA contacts is  $(140 \pm 30)\ \text{m}\Omega\text{cm}^2$  before annealing, and decreases by two orders of magnitude to its optimum value of  $\rho_{c,\text{COSIMA}} = (0.75 \pm 0.1)\ \text{m}\Omega\text{cm}^2$  after annealing for 10 min at  $T \geq 260^{\circ}\text{C}$ . This value remains constant for longer annealing times and higher annealing temperatures. The resistivity of the standard Ti/Pd/Ag contacts is  $\rho_{c,\text{TiPdAg}} = (0.9 \pm 0.3)\ \text{m}\Omega\text{cm}^2$  on the emitter samples that are prepared without a-Si:H interlayer, after annealing at  $400^{\circ}\text{C}$  for 10 min. Therefore, the COSIMA contacting scheme results in the same contact resistivity as the standard method applied at the ISFH, within the uncertainty interval of the measurement.

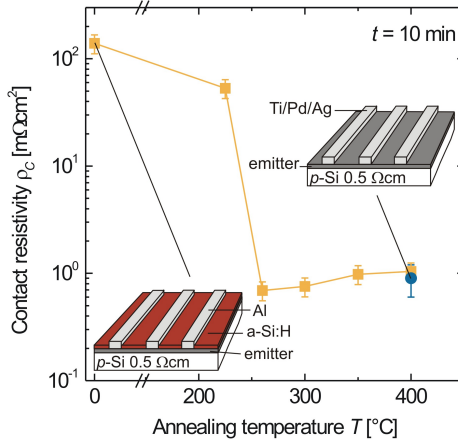


Figure 3.6: Resistivity of aluminum COSIMA contacts and of Ti/Pd/Ag contacts that are evaporated directly onto the  $90\ \Omega/\square$   $n^+$ -emitter, after annealing for 10 min at  $210^\circ\text{C} \leq T \leq 400^\circ\text{C}$ . The minimum resistivity of the COSIMA contacts  $\rho_{c,\text{COSIMA}} = (0.75 \pm 0.1)\ \text{m}\Omega\text{cm}^2$  is achieved by annealing at  $T \geq 260^\circ\text{C}$ . The minimum contact resistivity of the Ti/Pd/Ag contacts is  $\rho_{c,\text{TiPdAg}} = (0.9 \pm 0.3)\ \text{m}\Omega\text{cm}^2$  after annealing at  $400^\circ\text{C}$ .

### 3.2.4 Discussion

The COSIMA technique allows for the formation of contacts to both, the  $p$ -type base and the  $n^+$ -type emitter of crystalline silicon solar cells. The technique maintains the high quality of the a-Si:H-passivation of the non-metallized surface areas, and allows for the formation of contacts to the a-Si:H-passivated base and emitter of solar cells, by a annealing at low temperatures  $T < 300^\circ\text{C}$ .

The high values of  $\rho_c > 1\ \Omega\text{cm}^2$  of the COSIMA contacts before annealing are due to the low conductivity of the non-doped a-Si:H layer below the Al stripes. During annealing, the a-Si:H film dissolves in the overlying Al layer as shown in Section 3.2.2, and a contact to the crystalline silicon forms. The minimum contact resistivity of both, COSIMA-contacted samples and reference samples without a-Si:H, is achieved after annealing at  $260^\circ\text{C}$  for 10 min. COSIMA contacts to both, the emitter and the base, exhibit resistivities that are of the same order, or even

lower, as those of the reference processes shown in Sections 3.2 and 3.2.

### Comparison to literature data

The minimum resistivity of the COSIMA contacts are achieved after annealing for 10 min at  $T \geq 260^\circ\text{C}$ . The values obtained in the experiments are  $\rho_{c,\text{base}} = (3.5 \pm 0.5) \text{ m}\Omega\text{cm}^2$  for COSIMA contacts to  $0.5 \Omega\text{cm}$   $p$ -type  $c$ -Si, and  $\rho_{c,\text{emi}} = (0.75 \pm 0.05) \text{ m}\Omega\text{cm}^2$  for COSIMA contacts to the  $90 \Omega/\square$   $n^+$ -emitter.

Aluminum forms a Schottky-type contact to crystalline silicon, with a barrier height of  $(0.4 \dots 0.6) \text{ eV}$ . The resulting contact resistivity to the lowly-doped  $p$ -type ( $0.5 \Omega\text{cm}$ ) base would therefore be in the order of  $100 \text{ m}\Omega\text{cm}^2$  [77]. However, measured values to be found in the literature are in the range of  $\rho_{c,\text{base}} = (0.1 \dots 1) \text{ m}\Omega\text{cm}^2$ . The large discrepancy of predicted and measured values is attributed in the literature to the formation of Al spikes, i. e. the local formation of Al-doped regions at the Al/ $c$ -Si interface that penetrate into the base material during annealing of the contacts, and thus decrease the contact resistance [77, 78]. This effect is stronger at higher annealing temperatures. The minimum resistivities of both, the COSIMA and the reference-type base-contacts shown in Section 3.2 are thus comparable to literature values of evaporated Al/ $c$ -Si contacts that show little or no spiking.

The situation is clearer for the COSIMA contacts to the  $n^+$ -type emitter, that features a surface dopant concentration of  $N_{\text{D}} = 2 \times 10^{19} \text{ cm}^{-3}$ . Both, the results of the Schottky theory, and measured values reported in the literature lie within the range of  $\rho_{c,\text{emi}} = (0.1 \dots 1) \text{ m}\Omega\text{cm}^2$  for this dopant concentration [77, 34]. Thus, the minimum contact resistivities obtained for both, the COSIMA and the Ti/Pd/Ag contacting schemes in Section 3.2 agree with the values of evaporated Al/ $c$ -Si contacts to be found in the literature.

### 3.3 Saturation current of the COSIMA-processed base

The base saturation current density of COSIMA-processed solar cells that feature an  $a$ -Si:H-passivated base with local aluminum contacts, is controlled by the local surface recombination velocities  $S_{\text{met}}$  below the contacts, and  $S_{\text{pass}}$  in the  $a$ -Si:H-passivated areas, and by the contact layout as shown in Section 2.6. In order to experimentally verify the model derived in Section 2.6, the saturation current density of the COSIMA-processed base is deduced from measurements of the effective surface recombination velocity of  $c$ -Si wafers that feature the same  $a$ -Si:H surface passivation and contact layout, as would be applied to the base of a solar cell.

Samples are prepared by depositing 50 nm-thick films of amorphous silicon onto both sides of (100)-oriented,  $p$ -type FZ-Si wafers with doping concentration  $p = 1 \times 10^{16} \text{ cm}^{-3}$  and thickness  $W = 300 \mu\text{m}$ . Subsequently, aluminum is deposited in various stripe- and dot-patterns onto one side of the samples through shadow masks, by electron-beam evaporation. The samples are annealed at  $210^\circ\text{C}$  for 3 h to form local COSIMA contacts. Contact coverages of  $f = (0 \dots 100) \%$  of the total surface area are realized, with contact spacings in the range  $p = (1 \dots 5) \text{ mm}$ .

The spatially resolved effective carrier lifetime  $\tau_{\text{eff}}$  is obtained from microwave-detected photoconductance decay (MWPCD) measurements. The illumination and microwave radiation are directed at the non-metalized side of the samples. The spatial resolution is  $250 \mu\text{m}$ . Bias light from a halogen lamp with an above-bandgap photon flux of  $2 \times 10^{21} \text{ m}^{-2}\text{s}^{-1}$  (equivalent to 1 sun) illuminates the sample during the measurement. The base saturation current is calculated by Equation 2.28 from the effective recombination velocity of the locally contacted side of the sample.

### 3.3.1 Experimental determination of the saturation current

Figure 3.7 shows the effective carrier lifetime map of an a-Si:H passivated sample with dot contacts in a square pattern. Bright areas indicate a high effective carrier lifetime. The front surface of the wafer is passivated by a-Si:H, and thus shows a spatially homogeneous surface recombination velocity,  $S_f = S_{\text{pass}}$ . The rear surface is divided into six sections, in which the contact coverage  $f$  is varied from 2% to 38%. The period length is  $p = 1.5 \text{ mm}$ . Thus, the effective surface recombination velocity at the rear side is a function of the contact layout as shown in Section 2.6,  $S_r = S_{\text{eff}}(f, p)$ . The center of the wafer is divided into two semicircles with  $f = 0$  and  $f = 100\%$ , and therefore  $S_r = S_{\text{pass}}$  and  $S_r = S_{\text{met}}$ , respectively.

The effective carrier lifetime  $\tau_{\text{pass}}$  of the center part with  $f = 0$  is only determined by the SRV  $S_{\text{pass}}$ , which is calculated analogously to Equation 2.23 in *lli* conditions, by solving

$$\tan(\beta_0 W) = \frac{2S_{\text{pass}}D\beta_0}{D^2\beta_0^2 - S_{\text{pass}}^2} \quad \text{with} \quad \beta_0 = D^{-1}\sqrt{\tau_{\text{pass}}^{-1} - \tau_b^{-1}} \quad (3.2)$$

for  $S_{\text{pass}}$ . The bulk carrier lifetime of the high-quality FZ-Si wafers is approximated by the Auger-limited lifetime,  $\tau_b = \tau_{\text{Auger}}$  that is calculated from the parameterization by Kerr and Cuevas given by Equation 2.11. The value of  $S_{\text{pass}}$  that is determined from the MWPCD measurement, is therefore the upper limit of the recombination velocity at the a-Si:H passivated surface.

In order to determine the effective recombination velocity of the locally COSIMA-contacted sections of the samples,  $S_{\text{eff}}(f, p)$  as a function of the contact coverage and spacing, the harmonic mean of the spatially resolved local effective carrier

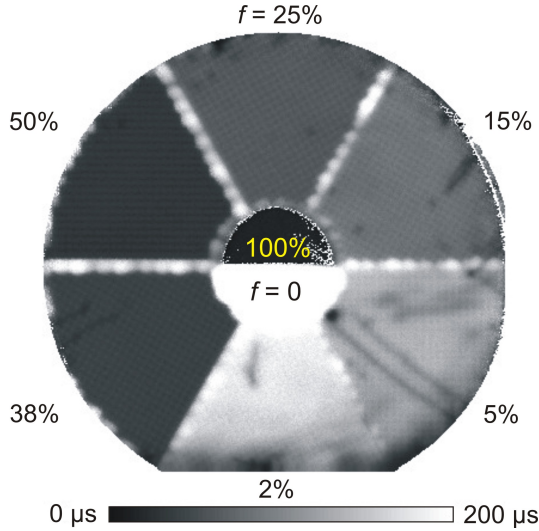


Figure 3.7: Map of the effective carrier lifetime  $\tau_{\text{eff}}$  of an a-Si:H passivated sample with dot contacts in a square pattern. The surface is divided into six sections with varying contact coverage. The period length is  $p = 1.5$  mm.

lifetime  $\tau_{\text{eff}}(x, y)$ ,

$$\langle \tau_{\text{eff}}^{-1}(f, p) \rangle^{-1} = \left[ \frac{1}{\text{Area}} \int_{\text{Area}} \tau_{\text{eff}}^{-1}(x, y) dA \right]^{-1} \quad (3.3)$$

is calculated within each segment of the sample with contact coverage  $f$  and contact spacing  $p$ . The harmonic mean is the relevant value that determines the global saturation current of a solar cell with spatially inhomogeneous recombination characteristics [79]. The value of  $\langle \tau_{\text{eff}}^{-1}(f, p) \rangle$  is determined from a  $1 \text{ cm}^2$ -large area of the respective sample segment which is selected to exclude process-induced inhomogeneities such as the lines that appear in the  $f = 5\%$  section shown in Figure 3.7.

The effective surface recombination velocity is then obtained by solving

$$\tan(\beta_0 W) = \frac{[S_{\text{pass}} + S_{\text{eff}}(f, p)] D \beta_0}{D^2 \beta_0^2 - S_{\text{pass}} S_{\text{eff}}(f, p)} \quad \text{with} \quad \beta_0 = D^{-1} \sqrt{\langle \tau_{\text{eff}}^{-1}(f, p) \rangle - \tau_b^{-1}}. \quad (3.4)$$

for  $S_{\text{eff}}(f, p)$  [30, 31, 32]. The base saturation current density is calculated from Equation 2.28,

$$J_{0b}(f, p) = \frac{qDn_i^2}{L_{\text{eff}}N_{\text{dop}}} \quad \text{with} \quad L_{\text{eff}} = L_b \frac{1 + S_{\text{eff}}(f, p) L_b/D \tanh(W/L_b)}{S_{\text{eff}}(f, p) L_b/D + \tanh(W/L_b)}, \quad (3.5)$$

where the bulk diffusion length is assumed to be limited by Auger recombination,  $L_b = \sqrt{D\tau_{\text{Auger}}}$ .

### 3.3.2 Comparison to theory

The experimentally deduced base saturation current densities  $J_{0b}(f, p)$  are compared to the results of the theory that is developed in Section 2.6. The model is checked particularly in the ranges of contact coverage  $f < 10\%$  and period length  $p \geq W$  that are in between the small-scale range and the large-scale range, as shown in Section 2.6.5.

#### Dot-contact layout

Figure 3.8a shows the base saturation current density  $J_{0b}$  of COSIMA-processed samples with local dot-shaped contacts, as a function of the contact coverage  $f = 0 \dots 100\%$ . The symbols denote base saturation current densities that are obtained from MWPCD measurements, as described above.

The saturation current density increases from  $J_{0b, \text{pass}} = (36 \pm 9) \text{ fA/cm}^2$  for  $f = 0$ , to  $J_{0b, \text{met}} = (1.74 \pm 0.01) \times 10^3 \text{ fA/cm}^2$  for  $f = 100\%$ . The corresponding effective surface recombination velocities are  $S_{\text{pass}} = (20 \pm 5) \text{ cm/s}$  and  $S_{\text{met}} = (10^5 \dots 10^7) \text{ cm/s}$ , respectively. The value  $S_{\text{pass}} = (20 \pm 5) \text{ cm/s}$  is within the range that has been reported for surface passivation by silicon nitride layers [64, 65, 66], while the value  $S_{\text{met}} = (10^5 \dots 10^7) \text{ cm/s}$  is in the range of values that is reported in literature for the effective SRV below the base contacts of  $p$ -type solar cells [80, 81].

Figure 3.8b shows the base saturation current density  $J_{0b}$  as a function of the period length  $p$ , for contact coverages  $f = 1.3\%$ ,  $3.0\%$  and  $10\%$ . Typical ranges of the contact coverage and period length are  $f \leq 5\%$  and  $p \geq W$  for high-efficiency PERC solar cells [45, 47]. The saturation current density shows a strong decrease with increasing period length for  $p \leq 2 \text{ mm}$ , and asymptotically approaches the large scale limit given by Equation 2.69 for  $p \gg W$ .

The local surface recombination velocities  $S_{\text{pass}} = 20 \text{ cm/s}$  of the a-Si:H passivated areas, and  $S_{\text{met}} = 1 \times 10^6 \text{ cm/s}$  below the contacts, are used to calculate the base saturation current density from the model shown in Section 2.6, by solving Equation 2.65. Since the effective SRVs  $S_{\text{met}}$  and  $S_{\text{pass}}$  are obtained from the measurement, and the contact spacing  $p$  and contact coverage  $f$  are determined by

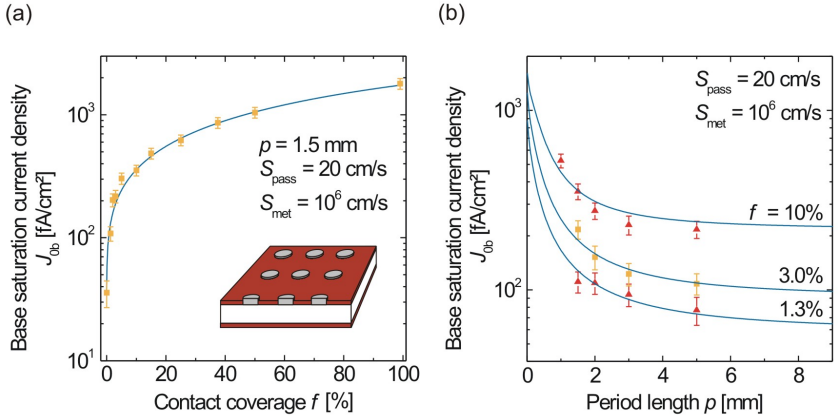


Figure 3.8: Base saturation current density  $J_{0b}$  of COSIMA-processed samples with local dot-shaped contacts, (a) as a function of the contact coverage  $f$  and (b) as a function of the period length  $p$ . The surface is passivated by 50 nm of a-Si:H. Values that are obtained from MWPCD measurements are shown as symbols. The blue lines show the base saturation current density that is obtained from Equation 2.65. The theory fits the experimentally obtained base saturation current densities within the uncertainty intervals of the measurement.

the layout of the samples, Equation 2.65 contains no free fit parameters. The base saturation current densities that are obtained from the model, are shown as blue lines in Figure 3.8. The theory fits the experimentally obtained values of  $J_{0b}(f, p)$  for  $f = 0 \dots 100\%$  and  $p = (1 \dots 5) \text{ mm}$ , within the uncertainty interval of the measurement. The validity of the model is therefore demonstrated within a range of the period length  $p$  and the contact coverage  $f$  that is typical for high-efficiency PERC solar cells.

### Stripe-contact layout

Figure 3.9 shows the base saturation current density  $J_{0b}$  of COSIMA-processed samples with local stripe-shaped contacts, as a function of the contact coverage  $f = 0 \dots 50\%$  for two different stripe widths,  $a = 20 \mu\text{m}$  and  $a = 300 \mu\text{m}$ . Again, the symbols denote base saturation current densities that are obtained from MWPCD measurements, and the lines are calculated from the model shown in Section 2.6.



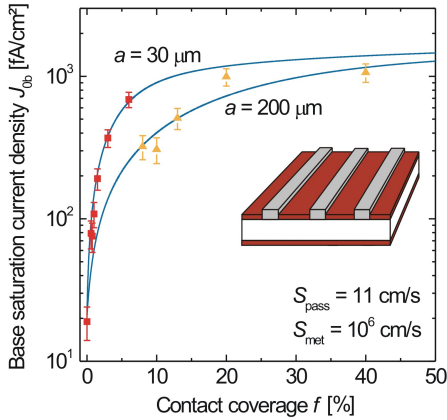


Figure 3.9: Base saturation current density  $J_{0b}$  of COSIMA-processed samples with local stripe-shaped contacts, as a function of the contact coverage  $f$ . The width of the contact stripes is  $a = 20 \mu\text{m}$  and  $a = 300 \mu\text{m}$ , respectively. The theory fits the experimentally obtained base saturation current densities within the uncertainty intervals of the measurement.

The recombination velocity of the surface areas that are passivated by a-Si:H, is  $S_{\text{pass}} = (11 \pm 2) \text{ cm/s}$ , which is obtained from a non-metalized sample (i. e.  $f = 0$ ), as described above. The corresponding base saturation current density is  $J_{0b,\text{pass}} = (19 \pm 5) \text{ fA/cm}^2$ . The surface recombination velocity below the contact stripes is  $S_{\text{met}} = (10^5 \dots 10^7) \text{ cm/s}$  and therefore  $J_{0b,\text{met}} = (1.74 \pm 0.01) \times 10^3 \text{ fA/cm}^2$  (not shown in the Figure). The theory fits the experimentally obtained values of  $J_{0b}(f, p)$  within the uncertainty interval of the measurement, just like for the dot-contacted samples.

The base saturation current with  $J_{0b} = (190 \pm 30) \text{ fA/cm}^2$  with a contact coverage of 1.5%. These values comply with literature data published for PERC solar cells with an efficiency exceeding 20% [78].

The dot- and stripe-contacted samples exhibit different SRVs  $S_{\text{pass}}$ , because they were passivated in different a-Si:H deposition runs. The local recombination velocity below the contacts  $S_{\text{met}}$ , is the same in both cases, because the a-Si:H film below the contacts dissolves during the COSIMA contact formation process. The value of  $S_{\text{met}}$  is therefore independent of the quality of the surface passivation by

the amorphous silicon film.

### 3.4 Summary

Intrinsic amorphous silicon was shown by Dauwe to excellently passivate the surface of crystalline silicon. However, the application of a-Si:H passivation to solar cells requires also the formation of electric contacts to the passivated surfaces of emitter and base. The low electric conductivity of the non-doped a-Si:H passivation layer makes it necessary that contacts are formed to the crystalline emitter or base, and not to the a-Si:H film. The COSIMA technique combines the surface passivation by an a-Si:H film, with the application of local aluminum contacts which are annealed at low temperatures  $T \leq 300^\circ\text{C}$ .

The a-Si:H film below the local Al contacts dissolves completely during annealing in the aluminum, where silicon crystallites form when the Si concentration exceeds the solubility limit. The resistivities of COSIMA contacts to the lowly-doped base and the highly-doped emitter are the same, or even lower than values that are obtained for reference samples that were processed without the a-Si:H interlayer,  $\rho_{c,\text{base}} = (3.5 \pm 0.5) \text{ m}\Omega\text{cm}^2$  for COSIMA contacts to  $0.5 \Omega\text{cm}$   $p$ -type  $c$ -Si, and  $\rho_{c,\text{emi}} = (0.75 \pm 0.05) \text{ m}\Omega\text{cm}^2$  for COSIMA contacts to a  $90 \Omega/\square$ ,  $n^+$ -type emitter. The minimum annealing temperature for the COSIMA contact formation is  $250^\circ\text{C}$  when annealing for 10 min. The interaction of Al and Si is restricted to those areas of the a-Si:H layer that are covered with Al. No lateral diffusion of Si atoms occurs within the amorphous silicon film, so the passivation of the non-metalized fraction of the solar cell surface is not affected by the contact-annealing step.

The base saturation current density  $J_{0b}$  of the COSIMA-processed, locally contacted base is measured for technologically relevant contact spacings  $1 \text{ mm} \leq p \leq 5 \text{ mm}$ , and contact coverages  $0 \leq f \leq 1$ . The experimentally deduced base saturation currents fit the the model shown in Section 2.6, within the uncertainty interval of the measurement. The effective recombination velocity at the interface of  $p$ -type  $c$ -Si ( $p = 10^{16} \text{ cm}^{-3}$ ), and annealed Al contacts is determined from MWPCD measurements. The obtained value  $S_{\text{met}} \approx 10^6 \text{ cm/s}$  allows for an excellent fit of the measured saturation current densities  $J_{0b}(f, p)$  by the model. Comparison with literature data on PERC solar cells shows that the base saturation current densities obtained with the COSIMA technique, comply with energy conversion efficiencies that exceed 20%.

## 4 Surface passivation by a-Si:H single- and a-Si:H/SiN<sub>x</sub> double-layers

Section 4.1 shows the optimization of the a-Si:H layer thickness for optimum surface passivation. Amorphous silicon absorbs light in the visible-wavelength range  $\lambda < 600$  nm. It is therefore necessary to keep the a-Si:H film as thin as possible while maintaining optimum surface passivation, when the a-Si:H layer is placed in the light path of solar cells (i. e. on the front side, or also on the rear side of bifacial solar cells).

In order to apply a-Si:H to the emitter side of solar cells, the suitability of amorphous silicon for the passivation of highly-doped c-Si surfaces has to be ensured. Section 4.2 shows the passivation of boron-diffused emitters and of phosphorus-diffused emitters by a-Si:H/SiN<sub>x</sub> double layers. The stability of the emitter passivation under UV irradiation is determined.

High-efficiency solar cells feature textured surfaces to enhance the optical confinement and therefore increase the short-circuit current when compared to a planar solar cell. However, the increased effective surface area and the different surface orientation make it necessary to prove the suitability of amorphous silicon for the passivation of textured silicon surfaces, which is shown in Section 4.3.

### 4.1 Optimum thickness of the a-Si:H film

Amorphous silicon absorbs light in the small-wavelength range  $\lambda < 600$  nm. It is therefore necessary for the fabrication of solar cells to keep the a-Si:H film as thin as possible while maintaining optimum surface passivation, when the a-Si:H film is placed within the light path, i. e. either on the front side, or on the rear side of bifacial solar cells. Furthermore, keeping the a-Si:H layer thin allows for short deposition times during the solar cell production process.

In order to analyze the impact of the a-Si:H layer thickness  $d$  on the surface passivation of the lowly-doped base of solar cells, a-Si:H films with  $3.5 \text{ nm} \leq d \leq 15 \text{ nm}$  are deposited as shown in Section 3.1, onto both sides of polished  $p$ -type, (100)-oriented FZ-Si wafers. The resistivity of the wafers is  $\rho = (1.5 \pm 0.3) \text{ } \Omega\text{cm}$ ,

and their thickness  $W = 380 \mu\text{m}$ . Layers with  $d > 15 \text{ nm}$  form blisters during the deposition or subsequent annealing, due to the formation of molecular hydrogen inside the a-Si:H film. A second set of samples is passivated by a-Si:H/SiN<sub>x</sub> double layers. The 60 nm thick anti reflective SiN<sub>x</sub> film is deposited on top of the a-Si:H layer by remote-PECVD at 230°C, as described in Section 3.1. The SiN<sub>x</sub> does not passivate the c-Si surface, but acts only as anti reflective coating and capping layer for the underlying a-Si:H- passivation layer.

The effective carrier lifetime  $\tau_{\text{eff}}$  of the samples is extracted from QSSPC measurements. The effective surface recombination velocity (SRV)  $S_{\text{eff}}$  is then calculated from  $\tau_{\text{eff}}$  by the Equations 2.20 and 2.22, as a measure for the quality of the a-Si:H passivation. The simplified evaluation with  $\chi = 1$  provides accurate results because the SRV is small,  $S_{\text{eff}} \ll W/D_a$ . The bulk carrier lifetime of the wafers is approximated by the parameterization of the intrinsic Auger- and radiative recombination lifetime by Kerr and Cuevas, after Equation 2.11. Therefore, all defect-related carrier recombination is attributed to the recombination at the surface, which makes  $S_{\text{eff}}$  the upper limit of the actual surface recombination velocity.

In this work, an infrared filter transmitting only wavelengths  $\lambda > 700 \text{ nm}$  is used for the QSSPC measurements, in order to prevent the generation of carriers within the a-Si:H passivation layer. Amorphous silicon is mostly transparent for wavelengths that correspond to photon energies that are smaller than the optical bandgap, which is around  $E_{g,\text{a-Si:H}} \approx 1.7 \text{ eV}$  ( $\lambda_{g,\text{a-Si:H}} \approx 730 \text{ nm}$ ) for PECVD-deposited a-Si:H [27, 28, 29]. Therefore, excess carriers are only generated in the c-Si bulk. Recombination in the amorphous silicon layer is then restricted to carriers that tunnel or diffuse from the c-Si bulk into the a-Si:H bulk.

#### 4.1.1 A-Si:H single layer passivation

Figure 4.1a shows the injection-dependent effective carrier lifetime  $\tau_{\text{eff}}$  that is obtained from QSSPC measurements of the a-Si:H single layer-passivated samples. The samples are measured in the as-deposited state, immediately after the a-Si:H deposition. Figure 4.1b shows  $S_{\text{eff}}$  at the excess carrier density  $\Delta n = 10^{14} \text{ cm}^{-3}$  and at  $\Delta n = 10^{15} \text{ cm}^{-3}$ , as a function of the thickness  $d$  of the a-Si:H film. Typical solar cells show  $\Delta n \approx 10^{14} \text{ cm}^{-3}$  at the maximum power point, and  $\Delta n \approx 10^{15} \text{ cm}^{-3}$  in open circuit under 1 sun illumination conditions [25].

The samples with  $d \leq 5 \text{ nm}$  and those with  $d \geq 6.5 \text{ nm}$  form two groups with the same injection-dependence of the effective carrier lifetime. The surface recombination velocity decreases by a factor of 2–3 from  $d = 5 \text{ nm}$  to  $d = 6.5 \text{ nm}$ . The optimum surface passivation is achieved with  $d \geq 6.5 \text{ nm}$ , with the optimum SRV being  $S_{\text{eff}} = (3.5 \pm 0.6) \text{ cm/s}$  at  $\Delta n = 10^{15} \text{ cm}^{-3}$ , and  $S_{\text{eff}} = (8.5 \pm 0.8) \text{ cm/s}$  at  $\Delta n = 10^{14} \text{ cm}^{-3}$ .

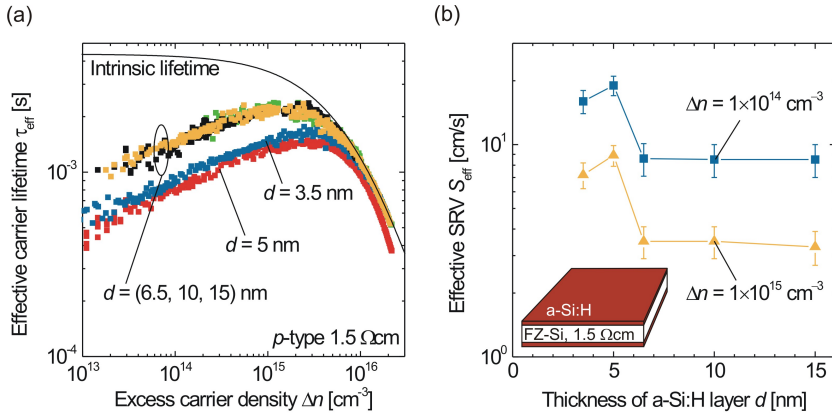


Figure 4.1: (a) Effective carrier lifetime of 1.5  $\Omega\text{cm}$  p-type c-Si wafers passivated with a-Si:H single layers of the thickness  $d$ . The wafer thickness is 380  $\mu\text{m}$ . Samples with  $d \leq 5$  nm and  $d \geq 6.5$  nm form two groups with an almost equal injection-dependence of the effective carrier lifetime. (b) Effective surface recombination velocity  $S_{\text{eff}}$  of the same samples at  $\Delta n = 10^{14} \text{ cm}^{-3}$  and at  $\Delta n = 10^{15} \text{ cm}^{-3}$ . The surface recombination velocity decreases from  $d = 5$  nm to  $d = 6.5$  nm. The optimum SRV is  $S_{\text{eff}} = (3.5 \pm 0.6) \text{ cm/s}$  at  $\Delta n = 10^{15} \text{ cm}^{-3}$ , with  $d \geq 6.5$  nm.

### 4.1.2 A-Si:H/SiN<sub>x</sub> double layer passivation

Figure 4.2 shows the effective SRV  $S_{\text{eff}}$  of the a-Si:H/SiN<sub>x</sub> double layer-passivated wafers, as a function of the a-Si:H thickness  $d$ , at  $\Delta n = 10^{15} \text{ cm}^{-3}$ . The results of the a-Si:H single layer-passivated wafers shown in Figure 4.1 are included for comparison. Both, single-layer samples and double-layer samples are optimally passivated with  $d \geq 6.5$  nm. All measured data for  $d \geq 6.5$  nm lie within  $S_{\text{eff}} = (3.5 \pm 1.0) \text{ cm/s}$ .

Both kinds of samples show the same decrease of  $S_{\text{eff}}$  from  $d \leq 5$  nm to  $d \geq 6.5$  nm. The SRV of the double layer-passivated samples seems to decrease from  $d = 6.5$  nm to  $d = 15$  nm. However, all values are within the tolerance of the measurement.

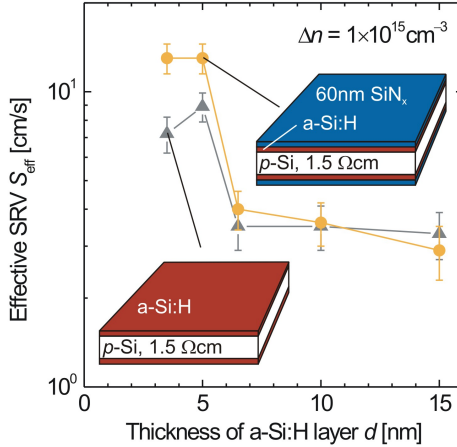


Figure 4.2: Effective SRV  $S_{\text{eff}}$  of a-Si:H/SiN<sub>x</sub> double layer-passivated samples at  $\Delta n = 10^{15} \text{ cm}^{-3}$ , as a function of the a-Si:H layer width  $d$ . The circles denote  $\tau_{\text{eff}}$  and  $S_{\text{eff}}$  of the a-Si:H/SiN<sub>x</sub>-passivated samples. The gray triangular symbols stand for the a-Si:H-passivated samples.

### 4.1.3 Discussion

The minimum a-Si:H thickness is  $d = 6.5 \text{ nm}$  to achieve the optimum passivation of the planar c-Si surface by amorphous silicon. The results of Section 4.1.2 show that the deposition of the SiN<sub>x</sub> capping layer at 230°C has no influence on the passivation quality of the underlying a-Si:H layer. The effective surface recombination velocity of  $S_{\text{eff}} = (3.5 \pm 1.0) \text{ cm/s}$  at  $\Delta n = 10^{15} \text{ cm}^{-3}$  is among the lowest ones reported for the surface passivation of crystalline silicon by thermally grown oxide, or by SiN<sub>x</sub> [63, 64, 65, 66]. The corresponding base saturation current is  $J_{0,b} = (6.1 \pm 1.8) \text{ fA/cm}^2$ .

The reason for the improvement of the surface passivation from  $d \leq 5 \text{ nm}$  to  $d \geq 6.5 \text{ nm}$  is not clear from these measurements. However, it is proposed in this work that too thin a-Si:H layers are not completely closed. Non-passivated pinholes remain, which increase the effective surface recombination velocity.

As the effective carrier lifetime obtained from the QSSPC measurements is an average value of about  $2.5 \text{ cm}^2$  surface area of the sample, pinholes in the passivat-

ing a-Si:H layer are perceived as an increased area-averaged surface recombination velocity.

A second possibility is that the passivation of dangling bonds of the c-Si surface atoms might be less effective with  $d \leq 5$  nm due to the shorter heating time during the deposition. However, this possibility was ruled out in this work, by additional experiments: Depositions with longer remaining times up to 1 min on the sample stage after the a-Si:H deposition, and post-deposition annealing of the samples at temperatures up to 300°C are performed. In both cases, the measured effective lifetimes are equal to those of Figure 4.1, within the uncertainty intervals of the measurement.

## 4.2 Passivation of diffused emitters

Highly efficient silicon solar cells feature an excellent surface passivation of both, the emitter and the base. Today, low-temperature processing sequences are based in most cases on the passivation of the phosphorus-diffused emitter of *p*-type cells by silicon nitride, which is also used as anti reflective coating [82, 67]. However, the passivation of boron-diffused emitters for *n*-type cells has only recently been achieved by the use of SiN<sub>x</sub> layers with a high refractive index, and by including an additional annealing step of 30 min at 450°C for optimum passivation [83]. The deposition of silicon nitride with a lower refractive index, which is suitable as anti reflective coating, was shown to have no passivating effect on boron-diffused emitters, and thermally grown oxide is therefore still the standard passivation technique for boron-diffused emitters on *n*-type solar cells [2, 84].

The passivation of both, phosphorus-diffused emitters and boron-diffused emitters by a-Si:H/SiN<sub>x</sub> double layers, is described in the sections 4.2.2 and 4.2.3. The solar cells that are prepared in this work feature the emitter on the illuminated front side, and therefore the anti reflective SiN<sub>x</sub> capping layer is mandatory to achieve high efficiencies. The a-Si:H thickness and the post-deposition anneal are optimized for both types of emitters. The dopant profiles of the diffused emitters are shown in Section 4.2.1.

The stability of the a-Si:H/SiN<sub>x</sub> passivation under ultraviolet (UV) irradiation is most important for the application to the front side of solar cells. The quality of the surface passivation is therefore shown as a function of the duration of the UV irradiation, in Section 4.2.4.

### 4.2.1 Sample preparation

Two different boron-diffusions on (100)-oriented 10 Ωcm *n*-type FZ-Si wafers generate *p*<sup>+</sup>-type emitters on both sides of the samples, with a sheet resistance of 75 Ω/□ or 225 Ω/□, respectively. A 90 Ω/□ *n*<sup>+</sup>-type emitter is generated by a phosphorus-diffusion of (100)-oriented 200 Ωcm *p*-type FZ-Si wafers. The sheet resistances are measured by the four-point probe technique, with an accuracy of about 10%. The emitter lifetime samples are then passivated by depositing the a-Si:H layer with thickness *d*, which is capped by the 60 nm thick SiN<sub>x</sub> layer, as described in Section 3.1.

For comparison, samples with just a SiN<sub>x</sub>-passivation are prepared: The surface of the phosphorus-diffused emitter is passivated by a 20 nm thick layer of SiN<sub>x</sub> with a refractive index *n* = 2.4, which is capped by a 60 nm thick layer of SiN<sub>x</sub> with *n* = 2.05. The deposition temperature for both layers is 400°C, which allows for a high-quality surface passivation of *n*<sup>+</sup>-emitters [64].

The emitter saturation current *J*<sub>0e</sub> as a measure for the quality of the surface passivation, is determined from QSSPC measurements by the Kane-Swanson method as shown in Section 2.5.1. The base is in *hli* and the emitter is in *lli*-conditions.

Figure 4.3a shows the doping profiles of the two boron-diffused emitters that are investigated in this section. The doping profiles are measured by the ECV technique [85]. The surface dopant concentrations are  $N_{\text{surf},p+} = (1.3 \pm 0.3) \times 10^{20} \text{ cm}^{-3}$  and  $(3 \pm 0.6) \times 10^{19} \text{ cm}^{-3}$ . The depth of the *pn*-junction is  $z_{\text{jct},p+} = (0.42 \pm 0.03) \mu\text{m}$  and  $(0.28 \pm 0.03) \mu\text{m}$ , respectively.

Figure 4.3b shows the doping profile of the phosphorus-diffused emitter. The sheet resistance is  $\rho_{\text{sheet}} = 90 \Omega/\square$ . The surface dopant concentration is  $N_{\text{surf},n+} = (2 \pm 0.4) \times 10^{19} \text{ cm}^{-3}$ . The depth of the *pn*-junction is  $z_{\text{jct},n+} = (0.63 \pm 0.04) \mu\text{m}$ .

### Transparency of the diffused emitters

An estimate of the transparency of the emitters shown in Figure 4.3 is made by calculating the Auger-limited bulk diffusion length  $L_{\text{Auger}} = \sqrt{D_{\text{a}}\tau_{\text{Auger}}}$  of their surface-near region, along the lines of Section 2.5.2: Neglecting high-doping effects, Equation 2.11 shows that a boron concentration of  $1 \times 10^{20} \text{ cm}^{-3}$  like in the 75 Ω/□ *p*<sup>+</sup>-emitter of Figure 4.3a corresponds to the Auger-limited *lli* carrier lifetime of 1.7 ns. This corresponds to a carrier diffusion length of about 0.4 μm, which is equal to the junction depth. In the same way,  $L_{\text{Auger}} \approx 1 \mu\text{m}$  is found for both, the 225 Ω/□ boron-diffused emitter, and the 90 Ω/□ phosphorus-diffused emitter. However, these values are lower limits because the dopant concentration decreases toward the *pn*-junction, which leads to an increase of the bulk diffusion length. Nevertheless, it can be concluded that the diffusion profiles of Figure 4.3



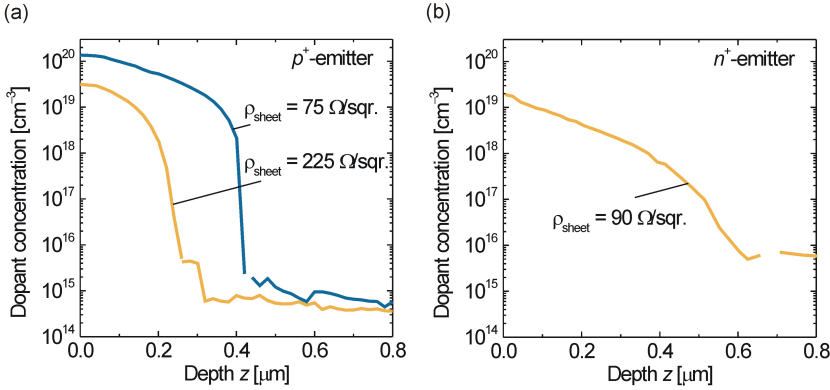


Figure 4.3: (a) Doping profiles of the  $75 \Omega/\square$  and the  $225 \Omega/\square$  boron-diffused emitter. The surface dopant concentrations are  $N_{\text{surf},p+} = 1.3 \times 10^{20} \text{ cm}^{-3}$  and  $3 \times 10^{19} \text{ cm}^{-3}$ , respectively. The depth of the pn-junction is  $z_{\text{jct},p+} = 0.42 \mu\text{m}$  and  $0.26 \mu\text{m}$ , respectively. (b) Doping profile of the  $90 \Omega/\square$  phosphorus-diffused emitter. The surface dopant concentration is  $N_{\text{surf},n+} = 2 \times 10^{19} \text{ cm}^{-3}$ . The depth of the pn-junction is  $z_{\text{jct},n+} = 0.63 \mu\text{m}$ .

create semi-transparent emitters, with the  $75 \Omega/\square$   $p^+$ -emitter showing the largest contribution of the intrinsic bulk recombination to  $J_{0e}$ .

## 4.2.2 Passivation of phosphorus-diffused emitters

### Experimental

Figure 4.4a shows the saturation current density  $J_{0e,n+}$  of the a-Si:H/SiN<sub>x</sub> double-layer passivated  $n^+$ -emitter as a function of the thickness  $d$  of the a-Si:H layer. The samples are measured in the as-deposited (non-annealed) state, and after 5 min annealing at  $300^\circ\text{C}$ . The optimum surface passivation is achieved with  $d > 5 \text{ nm}$ , just as it is shown in Section 4.1 for the passivation of lowly-doped c-Si surfaces.

Annealing for 5 min at  $300^\circ\text{C}$  reduces in particular the emitter saturation current density of the samples with thin a-Si:H layers,  $d \leq 5 \text{ nm}$ . The minimum saturation current density  $J_{0e,n+} = (18 \pm 3) \text{ fAcm}^{-2}$  per side is achieved with  $d = 10 \text{ nm}$  after annealing. The emitter samples that are passivated with SiN<sub>x</sub> double layers at  $400^\circ\text{C}$  show  $J_{0e,n+} = (30 \pm 5) \text{ fAcm}^{-2}$ .

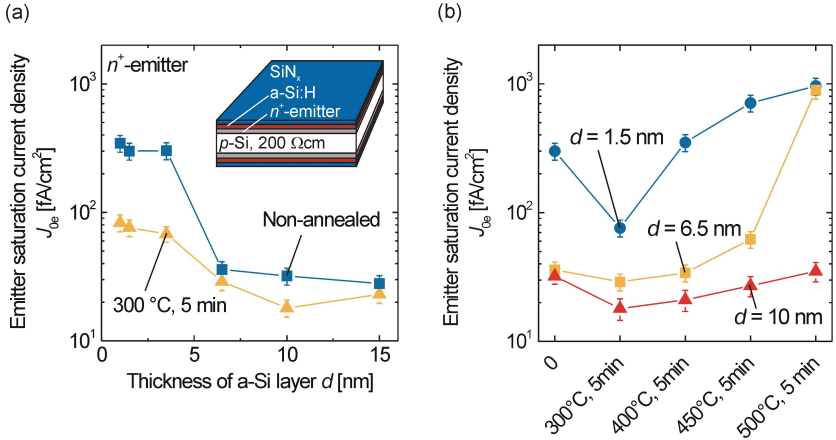


Figure 4.4: Emitter saturation current density  $J_{0e,n+}$  of the a-Si:H/SiN<sub>x</sub>-passivated n<sup>+</sup>-emitter. (a)  $J_{0e}$  as a function of the thickness  $d$  of the a-Si:H layer, non-annealed and after 5 min annealing at 300°C. The optimum passivation is achieved with  $d > 5$  nm.  $J_{0e,n+} = 18 \text{ fAcm}^{-2}$  is achieved with  $d = 10$  nm after annealing. (b)  $J_{0e,n+}$  as a function of the annealing temperature  $T_{\text{anneal}}$ , for  $d = (1.5, 6.5, 10)$  nm. The annealing time is 5 min. The optimum  $J_{0e,n+}$  is achieved with  $T_{\text{anneal}} = 300^\circ\text{C}$  for all  $d$ . The thermal stability increases with increasing  $d$ .

Figure 4.4b shows the emitter saturation current density of the phosphorus-diffused samples during annealing for 5 min in the range from 300°C to 500°C. The thickness  $d$  of the a-Si:H layer is varied,  $d = (1.5, 6.5, 10)$  nm. The optimum surface passivation is achieved by annealing at 300°C, for all  $d$ . The emitter saturation current is most efficiently reduced for thin a-Si:H layers, leading to a reduction by a factor of 4 for  $d = 1.5$  nm.

With  $d = 10$  nm, the passivation is stable up to 500°C. The annealed sample shows  $J_{0e,n+} = (35 \pm 5) \text{ fAcm}^{-2}$ , which is still in the same range as what is obtained with the SiN<sub>x</sub> surface passivation. Both samples with thinner a-Si:H layers,  $d = 1.5$  and 6.5 nm, show  $J_{0e,n+} \approx 10^3 \text{ fAcm}^{-2}$  after annealing at 500°C, which is also obtained from non-passivated samples.

## Discussion

The above mentioned results show that the a-Si:H/SiN<sub>x</sub> double layers deposited at 230°C allow for a lower surface recombination rate than the SiN<sub>x</sub> double layer deposited at 400°C. The optimum passivation is achieved with the thickness of the a-Si:H layer being larger than  $d \geq 6.5$  nm, just as it is shown in Section 4.1 for the passivation of lowly-doped c-Si surfaces. Annealing at 300°C permits the optimum surface passivation, while annealing at higher temperatures finally leads to de-passivation.

The thermal stability of the surface passivation increases with increasing thickness of the a-Si:H layer. The passivation is stable up to annealing at 500°C for 5 min, with  $d = 10$  nm. This complies well with recent results published by Bentzen et al. on the temperature stability of a-Si:H/SiN<sub>x</sub> double layers on lowly-doped *p*-type c-Si. They found the surface passivation to improve by annealing up to 500°C with  $d = 100$  nm [86].

### 4.2.3 Passivation of boron-diffused emitters

#### Experimental

Figure 4.5a shows the emitter saturation current density of the a-Si:H/SiN<sub>x</sub>-passivated boron-diffused emitters as a function of the a-Si:H thickness  $d$ , after annealing for 5 min at their respective optimum temperature which is 400°C for the 225 Ω/□-emitter, and 450°C for the 75 Ω/□-emitter, respectively. There is again a significant decrease of the saturation current density from  $d < 5$  nm to  $d > 5$  nm, like on lowly-doped c-Si surfaces and on the  $n^+$ -emitter.

The optimum surface passivation is achieved with  $d = 10$  nm for both emitters, resulting in a minimum saturation current density of  $J_{0e,p+} = (24 \pm 4)$  fAcm<sup>-2</sup> for the 225 Ω/□-emitter, and of  $J_{0e,p+} = (130 \pm 20)$  fAcm<sup>-2</sup> for the 75 Ω/□-emitter.

Figure 4.5b shows the saturation current density of both boron-diffused emitters during annealing in the range from 300°C to 500°C. The thickness of the a-Si:H layer is  $d = 10$  nm. The corresponding results of the phosphorus-diffused emitter of Figure 4.4b are shown for comparison. Samples with as-deposited a-Si:H/SiN<sub>x</sub> layers show saturation current densities around 10<sup>3</sup> fA/cm<sup>2</sup>, which is also measured on non-passivated samples.

Annealing strongly reduces  $J_{0e,p+}$ . The optimum surface passivation is achieved by annealing for 5 min in the range from 400°C to 450°C. The emitter saturation current is then stable during annealing up to 500°C for 1 min, and increases to  $J_{0e,p+} = (67 \pm 10)$  fAcm<sup>-2</sup> after 5 min at 500°C for the 225 Ω/□-emitter.

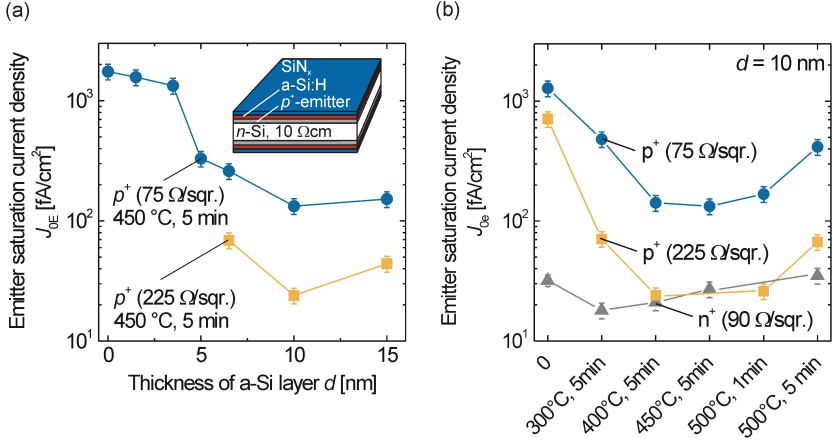


Figure 4.5: Emitter saturation current density  $J_{0e,p+}$  of the a-Si:H/SiN<sub>x</sub>-passivated  $p^+$ -emitters. (a)  $J_{0e,p+}$  as a function of the thickness  $d$  of the a-Si:H layer, for the 75  $\Omega/\square$ -emitter and the 225  $\Omega/\square$ -emitter. The samples are annealed at their optimum temperature for 5 min. The optimum passivation is achieved with  $d \geq 5$  nm. (b)  $J_{0e,p+}$  as a function of the annealing temperature  $T_{\text{anneal}}$  and of the annealing time  $t_{\text{anneal}}$ . The thickness of the a-Si:H layer is  $d = 10$  nm. The optimum  $J_{0e,p+} = (24 \pm 4) \text{ fAcm}^{-2}$  is achieved with  $T_{\text{anneal}} = 400^\circ\text{C}$  for the 225  $\Omega/\square$ -emitter, and  $J_{0e,p+} = (130 \pm 20) \text{ fAcm}^{-2}$  with  $T_{\text{anneal}} = 450^\circ\text{C}$  for the 75  $\Omega/\square$ -emitter, with  $t_{\text{anneal}} = 5$  min. The corresponding curve for the  $n^+$ -emitter is shown for comparison.

## Discussion

Boron-diffused emitters are passivated by a-Si:H/SiN<sub>x</sub> double layers. The results show that a-Si:H/SiN<sub>x</sub> double layers permit the passivation of boron-diffused emitters with the same high quality as on phosphorus-doped emitters. The surface passivation is stable up to annealing at 500°C.

The higher saturation current of the 75  $\Omega/\square$ -emitter when compared to the 225  $\Omega/\square$ -emitter is attributed to the higher intrinsic carrier recombination rate in the emitter bulk due to the higher dopant concentration, as shown in Section 4.2.1. When applying the a-Si:H/SiN<sub>x</sub> passivation scheme of this work to boron-diffused emitters that feature smaller surface dopant concentrations than  $N_{\text{surf},p+} \leq 2 \times$

$10^{19} \text{ cm}^{-3}$ , it was shown that the emitter saturation current densities were smaller than  $J_{0e,n+} < 100 \text{ fAcm}^{-2}$ , even for low sheet resistivities  $\rho_{\text{sheet}} \approx 50 \Omega/\square$ . The quality of the surface passivation was the same as with thermally grown oxide [87].

Non-annealed a-Si:H/SiN<sub>x</sub>-layers have no passivating effect on the boron-diffused emitters of this work, as shown in Figure 4.5b. In contrast, the  $n^+$ -emitter is already well passivated with  $J_{0e,n+} = (32 \pm 5) \text{ fAcm}^{-2}$  by the as-deposited a-Si:H/SiN<sub>x</sub> layers. However, the reason for this different behavior is not yet understood.

The fact that both,  $n^+$ - and  $p^+$ -surfaces are passivated equally well by a-Si:H, is due to the capture cross sections of the a-Si:H/c-Si interface recombination centers being of the same order of magnitude for electrons and holes, as shown by Equation 2.18. The emitter is in *lli* conditions due to its high dopant concentration, and therefore the carrier recombination rate is limited by the capture of the minority carriers. Assuming that the interface defect densities for the  $n^+$ - and the  $p^+$ -samples are the same, the surface recombination rate is determined by  $\sigma_p$  for the  $n^+$ -emitter, and by  $\sigma_n$  for the  $p^+$ -emitter. From Equation 2.18 then follows

$$\frac{J_{0e,n+}}{J_{0e,p+}} \approx \frac{\sigma_p}{\sigma_n}, \quad (4.1)$$

which means that the capture cross sections for electrons and holes are of the same order of magnitude, because  $J_{0e,n+}$  and  $J_{0e,p+}$  are of the same order of magnitude. The same result was obtained in Reference [87] from a review of measured emitter surface recombination velocities of  $n^+$ -type and  $p^+$ -type emitters, as a function of the surface dopant concentration and the type of passivation layer (SiO<sub>2</sub>, SiN<sub>x</sub>, and a-Si:H), by finite-element numerical device simulation [41, 87].

#### 4.2.4 Stability under UV irradiation

The stability of the surface passivation under illumination is essential for the industrial applicability of a surface passivation scheme. Due to the high photon energy, the ultraviolet (UV) fraction of the solar spectrum has the most detrimental effect on dielectric passivation layers.

#### Experimental

The stability of the a-Si:H/SiN<sub>x</sub> double layer passivation under ultraviolet light is investigated by irradiating the phosphorus-diffused samples of Section 4.2.2 with UV light of an intensity of  $25 \text{ mWcm}^{-2}$  in the wavelength range from 280 nm to 400 nm. One phosphorus-diffused sample that is passivated by SiN<sub>x</sub> at 400°C, as shown in Section 4.2.2, is subject to the same treatment for comparison.

The thickness of the a-Si:H layer is 6.5 nm, which is the optimum in terms of both, surface passivation and transparency for the incident light. Section 8.2 shows that  $d = 6.5$  nm leads to the maximum efficiency of solar cells that feature an a-Si:H/SiN<sub>x</sub>-passivated emitter on the illuminated front side.

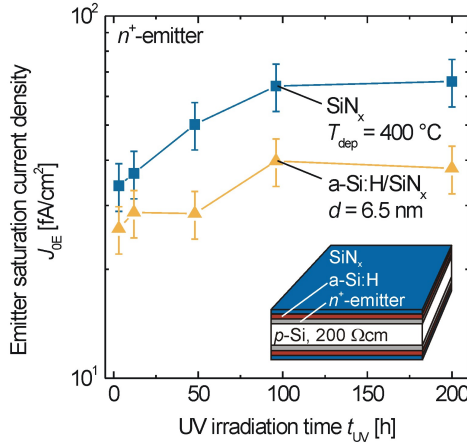


Figure 4.6: Emitter saturation current density  $J_{0e,n+}$  of the a-Si:H/SiN<sub>x</sub>-passivated  $n^+$ -emitter during UV irradiation. The results of a SiN<sub>x</sub>-passivated sample are shown for comparison. The passivation is stable up to 200 h of irradiation. The lines are guides to the eye.

A 3 mm thick glass sheet laminated with 2 mm of ethylene vinyl acetate on one side covers the samples during the UV irradiation in order to simulate the UV spectrum which reaches solar cells in a laminated photovoltaic module. The irradiation time is 200 h, which corresponds to 1 year of outdoor illumination in terms of deposited energy [88].

Figure 4.6 shows the measured emitter saturation current  $J_{0e,n+}$  as a function of the UV irradiation time. The emitter saturation current of the a-Si:H/SiN<sub>x</sub>-passivated sample increases from  $J_{0e,n+} = (26 \pm 4)$  fAcm<sup>-2</sup> to  $(38 \pm 6)$  fAcm<sup>-2</sup> after 200 h of irradiation. The sample with 400°C SiN<sub>x</sub>-passivation shows an increase of the emitter saturation current from  $(34 \pm 5)$  fAcm<sup>-2</sup> to  $(66 \pm 10)$  fAcm<sup>-2</sup>.

## Discussion

The a-Si:H/SiN<sub>x</sub> double layer passivation shows a better stability under UV irradiation than the SiN<sub>x</sub>-passivation. The emitter saturation current saturates to constant values with increasing irradiation time, for both kinds of samples. It is therefore concluded that the passivation layers are also stable for longer irradiation times.

The UV stability of the a-Si:H/SiN<sub>x</sub> double layer passivation developed in this work is also shown for boron-diffused emitters, in Reference [87]. It is shown that  $J_{0e,p+}$  is also stable for at least 200 h under the test conditions described above. Furthermore, Reference [87] shows that the stability of the a-Si:H/SiN<sub>x</sub> is superior to that of thermally grown oxide.

## 4.3 Passivation of textured surfaces

High-efficiency solar cells typically feature textured front surfaces in order to reduce their reflectivity. From the technological point of view, it is favorable to process both sides of the solar cell as symmetrically as possible in order to reduce the number of masking steps. A comparison of the passivation quality of a-Si:H single layers and that of a-Si:H/SiN<sub>x</sub> double layers on textured and planar c-Si surfaces is shown in Section 4.3.2. Section 4.3.1 gives an overview on how the changed surface morphology due to the texturing affects the efficiency of the surface passivation, when compared to planar wafers.

### 4.3.1 Contributions to the surface recombination rate

The lifetime samples that are used to assess the passivation quality on the textured surface are prepared by anisotropic etching of (100)-oriented 1.5 Ωcm *p*-type FZ-Si wafers in KOH/isopropanol solution. The resulting surface features randomly distributed pyramids of about 5–10 μm height. The flanks of the random pyramids are (111)-oriented, and thus form an angle of 54.7° to the original (100)-surface. The effective surface area of a wafer that is homogeneously textured with pyramids, is therefore increased by a factor of 1.74 when compared to the original (100)-oriented planar surface [89].

The impact of surface texturing on the effective surface recombination velocity  $S_{\text{eff}}$  is not a simple geometrical one, as described in the following. Equation 2.16 shows that the surface recombination velocity depends on the density  $D_{\text{it}}$  of non-passivated recombination centers per unit area of the wafer, on their capture cross

sections  $\sigma_{n/p}$  for electrons (n) and holes (p), and on the energetic distribution of the recombination centers within the c-Si bandgap.

The density of surface atoms is 1.15 times higher at the (111) surface than at the (100) surface, which makes 2 times more atoms per unit area on the textured wafer, than on the planar wafer. One surface atom of the (111)-oriented surface has only one non-saturated electronic orbital, i.e. one dangling bond, whereas surface atoms at the (100)-oriented surface feature two dangling bonds. Reconstruction of the surfaces was found to occur by the formation of dimers from neighboring atoms, thus reducing the dangling bond density by about a factor of 1/2 in both cases [17]. Therefore, the total densities of dangling bond states *per unit area of the wafer* are equal for the non-passivated planar and textured wafers,  $D_{\text{DB,ext.}} = D_{\text{DB,planar}} = D_{\text{DB}}$ .

Therefore, only the orientation-dependent efficiency of the respective surface passivation technique determines the density  $D_{\text{it}}$  of the remaining recombination centers at the passivated surface of the wafer:

$$\begin{aligned} D_{\text{it,ext.}} &= D_{\text{DB}} \times (1 - \eta_{\text{ext.}}), \text{ and} \\ D_{\text{it,planar}} &= D_{\text{DB}} \times (1 - \eta_{\text{planar}}), \end{aligned} \quad (4.2)$$

where  $\eta$  is the ratio of the density of passivated dangling bonds to the total density of dangling bonds  $D_{\text{DB}}$ , i.e. the efficiency of the surface passivation.

It was experimentally shown in several publications [17, 90, 91, 92, 93, 94] for surface passivation with SiO<sub>2</sub> and SiN<sub>x</sub>, that (111)-oriented surfaces are usually more difficult to passivate than (100)-oriented ones. (111)-oriented surfaces showed higher defect densities than (100)-oriented surfaces after passivation by thermally grown oxide and PECVD-SiN<sub>x</sub>. This was attributed to the different bond configurations of the surface atoms and the different surface reconstruction mechanisms, which lead to different distribution functions for the surface recombination levels throughout the c-Si bandgap. Therefore,  $\eta_{\text{ext.}} < \eta_{\text{planar}}$  due to the different surface orientations.

Furthermore, the passivation of the textured surface by deposited layers like SiN<sub>x</sub> or a-Si:H has the risk of pinhole formation, which can preferentially take place at the sharp pyramid tops, and again leads to  $\eta_{\text{ext.}} < \eta_{\text{planar}}$  due to technological reasons.

The literature data about the capture cross sections of the dangling bond surface states scatters by a few orders of magnitude, and also depends on the type of surface passivation. There is no evidence for different capture cross sections of the dangling bonds at the (111)- and at the (100)-surfaces with SiO<sub>2</sub>- or SiN<sub>x</sub>-passivation [93, 95]. No data are available for the a-Si:H/c-Si material system.



In conclusion, textured and planar wafers show equal total dangling bond densities per unit area of the wafer. However, the efficiency of the surface passivation by  $\text{SiO}_2$  and  $\text{SiN}_x$  was found to be usually lower for (111)-oriented surfaces than for (100)-oriented ones, which is the main reason for the commonly found relation  $S_{\text{eff, text.}} > S_{\text{eff, planar}}$ .

### 4.3.2 Passivation of lowly-doped surfaces

#### Experimental

Both sides of the KOH-textured  $1.5 \Omega\text{cm}$   $p$ -type wafers are passivated by a-Si:H single layers and by a-Si:H/ $\text{SiN}_x$  double layers, respectively. The thickness of the  $\text{SiN}_x$  layer is 100 nm in order to obtain the optimum anti reflective coating. The thickness of the a-Si:H layer is calculated from the deposition rate  $r = 10 \text{ nm/min}$  on planar surfaces, and is therefore only a nominal value for the textured samples. The effective surface recombination velocity is obtained from QSSPC measurements.

Figure 4.7a shows the SRV of the wafers with a-Si:H single-layer passivation, as a function of the thickness  $d$  of the a-Si:H layer. The data of the planar samples of Section 4.1 are shown for comparison. The SRV is obtained at the excess carrier density  $\Delta n = 10^{15} \text{ cm}^{-3}$ . Both, textured and non-textured samples show the significant decrease of  $S_{\text{eff}}$  from  $d \leq 5 \text{ nm}$  to  $d \geq 6.5 \text{ nm}$  that is described in Section 4.1. The effective surface recombination velocity of the textured samples is  $S_{\text{eff, text.}} = (18 \pm 3) \text{ cm/s}$  for  $6.5 \text{ nm} \leq d \leq 10 \text{ nm}$ , and decreases to  $S_{\text{eff, text.}} = (5.7 \pm 0.6) \text{ cm/s}$  for  $d = 15 \text{ nm}$ . Figure 4.7c shows that the ratio of  $S_{\text{eff, text.}}/S_{\text{eff, planar}}$  also decreases from 18 to 1.7 with increasing a-Si:H-thickness from 3.5 nm to 15 nm. The maximum deposited thickness of  $d = 15 \text{ nm}$  allows to achieve the ratio of  $S_{\text{eff, text.}}/S_{\text{eff, planar}} = (1.7 \pm 0.5)$ , which is in the same range as what was found for the surface passivation with  $\text{SiN}_x$  at  $400^\circ\text{C}$  [64, 93]. The application of thicker a-Si:H films is not feasible, because they form blisters during annealing, due to the large hydrogen content of the a-Si:H.

Figure 4.7b shows the SRV of the a-Si:H/ $\text{SiN}_x$  double-layer passivated wafers. Again, textured and non-textured samples show the decrease of  $S_{\text{eff}}$  from  $d \leq 5 \text{ nm}$  to  $d \geq 6.5 \text{ nm}$  that is described in Section 4.1, although the effective surface recombination velocity of the textured samples decreases steadily also from  $d = 6.5 \text{ nm}$  to 15 nm. Figure 4.7c shows that the ratio of the effective SRVs,  $S_{\text{eff, text.}}/S_{\text{eff, planar}}$  is almost constant at  $(3.1 \pm 0.1)$  for  $d \leq 6.5 \text{ nm}$ , and decreases significantly to  $1.4 \pm 0.5$  with  $d = 10 \text{ nm}$  and  $1.3 \pm 0.5$  with  $d = 15 \text{ nm}$ . This is among the lowest values found in the literature for the passivation by  $\text{SiO}_2$  and by PECVD- $\text{SiN}_x$ ,  $S_{\text{eff, text.}}/S_{\text{eff, planar}} = 1.3 \dots 2.5$ , for optimized passivation layers [64, 93].

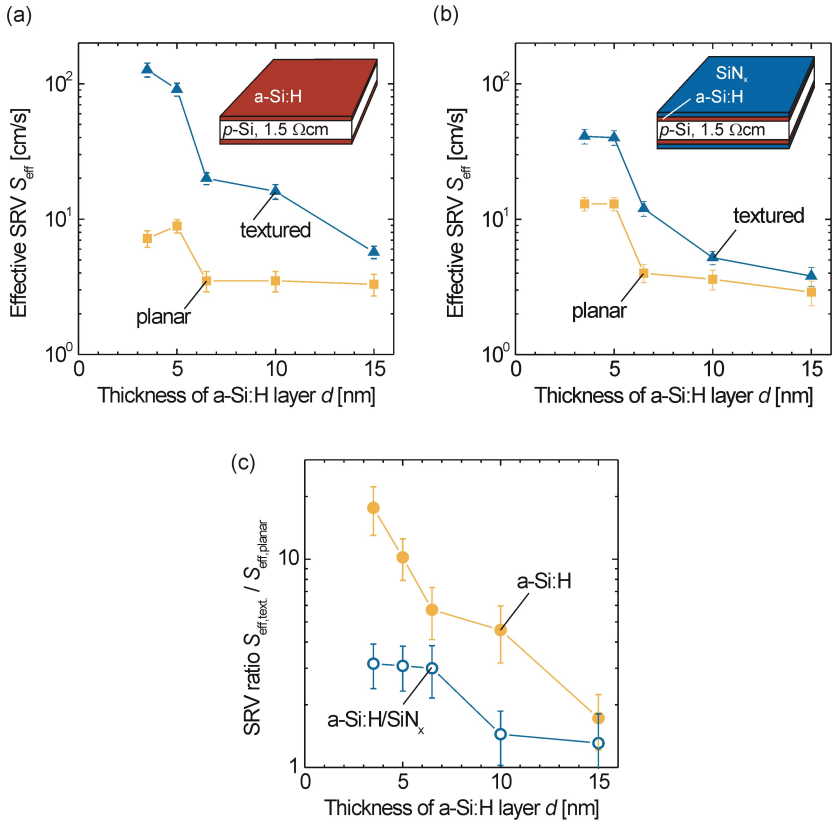


Figure 4.7: Effective SRV at  $\Delta n = 10^{15} \text{ cm}^{-3}$  of planar and KOH-textured 1.5  $\Omega\text{cm}$  *p*-type wafers passivated with (a) *a*-Si:H single layers, and (b) with *a*-Si:H/SiN<sub>x</sub> double layers. The thickness  $d$  of the *a*-Si:H layer is varied. The thickness of the SiN<sub>x</sub> layer is 60 nm on the planar wafers, and 100 nm on the textured wafers for optimum anti reflective coating. (c) The ratio of the effective surface recombination velocities of textured wafers to that of planar wafers,  $S_{\text{eff, text.}}/S_{\text{eff, planar}}$ .

## Discussion

Three effects are identified from the measurements shown in this section:

- The significant decrease of  $S_{\text{eff}}$  from  $d \leq 5$  nm to  $d \geq 6.5$  nm is present for both, textured and planar surfaces featuring both, a-Si:H- and a-Si:H/SiN<sub>x</sub>-passivation. This effect is therefore due to the properties of the a-Si:H layer, irrespective of the surface morphology of the c-Si wafer. The most probable explanation is that unpassivated pinholes remain in the a-Si:H layer when  $d \leq 5$  nm, as discussed in Section 4.1.
- The ratio  $S_{\text{eff, text.}}/S_{\text{eff, planar}}$  decreases steadily with increasing nominal a-Si:H thickness  $d$  from quite large values to around 1.5 for both, a-Si:H single layer passivation and a-Si:H/SiN<sub>x</sub> double layer passivation. This effect is attributed (i) to the passivation of the dangling bonds at the (111) surfaces becoming more effective with increasing  $d$ , or (ii) to the closing of additional pinholes in the a-Si:H layer on the textured samples, when  $d \geq 10$  nm. The additional pinholes are located presumably at the sharp pyramid tops.
- The use of a-Si:H/SiN<sub>x</sub> double layers instead of a-Si:H single layers leads to a significantly better passivation of the textured c-Si surfaces, especially when the a-Si:H layer is thin,  $d \leq 6.5$  nm. With  $d \geq 10$  nm, the efficiency of the SRV of the textured c-Si surface is at least as low as what has been achieved with thermally grown oxide or with PECVD-SiN<sub>x</sub> deposited at 400°C. This is the only experiment of this work where the SiN<sub>x</sub> capping layer actually enhances the quality of the surface passivation when compared to a-Si:H single-layer passivation.



## 5 Model of the a-Si:H/c-Si heterojunction

Unlike the passivation with dielectric layers like  $\text{SiN}_x$  or  $\text{SiO}_2$ , that have band gap energies of several eV, the possibility of charge carriers to diffuse or tunnel into the amorphous silicon layer is not negligible *a priori*. Therefore, not only recombination through the defects at the a-Si:H/c-Si interface, but also recombination in the a-Si:H bulk has to be taken into account in order to model the contributions the effective carrier recombination rate at the a-Si:H passivated surface.

Section 5.1 describes the heterostructure simulation program that is used to separate the recombination through the interface states from the recombination through the a-Si:H bulk defect states by simulating the measured injection-dependence of the effective carrier lifetime of a-Si:H passivated c-Si wafers. In order to describe the carrier recombination through the defect states, their energetic distribution function and their capture cross sections for electrons and holes have to be known.

A model for the recombination centers in the a-Si:H bulk and at the a-Si:H/c-Si interface is developed in the sections 5.2 and 5.3, which is based on measurements of the distribution function of the density of states in the a-Si:H bulk, and on data extracted from the literature.

### 5.1 The heterostructure simulation package AFORS-HET

AFORS-HET is an open-source on demand software tool for the one-dimensional simulation of semiconductor multilayer structures, developed at the Hahn-Meitner Institute (HMI), Berlin [96, 97]. An arbitrary sequence of semiconducting layers can be specified by stating their respective electronic and optical properties, and the distribution function of the defect states. Both, intrinsic and Shockley-Read-Hall type recombination are considered in the calculation. The distribution of defect states can also be specified for each interface between adjacent layers, in order to simulate the interface recombination. Each layer is defined by its width, dielectric constant, electron affinity, bandgap energy, valence and conduction band densities of states, donor and acceptor concentrations, thermal velocities of electrons and holes, Auger recombination coefficients for electrons and holes, radiative recombination coefficient, and the distribution functions and capture cross sections of defects within the bandgap. The defects can be defined as donors or

acceptors, depending on their charge state when filled with an electron. Only energy-independent capture cross sections can be defined.

AFORS-HET numerically solves Poisson's equation and the continuity equations for electrons and holes with the appropriate boundary conditions in one dimension under steady state conditions, and since version 2.0 also in transient mode. The user can specify the externally applied voltage, current, and the spectrum of the illumination. The set of coupled partial differential equations is transformed into a set of nonlinear algebraic equations by the method of finite differences. The resulting nonlinear equations are solved iteratively. The free electron and hole densities, and the electrostatic potential at each gridpoint are used as independent variables. All other variables in the discretized set of differential equations are expressed as functions of these three independent variables.

Thus, the internal cell characteristics, such as band diagrams, local generation and recombination rates, and free and trapped carrier densities are calculated, which allows for the simulation of various characterization methods like current-voltage, quantum efficiency, or lifetime measurements. The simulation of steady-state lifetime measurements as it is used in this work has been implemented in version 2.2. The semiconductor equations are solved for steady-state illumination, under open-circuit conditions. The effective carrier lifetime

$$\tau_{\text{eff}} = \frac{\int \Delta n(z) dz}{\int G(z) dz} \quad (5.1)$$

is then calculated from the simulated local carrier density  $\Delta n(z)$  and local generation rate  $G(z)$ . It can be directly compared to the effective carrier lifetime obtained from QSSPC measurements of the a-Si:H passivated lifetime samples, as the spectral distribution of the flashlamp illumination in the QSSPC experiments is also used in the simulation. Thus, the user-defined defect model can be adjusted to obtain the best fit of the simulated injection-dependent carrier lifetime to the experimental data.

A detailed description of the models implemented in AFORS-HET is provided in the online help file [96]. A short overview is given in the following:

- **Transport**

AFORS-HET accounts for impurity scattering and carrier-carrier scattering within crystalline silicon, which means that the electron and hole mobilities are calculated iteratively according to the local carrier density. The starting values correspond to the Dorkel-Leturcq model [98]. The specified carrier mobilities of non-crystalline silicon layers are kept constant during the calculation.

- **Optics**

The multiple reflections and coherence model accounts for reflection at interfaces between adjacent layers, and at the front and rear surface of the device. Interference effects are considered. Optical layers, such as anti reflective coatings can be defined. The wavelength-dependent refractive index and absorption coefficient of each layer have to be specified to calculate the local absorption, and thus the generation rate.

- **Recombination**

The recombination rate through defect states is calculated by the extended SRH formalism described in the Equations 2.12 and 2.16. The distribution function of the density of states, and the carrier capture cross sections have to be specified for each kind of recombination center. The intrinsic recombination rate is calculated according to the Dziewior-Schmid model as the sum of the Auger recombination rate and the radiative recombination rate,  $U_{\text{intr,DS}} = C_n n^2 p + C_p n p^2 + C_{\text{rad}} n p$ . This model is only applicable if the parameters  $C_n$ ,  $C_p$ , and  $C_{\text{rad}}$  are adjusted to the actual doping concentration of the investigated silicon wafer (see Equation 2.9). Therefore, the intrinsic recombination rate is calculated from the parameterization developed by Kerr and Cuevas (equations 2.10 and 2.11), and  $C_n$ ,  $C_p$ , and  $C_{\text{rad}}$  are then fitted to reproduce the correct injection dependence of the intrinsic carrier lifetime.

## 5.2 Model of the a-Si:H bulk defects

This section shows a model of the electronic states within the bandgap of amorphous silicon. The distribution function of the density of the defect states, their physical origin, and their capture cross sections for electrons and holes are derived from experiments, and from literature data.

### 5.2.1 Distribution function of the density of states

Although there is no long-range order in the atomic array of amorphous semiconductors, the local bond configuration of the constituent atoms is equivalent to that of the corresponding crystalline material. It was shown in Reference [99] by using the tight-binding model, that the same energetic bandgap forms in amorphous silicon as in crystalline silicon. However, *hydrogenated* amorphous silicon, as it is naturally deposited by PECVD from  $\text{SiH}_4$  plasma, contains up to 20% of bonded hydrogen. The partial replacement of Si-Si bonds by Si-H bonds of larger bonding

energy moves the valence band edge toward lower energies, thus expanding the energetic bandgap as shown in References [27, 100]. Schmidt et al. showed that the bandgap energy of a-Si:H films deposited by direct-PECVD at low temperatures,  $200^\circ\text{C} < T < 250^\circ\text{C}$ , is  $E_{g,a\text{-Si:H}} = (1.72 \dots 0.05)$  eV, regardless of the specific deposition parameters [28].

## Experimental

Figure 5.1 shows the density of occupied states in a 10 nm thin a-Si:H layer that is deposited by PECVD at  $225^\circ\text{C}$  on a *p*-type c-Si wafer, as described in Section 3.1. The data were obtained by UV-photoelectron spectroscopy (PES) measurements of the yield of photoelectrons under UV-irradiation, at Hahn-Meitner Institute, Berlin. The sample is irradiated by ultraviolet light, and the yield of photo-emitted electrons as a function their kinetic energy, is obtained as a measure for the density  $N_{\text{occ}}$  of occupied electronic states in the a-Si:H bulk as shown in References [28, 101, 102].

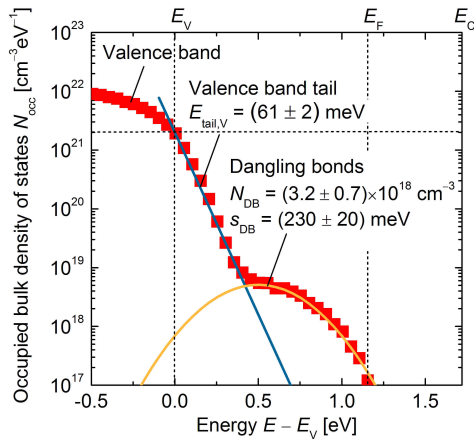


Figure 5.1: Occupied bulk density of states in the 10 nm thin a-Si:H layer deposited on a *p*-type c-Si wafer, as obtained from UV-photoelectron yield spectroscopic measurements. The lines denote the best fits of Equations 5.2 and 5.4 to the measured DOS (shown as symbols). Thanks to Dr. Lars Korte for performing the PES measurements at Hahn-Meitner Institute, Berlin.



The density of occupied states decays from the valence band edge towards the Fermi energy at  $E_F - E_V = (1.16 \pm 0.02)$  eV. The Fermi energy is determined from the cut-off energy level in the yield spectrum of photo-emitted electrons. The energetic position of the valence band edge is defined by the change of the slope of the density of states (DOS), from the DOS of the valence band states  $N_{\text{occ}} \propto (E_V - E)^{0.5}$  for  $E < E_V$  to the exponentially decaying DOS of the localized band-tail states within the bandgap, as shown in References [101, 103]. The nature of the electronic states within the bandgap is explained in the following Sections.

### Band tail states

In contrast to crystalline semiconductors, the density of states in amorphous silicon does not completely vanish within the bandgap, which is due to the lacking long-range order. The lack of periodicity and symmetry in the atomic array leads to the formation of localized electronic states called *band tail states* whose distribution function decays exponentially toward the center of the energetic bandgap [104]:

$$\begin{aligned} N_{\text{tail,V}}(E) &= N_{0,\text{V}} \times \exp\left(\frac{E_V - E}{E_{\text{tail,V}}}\right) \quad \text{for the valence band, and} \\ N_{\text{tail,C}}(E) &= N_{0,\text{C}} \times \exp\left(\frac{E - E_C}{E_{\text{tail,C}}}\right) \quad \text{for the conduction band,} \end{aligned} \quad (5.2)$$

where  $N_{0,\text{V}} = N_{0,\text{C}} = 2 \times 10^{21} \text{ cm}^{-3}$  is the density of states at the valence band edge and at the conduction band edge, as shown in References [101, 103]. The *Urbach energies*  $E_{\text{tail,V}}$  and  $E_{\text{tail,C}}$  are a measure for the disorder broadening of the energetic bands by localized states. Qualitatively, larger values of  $E_{\text{tail,V/C}}$  correspond to larger disorder in the amorphous silicon film. The Urbach energies of undoped a-Si:H found in literature are in the range of  $E_{\text{tail,V}} = (50 \dots 70)$  meV and  $E_{\text{tail,C}} = (20 \dots 40)$  meV [28, 29, 105].

The measured density of states is fitted best with  $E_{\text{tail,V}} = (61 \pm 2)$  meV, as shown in Figure 5.1. The Urbach energy of the conduction band tail distribution function,  $E_{\text{tail,C}}$  is not accessible by the experiment because the PES measurement reveals only the density of occupied states. However, References [28, 29, 105] show that the conduction-band Urbach energy is  $E_{\text{tail,C}} \approx 0.5E_{\text{tail,V}}$ . The value  $E_{\text{tail,C}} = 0.3$  eV is therefore used throughout this work.

The valance-band tail states are donor-like (positive when occupied by a hole), and the conduction-band tail states are acceptor-like (negative when occupied by an electron). Charge neutrality in the a-Si:H bulk therefore requires that

$$\int_{E_V}^{E_F} N_{\text{tail,C}}(E) dE = \int_{E_F}^{E_C} N_{\text{tail,V}}(E) dE, \quad (5.3)$$

if no other electronic states are present within the a-Si:H bandgap. Equation 5.3 results in  $E_F = E_V + 1.17$  eV with the parameters  $N_{0,V} = N_{0,C} = 2 \times 10^{21}$  cm<sup>-3</sup>,  $E_{\text{tail},V} = 61$  meV,  $E_{\text{tail},C} = 30$  meV, and  $E_{g,a-Si:H} = 1.72$  eV as shown above. The value  $E_F = E_V + (1.16 \pm 0.02)$  eV obtained from the results of the PES measurements shown in Figure 5.1, agrees with the result of Equation 5.3 within the uncertainty interval of the measurement.

### Dangling bond states

Non-saturated electronic orbitals are the major structural defects in amorphous silicon [28, 106]. These *dangling bonds* are amphoteric defects with three states that are denoted by  $\delta^0$  (neutral, filled with one electron),  $\delta^-$  (negatively charged, filled with two electrons), and  $\delta^+$  (positively charged, empty). Powell and Deane showed that the distribution function  $D(E)$  of the dangling bond states within the a-Si:H bandgap, depends on the position of the Fermi level  $E_F$ : The density of states forms such that the free energy of the system is minimized [107, 108]. In thermal equilibrium, virtually all dangling bonds in  $n$ -type a-Si:H are in the  $\delta^-$  state, i. e.  $D(E) \approx 0$  for  $E > E_F$ . This result agrees with the distribution function of defect states within the a-Si:H bandgap shown in Figure 5.1. Due to statistical fluctuations of the bonding angle and bonding lengths of neighboring atoms which influence the energy level of the dangling bond orbital, the distribution function of the dangling bond defects follows a gaussian shape centered at  $E_{\text{center}}$  as shown in References [28, 108, 109],

$$D(E) = \frac{N_{\text{DB}}}{s_{\text{DB}}\sqrt{2\pi}} \exp\left(-\frac{1}{2}\left(\frac{E_{\text{center}} - E}{s_{\text{DB}}}\right)^2\right), \quad (5.4)$$

where  $N_{\text{DB}}$  is the total density of dangling bonds (in cm<sup>-3</sup>), and  $s_{\text{DB}}$  is the standard deviation of the distribution function.

Figure 5.1 shows the best fit of Equation 5.4 to the density of states obtained from PES measurements, with  $E_{\text{center}} - E_V = (0.5 \pm 0.1)$  eV, the standard deviation being  $s_{\text{DB}} = (0.23 \pm 0.02)$  eV, and the defect density being  $N_{\text{DB}} = (3.2 \pm 0.7) \times 10^{18}$  cm<sup>-3</sup>. This value of  $N_{\text{DB}}$  is about two orders of magnitude higher than typical values of amorphous silicon that was optimized for the fabrication of amorphous silicon solar cells [110]. However, as the a-Si:H films shown in this work are optimized for the surface passivation of c-Si and not for an optimum a-Si:H bulk passivation, the density of the bulk defects is to be expected to be non-optimum. Furthermore, the total density of the dangling bond states  $N_{\text{DB}}$  depends on the post-deposition treatment of the a-Si:H film, and is therefore a variable in the defect model described in this Section.

The semiconductor device simulation software AFORS-HET that is used in this work to model carrier recombination in the a-Si:H bulk and at the a-Si:H/c-Si interface, requires the definition of defect states in the *single-electron scheme* because interaction between charge carriers is not included in the model. Dangling bonds are therefore described by two recombination levels located at  $E_{+/0}$  for the ( $\delta^+ \leftrightarrow \delta^0$ ) transition, and at  $E_{0/-}$  for the ( $\delta^0 \leftrightarrow \delta^-$ ) transition as described in References [106, 108, 111, 112, 113, 114]:

$$\begin{aligned} N_{+/0}(E) &= \frac{N_{\text{DB}}}{s_{\text{DB}} \sqrt{2\pi}} \exp\left(-\frac{1}{2} \left(\frac{E_{+/0} - E}{s_{\text{DB}}}\right)^2\right) \quad (\delta^+ \leftrightarrow \delta^0 \text{ transition}) \\ N_{0/-}(E) &= \frac{N_{\text{DB}}}{s_{\text{DB}} \sqrt{2\pi}} \exp\left(-\frac{1}{2} \left(\frac{E_{0/-} - E}{s_{\text{DB}}}\right)^2\right) \quad (\delta^0 \leftrightarrow \delta^- \text{ transition}), \end{aligned} \quad (5.5)$$

where

$$E_{+/0} = E_{\text{center}} - kT \ln 2 \quad \text{and} \quad E_{0/-} = E_{\text{center}} + U_{\text{eff}} + kT \ln 2, \quad (5.6)$$

as shown in Reference [108]. The distance between the energy levels  $E_{+/0}$  and

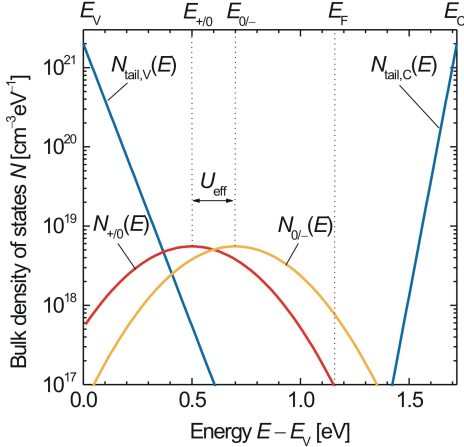


Figure 5.2: *Single-electron effective density of band tail states and dangling bond states within the a-Si:H bandgap, as calculated from the Equations 5.2 and 5.5 with the parameters listed in Table 5.1.*

$E_{0/-}$  is the correlation energy  $U_{\text{eff}} = E_{0/-} - E_{+/0}$  of the dangling bond defects. It depends on the Coulomb interaction of the electrons within the dangling bond, and on contributions due to the lattice relaxation, electron-phonon interactions, and rehybridization of the dangling bond orbitals [106]. It was shown in References [113, 114, 115, 116] that  $U_{\text{eff}} = (0.2 \pm 0.2)$  eV. The commonly used value  $U_{\text{eff}} = 0.2$  eV is also used in this work. The energy levels  $E_{+/0} - E_{\text{V}} = (0.5 \pm 0.1)$  eV and  $E_{0/-} - E_{\text{V}} = (0.7 \pm 0.1)$  eV are then obtained by Equation 5.6 from the value of  $E_{\text{center}} = (0.5 \pm 0.1)$  eV that is determined from fitting Equation 5.4 to the measured density of states shown in Figure 5.1.

### Defect distribution function of the a-Si:H bulk

Figure 5.2 shows the single-electron density of band tail states and dangling bond states within the bandgap of non-doped a-Si:H, as calculated from the Equations 5.2 and 5.5. The parameters listed in Table 5.1 are used for the calculation. They are obtained from the literature and from the measured density of occupied states that is determined from PES measurements as described above, to form a consistent set of parameters. The total density of dangling bonds in the a-Si:H bulk  $N_{\text{DB}} = 3.2 \times 10^{18} \text{ cm}^{-3}$  is determined by fitting Equation 5.4 to the measured density of states of 10 nm thick a-Si:H layer deposited at 225°C, as shown in Figure 5.1.

Table 5.1: *Energetic parameters of the distribution functions of the defects in the a-Si:H bulk, as shown in Figure 5.2. The parameters are used throughout this work.*

Tail states		
	$E_{\text{g,a-Si:H}}$	1.72 eV
	$E_{\text{F,a-Si:H}} - E_{\text{V}}$	1.16 eV
	$E_{\text{tail,V}}$	61 meV
	$E_{\text{tail,C}}$	30 meV
Dangling bonds		
	$E_{+/0} - E_{\text{V}}$	0.50 eV
	$E_{0/-} - E_{\text{V}}$	0.70 eV
	$s_{\text{DB}}$	0.23 eV

### 5.2.2 Carrier capture cross sections

The recombination activity of the defects within the electronic bandgap is determined by the capture time constants  $\tau_{n/p,0} = (v_{\text{th}} N_{\text{defect}} \sigma_{n/p})^{-1}$  for electrons (n) and holes (p), as described in Section 2.2.3. In order to model the carrier recombination through the defect states in the a-Si:H bulk, capture cross sections have to be assigned to the band tail states and to the dangling bond states, whose distribution functions are described by the Equations 5.2 and 5.5.

There are four different capture processes for charge carriers in the amphoteric dangling bond states, which correspond to four capture cross sections:

- The donor-like transitions  $\delta^+ \leftrightarrow \delta^0$  correspond to the capture of
  - Electrons in the positively charged, empty dangling bond orbitals:  $\delta^+ \rightarrow \delta^0$  transition, with the capture cross section  $\sigma_{+/0,n}$ , and
  - Holes in the non-charged dangling bond orbitals containing one electron:  $\delta^0 \rightarrow \delta^+$  transition, with the capture cross section  $\sigma_{+/0,p}$ .
- The acceptor-like transitions  $\delta^0 \leftrightarrow \delta^-$  correspond to the capture of
  - Holes in the negatively charged dangling bond orbitals containing two electrons:  $\delta^- \rightarrow \delta^0$  transition, with the capture cross section  $\sigma_{0/-,p}$ , and
  - Electrons in the non-charged dangling bond orbitals containing one electron:  $\delta^0 \rightarrow \delta^-$  transition, with the capture cross section  $\sigma_{0/-,n}$ .

Table 5.2: Capture cross sections  $\sigma_n$  for electrons and  $\sigma_p$  for holes of the different types of defects in the a-Si:H bulk [117].

Bulk defect	$\sigma_n$ [cm <sup>2</sup> ]	$\sigma_p$ [cm <sup>2</sup> ]
Valence band tail	$1 \times 10^{-17}$	$1 \times 10^{-17}$
Conduction band tail	$1 \times 10^{-17}$	$1 \times 10^{-17}$
Dangling bond ( $\delta^+ \leftrightarrow \delta^0$ )	$2 \times 10^{-15}$	$1 \times 10^{-15}$
Dangling bond ( $\delta^0 \leftrightarrow \delta^-$ )	$7 \times 10^{-15}$	$1 \times 10^{-14}$

Reference [117] gives an overview over the existing literature data on the capture cross sections of the band tail states and of the dangling bond states. The mean values, which are used throughout this work, are given in Table 5.2. The standard deviations of the data are about a factor of 10.

The band tail states actually correspond to the binding electronic orbitals between Si atoms. Their recombination activity is small, which is reflected by the small capture cross section of  $1 \times 10^{-17} \text{cm}^2$ . In contrast, the capture cross sections of the dangling bond states are 2-3 orders of magnitude larger. The Coulomb attraction between the charged dangling bond states and the captured carriers is reflected by the larger capture cross sections of the charged states.

### 5.3 Model of the a-Si:H/c-Si interface defects

This section shows a model of the electronic states at the a-Si:H/c-Si interface. The distribution function of the defect states, and their capture cross sections for electrons and holes are taken from the literature, and are adapted to fit the results shown in Section 5.2.1.

#### 5.3.1 Distribution function of the density of states

Figure 5.3 shows the band diagram of an undoped amorphous silicon film with thickness  $d = 10 \text{ nm}$  that is deposited onto a  $p$ -type crystalline silicon wafer ( $p = 10^{16} \text{ cm}^{-3}$ ), as calculated with AFORS-HET. The a-Si:H/c-Si heterojunction is characterized by the band edge offsets of the valence band  $\Delta E_V$ , and of the conduction band  $\Delta E_C = \Delta E_g - \Delta E_V$ . The value  $\Delta E_g = 600 \text{ meV}$  corresponds to the bandgap energy of  $E_{g,\text{a-Si:H}} = 1.72 \text{ eV}$  that agrees with the measured distribution function of occupied states, and the position of the Fermi level in the bulk of a-Si:H layers deposited in this work, as shown in Section 5.2.1. Furthermore, this value is within the range of  $\Delta E_g = (550 \dots 700) \text{ meV}$  that was obtained from photoelectron yield spectroscopic (PES) measurements and from measurements of the absorption coefficient, for a-Si:H that was deposited at low temperatures  $200^\circ\text{C} < T < 250^\circ\text{C}$  by other groups, as shown in References [27, 28, 29]. The valence band edge offset  $\Delta E_V = (450 \pm 20) \text{ meV}$  was measured by Sebastiani et al. and von Maydell et al. by photoelectron yield spectroscopy, as described in References [118, 119]. Since it was shown in References [118, 119] that the value of  $\Delta E_V$  shows only a small dependence on the actual deposition parameters, it is used throughout this work.

Non-saturated, dangling bonds of silicon atoms are the dominant type of defect at the c-Si surface [17]. However, little is known about the actual distribution function and the capture cross section of these defects, when the surface is passivated by a-Si:H. First investigations of the a-Si:H/c-Si interface density of states with the field-dependent surface photovoltage technique by von Maydell et al. [119] have

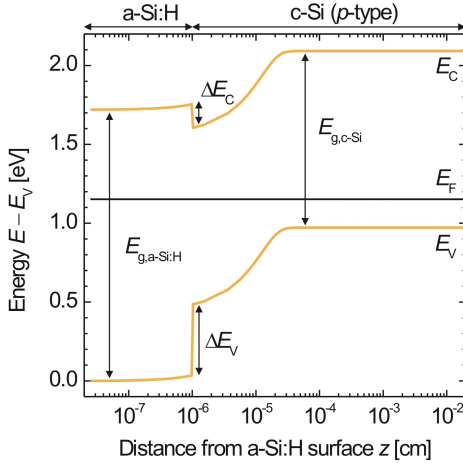


Figure 5.3: Band diagram of an a-Si:H passivated c-Si wafer in thermal equilibrium, without illumination. The position  $z$  is measured perpendicular to the surface.

shown a broad, U-shaped distribution which is almost constant in the center of the c-Si bandgap, until a distance of 0.3 eV to the band edges, as shown in Figure 5.4.

### Comparison to the SiO<sub>2</sub>/c-Si interface

The same kind of defect distribution as it is shown in Figure 5.4, was also described by Füssel et al. for the well-investigated SiO<sub>2</sub>/c-Si interface, and was attributed to two intrinsic defects of the silicon lattice: First, stretched Si-Si bonds between surface atoms lead to an Urbach-tail like broadening of the c-Si band edges, similar to the situation in the a-Si:H bulk. Second, dangling bond orbitals of c-Si surface atoms form an almost constant distribution of states throughout the c-Si bandgap, with the symmetry point  $E_0$  between donor-like ( $\delta^+ \leftrightarrow \delta^0$ ) states and acceptor-like ( $\delta^0 \leftrightarrow \delta^-$ ) states at 40 meV below midgap. High dangling bond densities at the interface lead to the pinning of the Fermi level at  $E_F = E_0$ . The broadening of the dangling bond states is due to the statistical disorder in the bond angles and distances of the dangling bond atoms to their nearest neighbors [94].

The band tail states are related to binding electron pairs between the silicon sur-

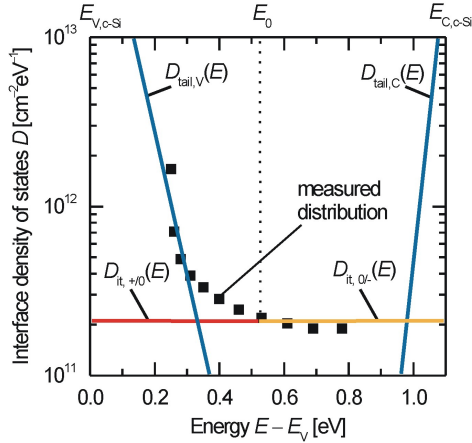


Figure 5.4: *Density of defect states at the a-Si:H/c-Si interface. Sketch after [94, 119], experimental data from Reference [119]. Thanks to Dr. Karsten v. Maydell (HMI, Berlin) for the data.*

face atoms. It was therefore concluded that the recombination activity of the band tail states is negligible [94], just as it is the case in the a-Si:H bulk. Reference [120] shows that the measured recombination velocities at the SiO<sub>2</sub>/c-Si interface can be well fitted by using an energy-independent defect distribution that represents the dangling bond interface states, and by using energy-independent mean carrier capture cross sections.

Only silicon atoms are involved in the formation of the intrinsic interface defects that are described in Reference [94] for the SiO<sub>2</sub>/c-Si interface. The a-Si:H/c-Si interface density of states is therefore attributed to the same defects, which leads the following conclusions:

- There are two types of intrinsic defects at the a-Si:H/c-Si interface, which are band tail states and dangling bond states.
- Carrier recombination through the almost energy-independent distribution of dangling bond states near midgap dominates the interface recombination rate, while the recombination through the band tail states is negligible.
- The distribution function of the recombination-active defect states at the



a-Si:H/c-Si interface is therefore modeled by an energy-independent distribution function representing the dangling bond interface states, with energy-independent mean carrier capture cross sections.

### Model of the a-Si:H/c-Si interface dangling bond distribution

The distribution function of the dangling bond defects at the a-Si:H/c-Si interface to be used in this work is therefore:

$$\begin{aligned} D_{\text{it},+/0}(E) &= \frac{D_{\text{it}}}{E_0 - E_V} [\Theta(E - E_V) \times \Theta(E_0 - E)], \delta^+ \leftrightarrow \delta^0 \text{ transition} \\ D_{\text{it},0/-}(E) &= \frac{D_{\text{it}}}{E_C - E_0} [\Theta(E - E_0) \times \Theta(E_C - E)], \delta^0 \leftrightarrow \delta^- \text{ transition}, \end{aligned} \quad (5.7)$$

where  $\Theta(E)$  is the Heaviside step function, and  $E_0 = (E_{V,c-Si} + 0.5E_{g,c-Si}) - 40 \text{ meV}$  is the symmetry point. The total density of dangling bonds at the interface is denoted by  $D_{\text{it}}$  (in  $\text{cm}^{-2}$ ).

### 5.3.2 Carrier capture cross sections

The main type of defects at the a-Si:H/c-Si interface are dangling bond states, just as in the case of the a-Si:H bulk. The allocation of capture cross sections to the four possible transitions of the amphoteric dangling bonds which is shown in Section 5.2.2, applies also to the interface states. It is concluded in Section 4.2.3, that the capture cross sections of the interface defects are of the same order of magnitude for electrons and holes. They are assumed to be the same within the model that is derived in this section, which reduces the number of free parameters from four to two:

$$\begin{aligned} \sigma_{+/0,n} = \sigma_{0/-,p} &:= \sigma_{\text{charged}}, \text{ and} \\ \sigma_{+/0,p} = \sigma_{0/-,n} &:= \sigma_{\text{non-charged}}. \end{aligned} \quad (5.8)$$

It is obvious that the capture cross sections of the charged states are larger than those of the neutral states due to the Coulomb attraction of the charge carriers, just as it is the case for the dangling bond states in the a-Si:H bulk.

Table 5.3: Capture cross sections  $\sigma_n$  for electrons and  $\sigma_p$  for holes of the dangling bond states at the a-Si:H/c-Si interface.

Interface defect	$\sigma_n$	$\sigma_p$
Dangling bond ( $\delta^+ \leftrightarrow \delta^0$ )	$\sigma_{\text{charged}}$	$\sigma_{\text{non-charged}}$
Dangling bond ( $\delta^0 \leftrightarrow \delta^-$ )	$\sigma_{\text{non-charged}}$	$\sigma_{\text{charged}}$

Table 5.3 shows the allocation of the capture cross sections to the dangling bond defects. The capture cross section of the charged states is fixed,  $\sigma_{\text{charged}} = 1 \times 10^{-14} \text{ cm}^{-2}$ , for the calculations of the interface carrier recombination rate that are performed in this work. Therefore, the ratio  $\sigma_{\text{charged}}/\sigma_{\text{non-charged}}$  is left as the only free parameter for the capture cross sections of the dangling bond interface states. To keep  $\sigma_{\text{charged}}$  at a predefined value is no restriction to the generality of this model, because the recombination rate depends only on the product of the two fit parameters, capture cross section and defect density, as shown in the Equations 2.12–2.14.  $\sigma_{\text{charged}} = 1 \times 10^{-14} \text{ cm}^{-2}$  is a reasonable value that was also found for the recombination at the  $\text{SiO}_2/\text{c-Si}$  interface [120].

The ratio of the capture cross sections of charged and non-charged interface states,  $\sigma_{\text{charged}}/\sigma_{\text{non-charged}}$ , and the total defect density  $D_{\text{it}}$  are then the only free interface parameters of the defect model derived in this chapter.

## 6 Stability under illumination: Staebler-Wronski effect

The stability of the a-Si:H- and a-Si:H/SiN<sub>x</sub>-passivation during illumination is important to ensure the long-term stability of a-Si:H passivated solar cells.

Amorphous silicon solar cells show a decrease of the dark- and photo-conductivity during illumination, which is fully reversible by annealing. This effect is named Staebler-Wronski effect after its discoverers and was found to be due to the light-induced formation of recombination centers in the a-Si:H bulk [121, 122, 123]. There are several mechanisms proposed for the formation of these defects. The common effect is the light-induced dissociation of Si-Si bonds that are stretched when compared to the c-Si binding length, and are thus “weak”. The dissociation of a weak Si-Si bond corresponds to the formation of two dangling bonds that act as recombination centers. The density of newly created recombination centers saturates after a certain illumination time that depends on the illumination intensity [110]. During annealing, the Si-Si bonds re-form or get passivated by hydrogen.

The same kind of effect is observed for the a-Si:H-passivated c-Si surface in this work. Illumination leads to a slight degradation of the surface passivation quality, which is fully reversible by annealing.

Section 6.1 shows the stability of the a-Si:H single-layer passivation, and of the a-Si:H/SiN<sub>x</sub> double-layers passivation under various illumination conditions. In Section 6.2, the defect model derived in Chapter 5 is used to determine the capture cross section of the dangling bond states at the a-Si:H/c-Si interface. The densities of light-induced defect states in the a-Si:H bulk, and at the a-Si:H/c-Si interface, are deduced from the effective carrier lifetimes of the samples after illumination.

### 6.1 Experimental

The single- and double-layer passivated samples with  $d = 10$  nm that are shown in Section 4.1 are used to assess the effective surface recombination velocity at several stages of illumination of each wafer side by a halogen lamp with the in-

tensity  $50 \text{ mW/cm}^2$ , and after illumination under indoor conditions, i. e. combined sunlight and fluorescent light. In addition to those samples,  $300 \mu\text{m}$  thick  $n$ -type  $1.5 \Omega\text{cm}$  FZ-Si wafers are passivated by  $10 \text{ nm}$  of a-Si:H on both sides. The surface orientation of the wafers is (100).

### 6.1.1 A-Si:H single layer passivation

#### p-type c-Si substrate

Figure 6.1a shows the injection-dependent carrier lifetime  $\tau_{\text{eff}}$  of the a-Si:H passivated  $p$ -type wafers in the as-deposited state, after 5 h illumination of each side under a  $50 \text{ mW/cm}^2$  halogen lamp, and after 3 and 15 months of storage under indoor illumination, i. e. a mixture of fluorescent light and sunlight. The lifetime curve obtained after 5 h of halogen illumination is also reproduced by 70 h of indoor illumination.

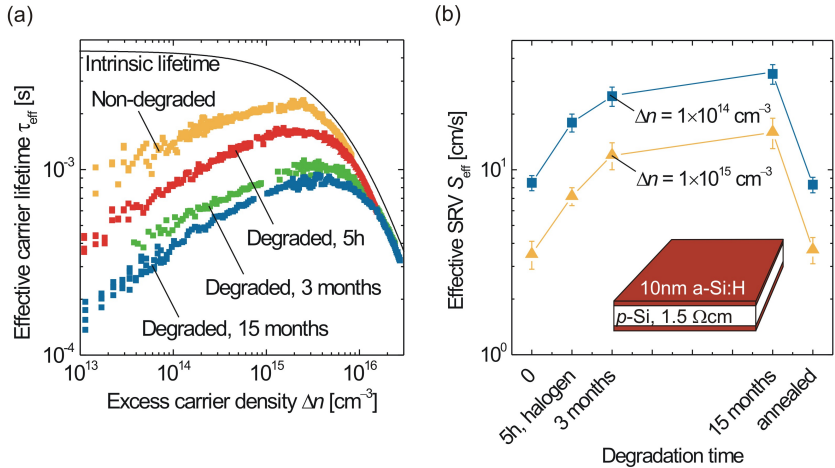


Figure 6.1: (a) Effective carrier lifetime of  $1.5 \Omega\text{cm}$   $p$ -type  $c$ -Si wafers passivated by a-Si:H single layers with  $d = 10 \text{ nm}$ . (b) Effective surface recombination velocities (SRV) at  $\Delta n = 10^{14} \text{ cm}^{-3}$  and  $\Delta n = 10^{15} \text{ cm}^{-3}$ . The samples are measured in the as-deposited state, after  $50 \text{ mW/cm}^2$  illumination by a halogen lamp for 5 h per side, and after 3 and 15 months storage under indoor illumination. The degradation is fully reversible by annealing at  $300^\circ\text{C}$  for 5 min.

Figure 6.1b shows the effective surface recombination velocities  $S_{\text{eff}}$  as calculated from  $\tau_{\text{eff}}$  at  $\Delta n = 10^{14} \text{ cm}^{-3}$  and  $\Delta n = 10^{15} \text{ cm}^{-3}$ . The surface recombination velocity saturates to a constant value with increasing degradation time. After 15 months,  $S_{\text{eff}} = (35 \pm 5) \text{ cm/s}$  at  $\Delta n = 10^{14} \text{ cm}^{-3}$ , and  $S_{\text{eff}} = (14 \pm 5) \text{ cm/s}$  at  $\Delta n = 10^{15} \text{ cm}^{-3}$ , which is about a factor of 5 higher than the initial values of  $S_{\text{eff}} = (8.5 \pm 0.8) \text{ cm/s}$  and  $S_{\text{eff}} = (3.5 \pm 0.6) \text{ cm/s}$ , respectively. However, the passivation quality is still in the range (4...20) cm/s that was reported for c-Si surfaces that were passivated by PECVD-SiN<sub>x</sub> optimized for surface passivation [65].

Annealing of the samples at 300°C for 5 min on a hotplate fully restores  $S_{\text{eff}}$  to the initial values of below 10 cm/s, and also maintains the injection-dependence of the effective carrier lifetime. Storage in the dark for 3 weeks after annealing maintains the high surface passivation quality (not shown in Figure 6.1). Subsequent illumination again leads to the degradation shown in Figure 6.1. The illumination-induced degradation of the a-Si:H/c-Si interface passivation is therefore fully reversible by annealing, like the Staebler-Wronski effect in the a-Si:H bulk.

### n-type c-Si substrate

Figure 6.2a shows the injection-dependent carrier lifetime  $\tau_{\text{eff}}$  of the a-Si:H passivated *n*-type wafers in the as-deposited state, and after 5 h illumination of each side under a 50 mW/cm<sup>2</sup> halogen lamp. The illumination conditions are the same as for the *p*-type wafer, so that both types of samples can be compared at a defined level of the light-induced degradation. Figure 6.1b shows the effective surface recombination velocity  $S_{\text{eff}}$ , as a function of  $\Delta n$ .

The surface recombination velocity at  $\Delta n = 10^{15} \text{ cm}^{-3}$  is  $S_{\text{eff}} = (3.0 \pm 0.5) \text{ cm/s}$  in the non-degraded state after the deposition, and increases to  $(5.0 \pm 0.5) \text{ cm/s}$  after illumination by the halogen lamp for 5 h. This is roughly the same relative increase of the SRV as for the *p*-type wafer, where the SRV increases from  $S_{\text{eff}} = (3.5 \pm 0.5) \text{ cm/s}$  in the non-degraded state after to  $(7.2 \pm 0.5) \text{ cm/s}$  after 5 h of halogen lamp illumination.

### 6.1.2 A-Si:H/SiN<sub>x</sub> double layer passivation

Figure 6.3 shows the effective carrier lifetime of the a-Si:H/SiN<sub>x</sub> passivated *p*-type samples with  $d = 10 \text{ nm}$ , measured by QSSPC immediately after the deposition and after 15 months of storage. The a-Si:H passivation layer is capped by a 60 nm thick SiN<sub>x</sub> layer deposited at 230°C, as described in Section 3.1. The refractive index of the SiN<sub>x</sub> layer is  $n = 2.05$ . The corresponding lifetime curves of the a-Si:H single-layer passivated wafers of Figure 6.1 are shown for comparison.

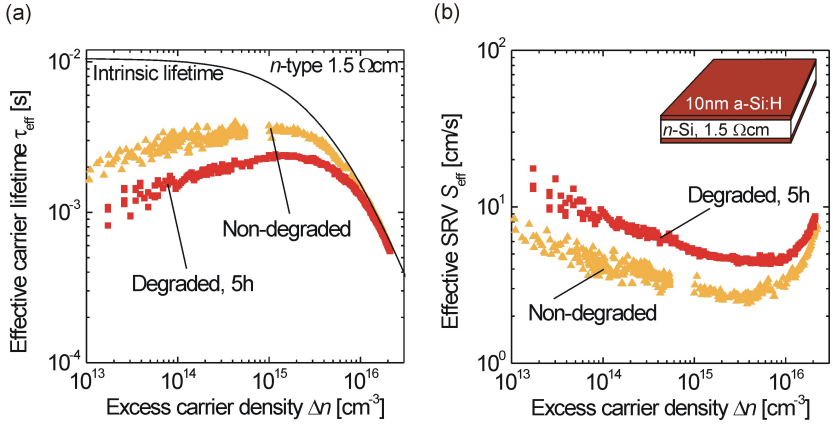


Figure 6.2: (a) Effective carrier lifetime of a 1.5 Ωcm n-type c-Si wafer that is passivated by 10 nm of a-Si:H. (b) Effective surface recombination velocities of the same samples. The wafer is measured in the as-deposited state (non-degraded), and after 5 h illumination of each side by a halogen lamp. The illumination intensity during the light-induced degradation is 50 mW/cm<sup>2</sup>.

There is no discernible difference in the injection-dependent effective carrier lifetimes of the samples that are passivated with a-Si:H/SiN<sub>x</sub> double layers, and the samples that are passivated with a-Si:H single layers, within the uncertainty interval of the lifetime measurement. Both kinds of passivation layers show the same degradation under illumination. Therefore, the application of the SiN<sub>x</sub> capping layer has no influence on the injection-dependence of the a-Si:H passivation, and on its stability during illumination.

### 6.1.3 Discussion

The observed slight degradation of the surface passivation by a-Si:H is found to be light-induced, and is fully reversible by annealing at 300°C as shown in Figure 6.1b. It therefore shows the same behavior under illumination and annealing as the Staebler-Wronski effect that is known to occur in the a-Si:H bulk. The light-induced dissociation of weak Si-Si bonds and of Si-H bonds forms recombination centers. Therefore, the carrier recombination rate increases. Within the uncertainty interval of the lifetime measurement, the observed effect is not influenced by the application

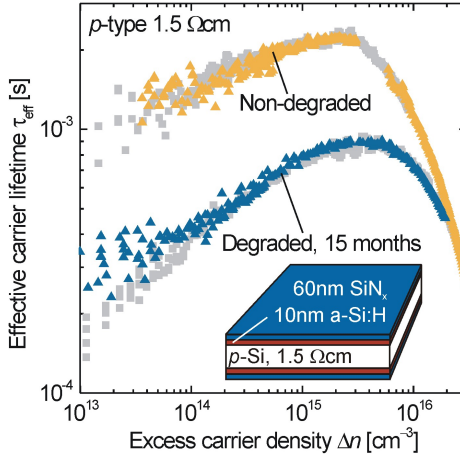


Figure 6.3: Effective carrier lifetime  $\tau_{\text{eff}}$  of 1.5  $\Omega\text{cm}$  *p*-type *c*-Si wafers passivated by *a*-Si:H/SiN<sub>x</sub> double layers (orange/blue triangles), as a function of the excess carrier density  $\Delta n$ . The *a*-Si:H layer is 10 nm thick. The samples were measured in the non-degraded state immediately after the deposition, and after 15 months storage under indoor illumination. The corresponding curves of the *a*-Si:H single layer passivated samples shown in Figure 6.1 are included for comparison (gray squares).

of the SiN<sub>x</sub> capping layer, and it is not influenced by the type of doping of the substrate wafer.

The effective surface recombination velocity is found to saturate around  $S_{\text{eff}} = 20$  cm/s after 15 months of illumination in the case of the *p*-type *c*-Si wafer. The passivation quality after degradation is still in the range (4... 20) cm/s that was reported for *c*-Si surfaces that were passivated by PECVD-SiN<sub>x</sub> optimized for surface passivation [65]. According to Reference [67], the increase of  $S_{\text{eff}}$  during the annealing hardly decreases the efficiency potential of solar cells, when the *a*-Si:H layer is used to passivate the base surface. The light-induced increase of the surface recombination velocity is therefore no obstacle for the application of the *a*-Si:H surface passivation to solar cells.

## 6.2 Formation of defects during illumination

The injection-dependent carrier lifetimes of the a-Si:H single layer passivated wafers at various stages of illumination, which are shown in Section 6.1.1, are used to assess the carrier capture cross sections of the defect states at the a-Si:H/c-Si interface. The densities of the illumination-induced dangling bond states in the a-Si:H bulk, and at the a-Si:H/c-Si interface are determined.

### 6.2.1 Prerequisites

The model of the dangling bond distribution functions in the a-Si:H bulk and at the a-Si:H/c-Si interface is described by the Equations 5.2, 5.5, and 5.7. It leaves three free parameters: The total dangling bond densities in the a-Si:H bulk and at the a-Si:H/c-Si interface,  $N_{\text{DB}}$  and  $D_{\text{it}}$ , which are subject to the illumination intensity and time, and the ratio  $\sigma_{\text{charged}}/\sigma_{\text{non-charged}}$  of the capture cross sections of the charged and the non-charged dangling bond states at the interface, which is determined by the physical nature of the defects and does therefore *not* change during illumination.

Five independent measurements are used to determine these three parameters: The injection-dependent effective carrier lifetimes of the a-Si:H-passivated *p*-type and *n*-type FZ-Si wafers in the as-deposited state, after 5 h and after 15 months of illumination, which are shown in Section 6.1.1, and also in Figure 6.4.

The software package AFORS-HET is used to fit the injection-dependent effective carrier lifetime of the a-Si:H-passivated wafers, as described in Section 5.1. The defect model derived in Section 5.2 is implemented in the calculations to simulate the carrier recombination through the a-Si:H/c-Si interface defects and through the a-Si:H bulk defects. The spectrum of the illumination is the same in the simulation, as in the experiment. The calculated lifetime is then compared to the effective carrier lifetime obtained from the QSSPC measurements in order to adjust the parameters  $N_{\text{DB}}$ ,  $D_{\text{it}}$ , and  $\sigma_{\text{charged}}/\sigma_{\text{non-charged}}$  to obtain the best fit to the experimental data of Section 6.1.1.

The capture cross sections of the interface states are assumed to be invariant under variations of the defect densities, because they are only determined by the physical nature of the defect. Therefore, all measured lifetime curves are fitted with the same ratio of the capture cross sections  $\sigma_{\text{charged}}/\sigma_{\text{non-charged}}$  of the dangling bond defects at the a-Si:H/c-Si interface.

The densities of the interface defects and of the a-Si:H bulk defects are assumed to be independent of the doping type and concentration of the substrate, but to depend only on the deposition parameters and on the post-deposition treatment of the samples. Therefore, one set  $N_{\text{DB,non-deg}}$ ,  $D_{\text{it,non-deg}}$  is found that fits the non-degraded curves, another set  $N_{\text{DB,5h}}$ ,  $D_{\text{it,5h}}$  that fits the light-degraded curves after



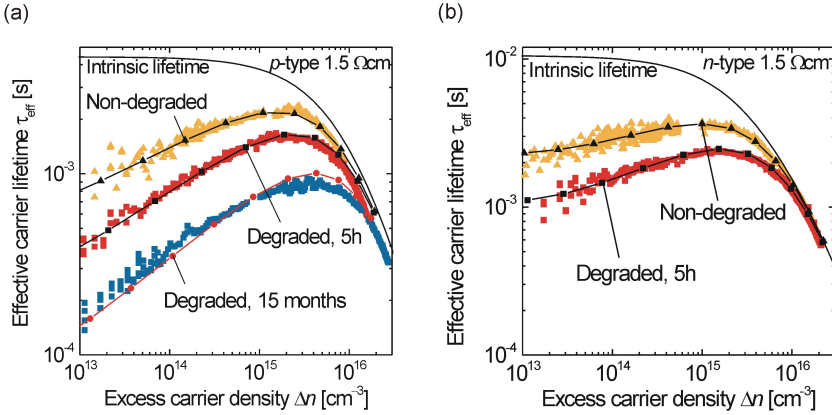


Figure 6.4: Effective carrier lifetime  $\tau_{\text{eff}}$  of (a) p-type silicon and (b) n-type silicon wafers passivated on both sides by 10 nm of a-Si:H. The symbols denote the lifetimes calculated from QSSPC measurements. The lines denote the best fits with the defect model shown in Chapter 5, with the parameters shown in Table 6.1.

5 h of illumination, and a third set  $N_{\text{DB},15\text{m}}$ ,  $D_{\text{it},15\text{m}}$  that fits the light-degraded curves after 15 months of illumination.

## 6.2.2 Results and discussion

Figure 6.4 shows the graphs of the best fits to the measured effective carrier lifetimes. The fitted values and the uncertainty intervals of the dangling bond densities and the capture cross section ratio are given in Table 6.1.

### Formation of dangling bonds during illumination

The dangling bond densities in the non-degraded state are  $N_{\text{DB}} \leq 1 \times 10^{18} \text{ cm}^{-3}$  in the a-Si:H bulk, and  $D_{\text{it}} = (5 \pm 5) \times 10^8 \text{ cm}^{-2}$  at the interface. The best fit to the non-degraded lifetime curves is obtained with the a-Si:H bulk density of dangling bonds being  $N_{\text{DB}} = 8 \times 10^{17} \text{ cm}^{-3}$ , and the interface dangling bond density  $D_{\text{it}} = 5 \times 10^8 \text{ cm}^{-2}$ . The interface defect density is in the same range as it was found for the interface between silicon-rich SiN<sub>x</sub> and c-Si [19].

The density of the interface defects  $D_{\text{it}}$  increases by a factor of about 2 during the first 5 h of 50 mW/cm<sup>2</sup> illumination by the halogen lamp, while the density

Table 6.1: *Parameters of the a-Si:H/c-Si defect model that are obtained from fitting the injection-dependent effective carrier lifetime of the a-Si:H passivated 1.5  $\Omega\text{cm}$  p- and n-type wafers in Figure 6.4. The capture cross section of the charged interface defects is fixed at  $\sigma_{\text{charged}} = 10^{-14} \text{ cm}^{-3}$ , which is a common value for the  $\text{SiO}_2/\text{c-Si}$  interface.*

	Parameter	Best fit	Uncertainty interval
All cases	$\frac{\sigma_{\text{charged}}}{\sigma_{\text{non-charged}}}$	$2 \times 10^3$	$\pm 1 \times 10^3$
Non-degraded	$N_{\text{DB}}$	$8 \times 10^{17} \text{ cm}^{-3}$	$\leq 1 \times 10^{18} \text{ cm}^{-3}$
	$D_{\text{it}}$	$5 \times 10^8 \text{ cm}^{-2}$	$\pm 5 \times 10^8 \text{ cm}^{-2}$
Degraded, 5 h	$N_{\text{DB}}$	$3 \times 10^{18} \text{ cm}^{-3}$	$\leq 1 \times 10^{19} \text{ cm}^{-3}$
	$D_{\text{it}}$	$1 \times 10^9 \text{ cm}^{-2}$	$\pm 5 \times 10^8 \text{ cm}^{-2}$
Degraded, 15 months	$N_{\text{DB}}$	$1 \times 10^{19} \text{ cm}^{-3}$	$\leq 5 \times 10^{19} \text{ cm}^{-3}$
	$D_{\text{it}}$	$4 \times 10^9 \text{ cm}^{-2}$	$\pm 2 \times 10^9 \text{ cm}^{-2}$

of the dangling bonds  $N_{\text{DB}}$  in the a-Si:H bulk increases by a factor of about 4. Therefore, the dangling Si bonds in the a-Si:H bulk form at a higher rate during annealing than the interface dangling bonds.

During the illumination, both defect densities increase by about one order of magnitude from the non-degraded state to the degraded state after 15 months. This is in good agreement with the relative increase by a factor of 10 due to the Staebler-Wronski effect, that was shown in Reference [124] for the increase of the bulk defect density of a-Si:H from the non-degraded state, to the light-soaked equilibrium state. It is therefore concluded that the p-type sample shown in Figure 6.4a is in its stable state after 15 months storage.

The experimental data are explained best by assuming that the reason for the reversible light-degradation of the a-Si:H surface passivation is a Staebler-Wronski-like formation of dangling bond states [121]. As weak Si-Si bonds exist both, in the a-Si:H bulk, and at the a-Si:H/c-Si interface, it is to be expected that the light-induced dissociation of those weak bonds occurs both, in the a-Si:H bulk, and at the interface.

### Carrier capture cross sections of the interface defects

By fitting all five curves in Figure 6.4 *simultaneously*, the ratio of the capture cross sections of the interface states  $\sigma_{\text{charged}}/\sigma_{\text{non-charged}} = (2 \pm 1) \times 10^3$  is found. This is in good agreement to the results  $\sigma_{\text{charged}}/\sigma_{\text{non-charged}} = 10^2 \dots 10^4$  that were obtained for both, the intrinsic dangling bond defects at the SiO<sub>2</sub>/c-Si interface [120], and the dangling bond defects at the a-Si:H/c-Si interface [109].

Figure 6.5a shows the simulated effective carrier lifetime of the a-Si:H passivated *n*-type wafer in the non-degraded state. The defect densities  $N_{\text{DB}} = 8 \times 10^{17} \text{ cm}^{-3}$  and  $D_{\text{it}} = 5 \times 10^8 \text{ cm}^{-2}$  are fixed, while the ratio of the capture cross sections is varied,  $\sigma_{\text{charged}}/\sigma_{\text{non-charged}} = 2000, 200, \text{ and } 1$ .

The *lli* carrier lifetime strongly depends on  $\sigma_{\text{charged}}/\sigma_{\text{non-charged}}$ , which allows for the rather accurate determination of the interface capture cross section ratio. The ( $\delta^+ \leftrightarrow \delta^0$ ) interface states in the lower half of the bandgap are populated by electrons in *lli* conditions, while the ( $\delta^0 \leftrightarrow \delta^-$ ) states in the upper half are mostly unpopulated. The recombination rate is therefore limited by the capture rate of the minority carriers (holes) in the ( $\delta^+ \leftrightarrow \delta^0$ ) states, which is determined by the smaller one of the interface capture cross sections,  $\sigma_{\text{non-charged}}$ .

### Carrier recombination in the a-Si:H bulk

Figure 6.5b shows again the non-degraded effective carrier lifetimes of the a-Si:H passivated *n*-type wafer. In order to simulate the impact of the interface defect density  $D_{\text{it}}$  on the effective carrier lifetime of the sample, lifetime curves are calculated with the a-Si:H bulk density of states and the ratio of the capture cross sections being fixed to the values that allow for the best fit to the experimental data,  $N_{\text{DB}} = 8 \times 10^{17} \text{ cm}^{-3}$  and  $\sigma_{\text{charged}}/\sigma_{\text{non-charged}} = 2000$ . The interface density of states  $D_{\text{it}}$  is varied from  $5 \times 10^8 \text{ cm}^{-2}$  to  $2 \times 10^9 \text{ cm}^{-2}$ . The effective surface recombination velocity  $S_{\text{lli}}$  in *lli* conditions is calculated from the effective lifetime at an excess carrier concentration of  $\Delta n = 1 \times 10^{10} \text{ cm}^{-3}$  by Equation 2.22.

Figure 6.5c shows a variation of the a-Si:H bulk density of states  $N_{\text{DB}}$ . Lifetime curves are calculated with the interface density of states and the ratio of the capture cross sections being fixed to  $D_{\text{it}} = 5 \times 10^8 \text{ cm}^{-2}$  and  $\sigma_{\text{charged}}/\sigma_{\text{non-charged}} = 2000$ . The a-Si:H bulk density of states  $N_{\text{DB}}$  is varied from  $1 \times 10^{16} \text{ cm}^{-3}$  to  $1 \times 10^{19} \text{ cm}^{-3}$ . A bulk density of states of  $N_{\text{DB}} = (1 \dots 10) \times 10^{16} \text{ cm}^{-3}$  is typically reported for amorphous silicon that is optimized for the fabrication of amorphous solar cells, where an optimum electronic quality of the a-Si:H bulk is necessary [110].

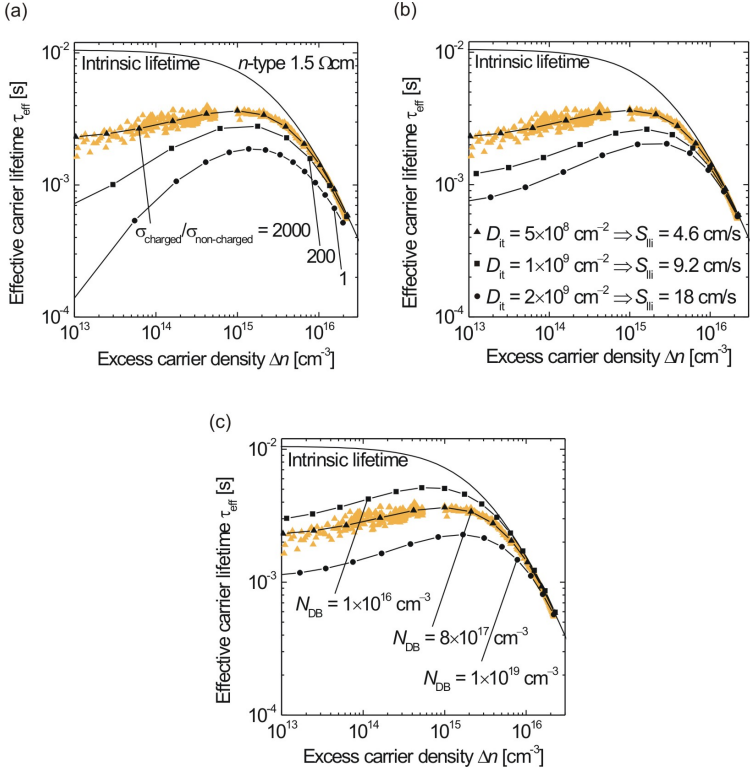


Figure 6.5: *Effective carrier lifetime of the a-Si:H-passivated n-type wafer, in the non-degrade state. The symbols denote the carrier lifetime measured by QSSPC. The lines denote the lifetimes simulated by AFORS-HET. (a) The defect densities  $N_{DB} = 8 \times 10^{17} \text{ cm}^{-3}$ , and  $D_{it} = 1 \times 10^9 \text{ cm}^{-2}$  are fixed. The ratio of the interface capture cross sections is varied,  $\sigma_{\text{charged}}/\sigma_{\text{non-charged}} = 2000, 200,$  and  $1$ . (b) The a-Si:H bulk defect density  $N_{DB} = 8 \times 10^{17} \text{ cm}^{-3}$  and the capture cross section ratio  $\sigma_{\text{charged}}/\sigma_{\text{non-charged}} = 2000$  are fixed. The interface density of dangling bonds is varied,  $D_{it} = (5 \dots 20) \times 10^8 \text{ cm}^{-2}$ . (c) The interface defect density  $D_{it} = 5 \times 10^8 \text{ cm}^{-2}$  and the capture cross section ratio  $\sigma_{\text{charged}}/\sigma_{\text{non-charged}} = 2000$  are fixed. The a-Si:H bulk density of dangling bonds is varied,  $N_{DB} = (10^{16} \dots 10^{19}) \text{ cm}^{-3}$ .*

Equation 2.12 states that the carrier recombination rate that is associated to the recombination through defect states by the Shockley-Read-Hall formalism, is proportional to the defect density. This correlation is fulfilled for the density of the interface dangling bonds, as shown in Figure 6.5b: Increasing the dangling bond density at the a-Si:H/c-Si interface by a factor of 2 (4) leads to a decrease of the effective surface recombination velocity  $S_{\text{li}}$  by also also a factor of 2 (4). Since the effective carrier recombination rate is proportional to the effective SRV,  $U_{\text{li}} = \Delta n S_{\text{li}}$  after Equation 2.17, a decrease of the effective SRV means a decrease of the effective carrier recombination rate by the same factor.

However, Figure 6.5c shows that increasing the dangling bond density in the a-Si:H bulk by three orders of magnitude leads to a much smaller increase of the effective carrier recombination rate: The effective carrier lifetime at the excess carrier density  $\Delta n = 1 \times 10^{13} \text{ cm}^{-3}$  is  $\tau_{\text{eff}} = 3.0 \text{ ms}$  for  $N_{\text{DB}} = 1 \times 10^{16} \text{ cm}^{-3}$ , and decreases by a factor of 2.5 to  $\tau_{\text{eff}} = 1.2 \text{ ms}$  for  $N_{\text{DB}} = 1 \times 10^{19} \text{ cm}^{-3}$ .

Figure 6.6 shows the calculated energy band diagrams, and depth profiles of the recombination rate  $U(z)$  for a 10 nm thick a-Si:H layer on a  $1.5 \Omega \text{ cm}$   $n$ -type wafer, as a function of the distance  $z$  from the a-Si:H surface. The parameters used for the calculations are the same as for the calculation of the effective carrier lifetime shown in Figure 6.5c: The density of dangling bonds is varied,  $N_{\text{DB}} = 1 \times 10^{16} \text{ cm}^{-3}$  for the results shown in Figure 6.6a, and  $N_{\text{DB}} = 1 \times 10^{19} \text{ cm}^{-3}$  for Figure 6.6b. The interface density of states  $D_{\text{it}} = 5 \times 10^8 \text{ cm}^{-2}$  and the excess carrier concentration  $\Delta n = 1 \times 10^{13} \text{ cm}^{-3}$  are the same in both cases. The illuminating spectrum contains only wavelengths  $\lambda > 800 \text{ nm}$ . Light-induced carrier generation within the a-Si:H film is therefore negligible, which means that only excess carriers that cross the a-Si:H/c-Si heterojunction will recombine within the a-Si:H layer.

The total recombination rates within the a-Si:H layer,  $U_{\text{s,a-Si:H}}$ , and in the interface region  $U_{\text{s,it}}$ , are obtained by integrating the local recombination rate over the respective layer width,

$$U_{\text{s,layer}} = \int_{\text{layer}} U(z) dz. \quad (6.1)$$

The corresponding specific recombination velocities of the a-Si:H layer and the interface layer are defined by Equation 2.17,  $S_{\text{layer}} = U_{\text{s,layer}}/\Delta n$ .

Figure 6.6a shows that for a low dangling bond density  $N_{\text{DB}} = 1 \times 10^{16} \text{ cm}^{-3}$  of the a-Si:H bulk, the carrier recombination rate within the a-Si:H layer is negligible when compared to the total recombination rate in the interface region,  $U_{\text{s,a-Si:H}} \ll U_{\text{s,it}}$ .

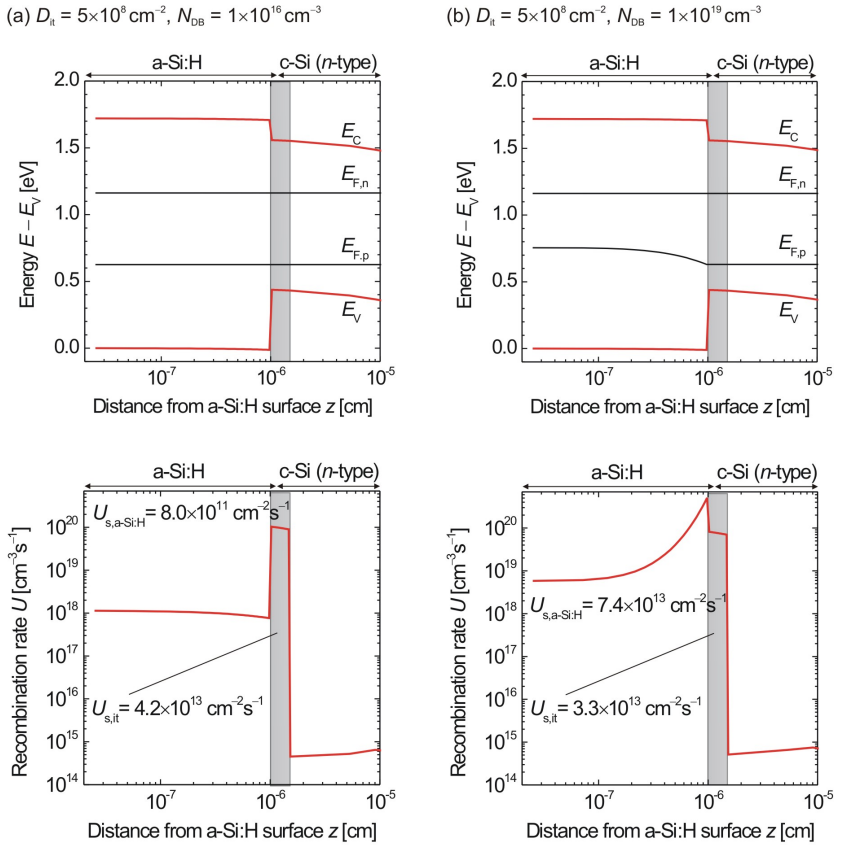


Figure 6.6: Calculated band diagrams and depth profiles of the recombination rate  $U$ , for a 10 nm thick a-Si:H layer on a 1.5  $\Omega\text{cm}$  n-type wafer, under infrared illumination with  $800 \text{ nm} < \lambda < 1100 \text{ nm}$ . The excess carrier density is  $\Delta n = 1 \times 10^{13} \text{ cm}^{-3}$ . The shaded area denotes the interface region. (a) Calculation for  $N_{DB} = 1 \times 10^{16} \text{ cm}^{-3}$ . (b) Calculation for  $N_{DB} = 1 \times 10^{19} \text{ cm}^{-3}$ . The increased a-Si:H bulk defect density leads to an increase of the total recombination rate by a factor of 2.5.

However, increasing the a-Si:H bulk density of states by three orders of magnitude to  $N_{\text{DB}} = 1 \times 10^{19} \text{ cm}^{-3}$  leads to an increase of the carrier recombination rate by only about two orders, from  $U_{\text{s,a-Si:H}} = 8.0 \times 10^{11} \text{ cm}^{-2}\text{s}^{-1}$  to  $7.4 \times 10^{13} \text{ cm}^{-2}\text{s}^{-1}$ . This value of  $U_{\text{s,a-Si:H}}$  is in the same range as the total recombination rate in the interface region  $U_{\text{s}} = 3.3 \times 10^{13} \text{ cm}^{-2}\text{s}^{-1}$  as shown in Figure 6.6b. The splitting of the quasi-Fermi levels  $E_{\text{F,n}} - E_{\text{F,p}}$  is reduced by 125 meV due to the increased carrier recombination in the a-Si:H bulk.

The total surface recombination rate  $U_{\text{s}} = U_{\text{s,a-Si:H}} + U_{\text{s,it}}$  therefore increases by a factor of 2.5 from  $U_{\text{s}} = 4.2 \times 10^{13} \text{ cm}^{-2}\text{s}^{-1}$  for  $N_{\text{DB}} = 1 \times 10^{16} \text{ cm}^{-3}$ , to  $U_{\text{s}} = 10.7 \times 10^{13} \text{ cm}^{-2}\text{s}^{-1}$  for  $N_{\text{DB}} = 1 \times 10^{19} \text{ cm}^{-3}$ , which agrees with the increase of  $S_{\text{eff}}$  as obtained from the effective carrier lifetime curves shown in Figure 6.5c. This increase is due to the increased carrier recombination rate within the a-Si:H bulk.

It is obvious from comparing the impact of the magnitude of the dangling bond densities  $N_{\text{DB}}$  and  $D_{\text{it}}$ , that

- The effective carrier recombination rate of the a-Si:H-passivated c-Si surface is determined by the density of the interface defects  $D_{\text{it}}$ , as long as the a-Si:H bulk density of states is within a range  $N_{\text{DB}} = (10^{16} \dots 10^{17}) \text{ cm}^{-3}$  that was reported in Reference [110] for a-Si:H layers with optimized bulk quality. As the dangling bond density of the a-Si:H bulk is higher,  $N_{\text{DB}} > 10^{18} \text{ cm}^{-3}$  for the layers that are prepared in this work, carrier recombination through both the defect states at the a-Si:H/c-Si interface and in the a-Si:H bulk contributes to the total surface recombination rate.
- However, the carrier recombination rate within the a-Si:H layer is not only limited by the concentration of defects, as is obvious from the only sub-linear increase of the recombination rate  $U_{\text{s,a-Si:H}}$  with increasing dangling bond density  $N_{\text{DB}}$ . This is due to the band edge offsets of  $\Delta E_{\text{V}} = 450 \text{ eV}$  and  $\Delta E_{\text{C}} = 150 \text{ eV}$  shown in Figure 5.3, which are considerably larger than the thermal energy of a charge carrier at room temperature,  $kT = 25.8 \text{ meV}$ . Therefore, transport of excess carriers from the crystalline silicon into the amorphous silicon layer is effectively blocked, and relatively high defect densities are allowed in the a-Si:H bulk without destroying the excellent surface passivation.

### 6.3 Summary

A slight increase of the effective surface recombination velocity of a-Si:H-passivated c-Si wafers is observed during illumination. The increase of the SRV is fully re-

versible by annealing at 300°C for 5 min, and does not occur during storage of the samples in the dark. The effective surface recombination velocity is found to saturate around  $S_{\text{eff}} = 20$  cm/s after 15 months of illumination in the case of the  $p$ -type c-Si wafer, which is in the same range as the effective SRV of SiN<sub>x</sub>-passivated c-Si wafers.

Fitting the defect model derived in Section 5.2 to the experimental data shows that both, the density of the interface dangling bonds and the density of the dangling bonds in the a-Si:H bulk, increase by an order of magnitude during the 15 months of illumination. The ratio of the capture cross sections of the interface dangling bonds is  $\sigma_{\text{charged}}/\sigma_{\text{non-charged}} = (2 \pm 1) \times 10^3$ . The capture cross sections for electrons and for holes are the same within the defect model that is used in this work. The effective surface recombination rate is controlled by both, carrier recombination through interface defects and recombination through a-Si:H bulk defects.

The experimental data are explained best by assuming that the reversible light-degradation of the a-Si:H surface passivation is due to the formation of dangling bond states both, at the a-Si:H/c-Si interface and in the a-Si:H bulk, analogue to the well-known Staebler-Wronski effect of the dissociation of weak Si-Si bonds [121]. The abundance of weak bonds and also the rate at which the light-induced recombination centers form is proposed to depend on the bond configuration of the involved atoms, which is different at the interface and in the a-Si:H bulk. Fitting the recombination model shown in Section 5 to the experimental results, suggests that the illumination-induced defects form at a higher rate in the a-Si:H bulk than at the interface.



## 7 Thermal stability

The thermal stability of the surface passivation is important for technological reasons, as the solar cells are subject to repeated heating during the annealing or firing of metal contacts, and during soldering and lamination of solar cells in modules.

Section 7.1, describes the thermal stability of the passivation of lowly-doped c-Si surfaces by a-Si:H single layers and by a-Si:H/SiN<sub>x</sub> double layers. In Section 7.2, the increase of the density of defect states is quantified by fitting the defect model of Section 5.2 to reproduce the injection-dependent carrier lifetime curves of the annealed a-Si:H-passivated samples. Section 7.3 shows the correlation of the post-deposition annealing temperature and of the a-Si:H layer thickness to the interface density of defects for the diffused emitters that are investigated experimentally in Section 4.2.

### 7.1 Passivation of lowly-doped surfaces

Lifetime samples with a-Si:H single-layer passivation and a-Si:H/SiN<sub>x</sub> double-layer passivation are prepared from polished *p*-type, (100)-oriented, 1.5 Ωcm FZ-Si wafers. The thickness of the a-Si:H layer is  $d = 10$  nm. Thicker a-Si:H layers show a slightly enhanced thermal stability, but form blisters during annealing, due to the desorption of hydrogen from the a-Si:H layer. The samples are annealed on a hotplate, in ambient atmosphere. The effective surface recombination velocity  $S_{\text{eff}}$  is determined from QSSPC measurements after annealing the samples at  $T = (300 \dots 600)^\circ\text{C}$  for  $(1 \dots 30)$  min.

#### 7.1.1 Results

Figure 7.1 shows the effective surface recombination velocity  $S_{\text{eff}}$  at  $\Delta n = 10^{15} \text{ cm}^{-3}$  as a function of the annealing time and temperature. For both types of samples, annealing at  $300^\circ\text{C}$  maintains the excellent surface passivation with  $S_{\text{eff}} = (3.5 \pm 1.0) \text{ cm/s}$  for at least 30 min annealing time.

The effective SRV of the a-Si:H single-layer passivated samples increases for annealing temperatures  $T_{\text{anneal}} \geq 400^\circ\text{C}$ . The surface recombination velocity

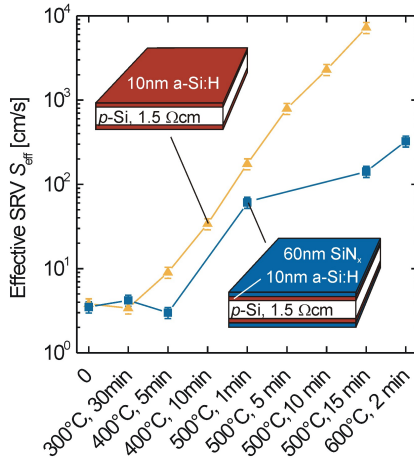


Figure 7.1: *Effective SRV of a-Si:H-passivated wafers and of a-Si:H/SiN<sub>x</sub>-passivated wafers at  $\Delta n = 10^{15} \text{ cm}^{-3}$ , as a function of the annealing temperature and time. The thickness of the a-Si:H layer is 10 nm on all samples. The SiN<sub>x</sub> capping layer enhances the thermal stability.*

is  $S_{\text{eff}} = (175 \pm 25) \text{ cm/s}$  after annealing at  $500^\circ\text{C}$  for 1 min, and increases to  $(7.2 \pm 1) \times 10^3 \text{ cm/s}$  after 5 min at  $500^\circ\text{C}$ .

The a-Si:H/SiN<sub>x</sub>-passivated samples show a stable SRV of  $S_{\text{eff}} = (3 \dots 4) \text{ cm/s}$  for up to 5 min at  $400^\circ\text{C}$ , and an increasing SRV for  $T_{\text{anneal}} \geq 500^\circ\text{C}$ . Annealing of the a-Si:H/SiN<sub>x</sub>-passivated samples at  $500^\circ\text{C}$  for 15 min results in  $S_{\text{eff}} = 140 \text{ cm/s}$ , which is in the same range as the effective SRV of the a-Si:H single layer-passivated samples after annealing for only 1 min.

### 7.1.2 Discussion

The SiN<sub>x</sub> capping layer enhances the thermal stability of the a-Si:H/SiN<sub>x</sub> double layer when compared to the a-Si:H single layer: The effective surface recombination velocity after annealing for 15 min at  $500^\circ\text{C}$  is almost two orders of magnitude lower with the a-Si:H/SiN<sub>x</sub> passivation, than with the a-Si:H single-layer passivation. Equation 2.12 suggests that also the density of the dangling bond states which contribute to the effective carrier recombination rate, is two orders of mag-

nitude lower with the a-Si:H/SiN<sub>x</sub> passivation, than with the a-Si:H single-layer passivation.

Annealing at 300°C maintains the excellent surface passivation of both kinds of samples, which complies with the results of Section 6 that show that annealing at 300°C even reverses the light-induced degradation of  $S_{\text{eff}}$ . However, annealing at 300°C does not enhance the effective carrier lifetime of samples that were degraded by annealing at high temperatures  $T \geq 400^\circ\text{C}$ .

The stability of the a-Si:H single layer passivation and of the a-Si:H/SiN<sub>x</sub> double layer passivation is demonstrated for temperatures up to 500°C, which has also been found for the a-Si:H/SiN<sub>x</sub>-passivated emitters as shown in Section 4.2. In order to maintain the advantage of the better surface passivation of a-Si:H when compared to a screen-printed aluminum back-surface field layer as it is applied for the base passivation of industrial solar cells, it is demanded that the effective surface recombination velocity of the sample be smaller than  $S_{\text{eff}} \leq 100 \text{ cm/s}$  after the annealing [67]. The maximum annealing time at 500°C is therefore 1 min for the a-Si:H single-layer passivated samples, and 15 min for the a-Si:H/SiN<sub>x</sub> double-layer passivated samples.

## 7.2 Formation of defects during annealing

In order to determine the density of the thermally induced defect states at the a-Si:H/c-Si interface, and in the a-Si:H bulk, the defect model of Section 5.2 is fitted to reproduce the injection-dependent carrier lifetime curves of the annealed a-Si:H single layer-passivated samples. The approach is the same as in Section 6.2.

The ratio of the carrier capture cross sections of the interface dangling bond states has been already found in Section 6.2,  $\sigma_{\text{charged}}/\sigma_{\text{non-charged}} = 2000$ , and is therefore fixed at this value. The density of the dangling bonds in the a-Si:H bulk  $N_{\text{DB}}$ , and the density of the dangling bonds at the a-Si:H/c-Si interface  $D_{\text{it}}$  are adjusted to fit the temperature-degraded effective carrier lifetimes of the a-Si:H single layer-passivated samples that are shown in Section 7.1.

### 7.2.1 Results

Both, the measured lifetime curves, and the best fitted curves are shown in Figure 7.2 together with the dangling bond densities that lead to the best fit of the model to the experimental data. The accuracy for the determination of the dangling bond densities is about  $\pm 50\%$  for the interface defects. The dangling bond states in the a-Si:H bulk contribute little to the effective surface recombination rate, as

shown in Section 6.2. Therefore, only the upper limit of their density  $N_{\text{DB}}$  that is compatible with the measured carrier lifetimes can be given.

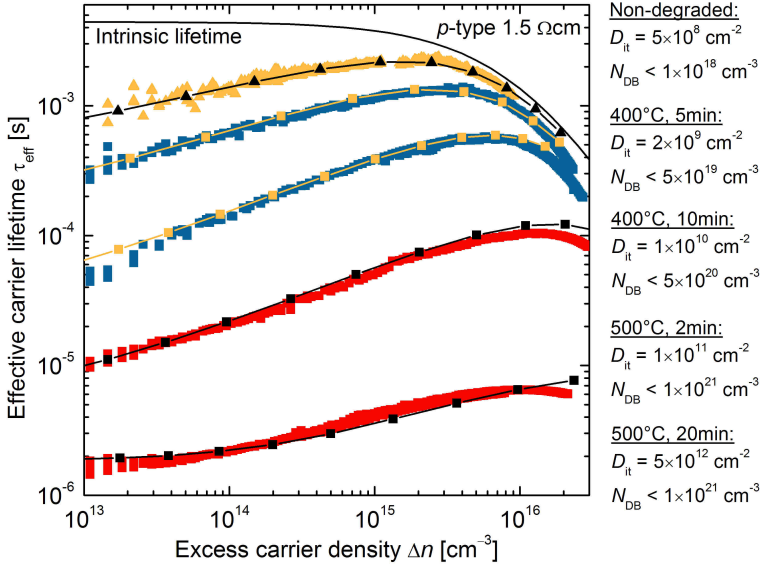


Figure 7.2: *Effective carrier lifetime  $\tau_{\text{eff}}$  of annealed p-type silicon (1.5  $\Omega\text{cm}$ ) passivated on both sides by 10 nm of a-Si:H. The symbols denote the lifetime measured by QSSPC. The annealing temperature and the annealing time are noted together with the dangling bond densities obtained from the best fit curve. The lines denote the lifetimes simulated by AFORS-HET.*

The defect density at the interface increases by four orders of magnitude from  $5 \times 10^8 \text{ cm}^{-2}$  in the non-degraded state to  $5 \times 10^{12} \text{ cm}^{-2}$  after annealing for 20 min at 500°C. The best fits to the experimental data are obtained when the dangling bond density in the a-Si:H bulk is increased from  $N_{\text{DB}} < 1 \times 10^{18} \text{ cm}^{-3}$  to  $N_{\text{DB}} < 1 \times 10^{21} \text{ cm}^{-3}$ .

Increasing the bulk density of the dangling bonds further than  $1 \times 10^{21} \text{ cm}^{-3}$  leads to no change of the simulated effective carrier lifetime. It is therefore the upper limit of the defect density  $N_{\text{DB}}$  when fitting the defect model to the experimental data.

### 7.2.2 Discussion

The injection-dependent carrier lifetime of the thermally degraded, a-Si:H passivated wafers is fitted by the same defect model as the carrier lifetimes of the samples that are degraded by illumination, as shown in Chapter 6. The dangling bond density at the a-Si:H/c-Si interface increases by four orders of magnitude during annealing for 20 min at 500°C.

Annealing of the a-Si:H-passivated c-Si wafers at 300°C maintains the excellent passivation quality even when the samples are annealed for up to 30 min, as shown in Section 7.1. In contrast, annealing at temperatures larger than 400°C leads to a degradation of the passivation quality. In the following, a qualitative explanation of the temperature-dependence of the formation of dangling bonds during annealing is proposed, which is based on the temperature-dependence of the diffusivity of hydrogen within the amorphous silicon:

Bentzen et al. showed experimentally that there is a correlation between the hydrogen content detected by ion-beam nuclear reaction analysis at the a-Si:H/c-Si interface, and the effective surface recombination velocity. They showed that an increase of the hydrogen content at the interface during annealing coincided with a decrease of the effective surface recombination velocity [86]. Annealing at higher temperatures led to a degradation of the passivation quality, which coincided with a decrease of the hydrogen concentration at the a-Si:H/c-Si interface.

It is therefore assumed that the bonding of hydrogen atoms to the dangling bond orbitals of the c-Si surface atoms is essential for the effective passivation of the a-Si:H/c-Si interface, besides the formation of Si-Si bonds. This was also shown by tight-binding molecular dynamics simulations of the a-Si:H deposition process [61]. The thermally activated desorption of one hydrogen atom during the annealing then either leaves a newly created Si-Si bond, or a Si dangling bond in place of the broken Si-H bond. Therefore, the density of the dangling bonds in the a-Si:H bulk eventually increases upon hydrogen desorption.

Street et al. showed that hydrogen starts to diffuse freely in non-doped a-Si:H at a temperature of (250...300)°C. The diffusion coefficient increases by three orders of magnitude from  $10^{-16} \text{ cm}^2\text{s}^{-1}$  at 300°C to  $10^{-13} \text{ cm}^2\text{s}^{-1}$  at 400°C [125]. This means that the desorption of hydrogen out of the a-Si:H bulk can occur at a rate that is  $10^3$  times higher at 400°C than at 300°C.

At low temperatures,  $T \approx 300^\circ\text{C}$ , hydrogen atoms start to diffuse freely within the a-Si:H bulk, which allows for the re-arrangement of the Si-H bonds so that the amount of dangling silicon bonds is further reduced when compared to the as-deposited state. Upon annealing of the samples at higher temperatures,  $T \geq 400^\circ\text{C}$ , the diffusion coefficient of hydrogen is at least three orders of magnitude higher, which means that also the out-diffusion of the hydrogen from the a-Si:H layer is by a factor of  $10^3$  faster. The creation of dangling bonds at the interface

and in the a-Si:H bulk due to the hydrogen desorption is then the dominating effect, when compared to the atomic rearrangement. Therefore, the passivation quality decreases during annealing at  $T \geq 400^\circ\text{C}$ , due to the increase of the dangling bond densities  $N_{\text{DB}}$  and  $D_{\text{it}}$ .

Applying a  $\text{SiN}_x$  capping layer on top of the passivating a-Si:H layer enhances the thermal stability of the passivation, because the  $\text{SiN}_x$  layer acts as a source of additional hydrogen atoms that diffuse freely within the double layer structure. This was also shown by the measurements of Bentzen et al. [86].

### 7.3 Defect density at the a-Si:H/c-Si interface of passivated emitters

The a-Si:H/c-Si interface density of states is shown in this Section as a function of the post-deposition annealing temperature, and of the a-Si:H layer thickness for boron- and phosphorus-diffused samples, by fitting the recombination model shown in Section 5 to the experimentally obtained carrier lifetimes. The experimental data are taken from the a-Si:H/ $\text{SiN}_x$  double-layer passivated samples featuring boron- and phosphorus-diffusions that are shown in Section 4.2.

#### 7.3.1 Assumptions

In order to simulate the effective carrier lifetime of the boron- and phosphorus-diffused wafers by AFORS-HET, the dopant profiles shown in Section 4.2 are approximated by a linear decrease of the doping concentration, starting at the surface with the measured surface concentration and ending at the measured junction depth.<sup>1</sup> The  $90\ \Omega/\square$  phosphorus-diffused emitter and the  $225\ \Omega/\square$  boron-diffused emitter are chosen for the simulation, because they show the best surface passivation after a-Si:H/ $\text{SiN}_x$  deposition and optimum post-deposition anneal, as described in Section 4.2.

The emitter surface is passivated with an a-Si:H/ $\text{SiN}_x$  double layer. However, Section 4.1.2 has shown that the  $\text{SiN}_x$  capping layer does not change the passivation quality or the injection-dependence of the effective carrier lifetime, when compared to an a-Si:H single-layer passivated sample. Therefore the  $\text{SiN}_x$  layer is omitted in the simulation, which reduces calculation time and enhances the stability of the iterative simulation process. The ratio of the capture cross sections of the interface

<sup>1</sup>The version of AFORS-HET used in this work allows no doping profiles other than linear gradients. However, the surface doping concentration is the most important parameter that determines the efficiency of the surface passivation.

defects is  $\sigma_{\text{charged}}/\sigma_{\text{non-charged}} = 2000$ , as found in Section 6.2. The dangling bond densities at the a-Si:H/c-Si interface  $D_{\text{it}}$ , and in the a-Si:H bulk,  $N_{\text{DB}}$  are fitted to reproduce the measured injection-dependent carrier lifetimes of the samples.

### 7.3.2 Results

Figure 7.3a shows the effective carrier lifetime curves of the best-passivated boron-diffused sample, as shown in Section 4.2.3. The emitter saturation current is  $J_{0e} = (24 \pm 2)$  fA/cm<sup>2</sup> after annealing at 400°C for 5 min. For comparison, the effective carrier lifetime of a sample that was annealed at 300°C is shown. This sample shows an emitter saturation current of  $J_{0e} = (71 \pm 8)$  fA/cm<sup>2</sup>. The thickness of the a-Si:H layer is 10 nm in both cases. The dangling bond densities in the a-Si:H bulk  $N_{\text{DB}}$ , and at the interface  $D_{\text{it}}$ , of the best fits are shown in Table 7.1, as well as the uncertainty intervals of the fits to the measured data. Annealing the samples at 400°C instead of 300°C reduces the density of the interface defects by a factor of 5, from  $N_{\text{DB}} = 4 \times 10^{11}$  cm<sup>-2</sup> to  $N_{\text{DB}} = 8 \times 10^{10}$  cm<sup>-2</sup>.

Figure 7.3b shows the effective carrier lifetime curves of the best-passivated phosphorus-diffused sample, as shown in Section 4.2.2. The emitter saturation current is  $J_{0e} = (18 \pm 2)$  fA/cm<sup>2</sup>, with a 10 nm thick a-Si:H layer. For comparison, the effective carrier lifetime of a sample that is passivated by only a 3 nm thick a-Si:H layer is shown. This sample shows an emitter saturation current of  $J_{0e} = (68 \pm 8)$  fA/cm<sup>2</sup>. Both samples are annealed at 300°C for 5 min. The thinner a-Si:H layer leads to a 4 times higher defect density at the a-Si:H/c-Si interface.

In order to fit the effective carrier lifetimes of the phosphorus-diffused samples for  $\Delta n < 10^{15}$  cm<sup>-3</sup> correctly, an additional recombination level at the c-Si midgap has to be assumed for the bulk recombination of the substrate wafer, with the capture time constants  $\tau_{n0} = \tau_{p0} = 3.5$  ms.

### 7.3.3 Discussion

The dangling bond density at the a-Si:H/c-Si interface of the boron-diffused samples decreases by a factor of 5 when the post-deposition annealing temperature is increased from 300°C to 400°C, which results in the observed decrease of the emitter saturation current. The dangling bond density in the a-Si:H bulk has virtually no influence of the simulated lifetime curve. This confirms that the defect density at the a-Si:H/c-Si interface determines the quality of the surface passivation, as it is shown in Section 6.2.2 for the lowly-doped c-Si wafers. The upper limit that is obtained from the defect model is  $N_{\text{DB}} \leq 1 \times 10^{21}$  cm<sup>-3</sup>, which is half the density of the of the electronic states at the valence band edge, as shown in Figure 5.1. Assuming higher defect densities has no effect on the simulated carrier lifetime.

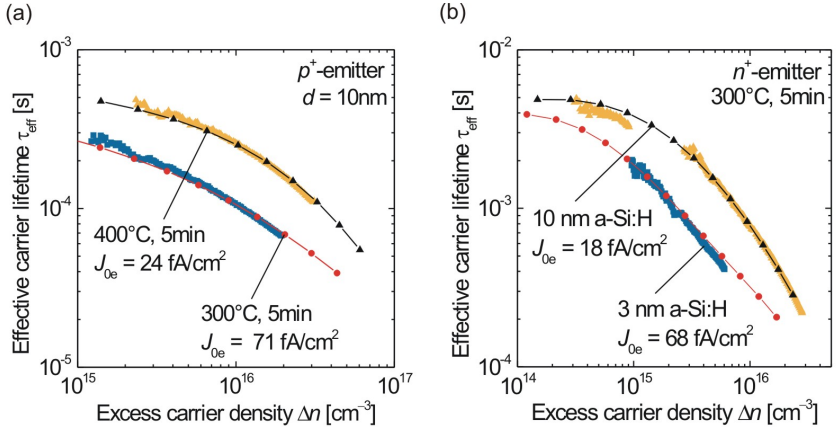


Figure 7.3: *High-injection effective carrier lifetime*  $\tau_{\text{eff}}$  of (a) a 10  $\Omega\text{cm}$  *p*-type silicon wafer featuring a 225  $\Omega/\square$  boron diffusion and *a-Si:H/SiN<sub>x</sub>* passivation on both sides, and (b) a 200  $\Omega\text{cm}$  *n*-type silicon wafer featuring a 90  $\Omega/\square$  phosphorus diffusion and *a-Si:H/SiN<sub>x</sub>* passivation on both sides. The symbols denote the lifetime measured by QSSPC. The lines with symbols denote the lifetimes simulated by AFORS-HET. The ratio of the interface capture cross sections is fixed,  $\sigma_{\text{charged}}/\sigma_{\text{non-charged}} = 2000$ . The dangling bond densities of the best fits, and the uncertainty intervals of the fits are given in Table 7.1. The emitter saturation current densities  $J_{0e}$  are extracted from the measured lifetimes by the Kane-Swanson method in the Section 4.2.

The phosphorus-diffused sample that is passivated by an only 3 nm thin *a-Si:H* layer is fitted best with a 5 times higher defect density at the interface, than the sample with 10 nm *a-Si:H*. This indicates that the main reason for the non-optimum passivation with *a-Si:H* thicknesses smaller than 5 nm is *not* a possibly higher dangling bond density in the *a-Si:H* bulk, but a higher interface density of defects, which is assumed to be due to remaining pinholes in the thin *a-Si:H* film, as discussed in Section 4.1. Pinholes would make this a two-dimensional problem, and the dangling bond density  $D_{\text{it}}$  that is extracted from the simulations would be an effective one, under the assumption of a uniformly passivated surface.

The simulated defect densities  $N_{\text{DB}}$  and  $D_{\text{it}}$  of the best-passivated samples are about two orders of magnitude higher than those found in Section 6.2.2 for the best-



Table 7.1: Dangling bond densities obtained from fitting the high-injection effective carrier lifetime of the a-Si:H/SiN<sub>x</sub> passivated boron-diffused (p<sup>+</sup>) and phosphorus-diffused (n<sup>+</sup>) emitters as shown in Figure 7.3. The boron-diffused samples are in different stages of post-deposition annealing, while the phosphorus-diffused samples feature different thicknesses  $d$  of the a-Si:H layer.

	Parameter	Best fit	Uncertainty interval
p <sup>+</sup> -emitter, 400°C	$N_{\text{DB}}$	$5 \times 10^{20} \text{ cm}^{-3}$	$\leq 1 \times 10^{21} \text{ cm}^{-3}$
	$D_{\text{it}}$	$8 \times 10^{10} \text{ cm}^{-2}$	$(5 \times 10^{10} \dots 1 \times 10^{11}) \text{ cm}^{-2}$
p <sup>+</sup> -emitter, 300°C	$N_{\text{DB}}$	$5 \times 10^{20} \text{ cm}^{-3}$	$\leq 1 \times 10^{21} \text{ cm}^{-3}$
	$D_{\text{it}}$	$4 \times 10^{11} \text{ cm}^{-2}$	$(2 \times 10^{11} \dots 5 \times 10^{11}) \text{ cm}^{-2}$
n <sup>+</sup> -emitter, 10 nm a-Si:H	$N_{\text{DB}}$	$1 \times 10^{20} \text{ cm}^{-3}$	$\leq 5 \times 10^{20} \text{ cm}^{-3}$
	$D_{\text{it}}$	$5 \times 10^{10} \text{ cm}^{-2}$	$(1 \times 10^{10} \dots 1 \times 10^{11}) \text{ cm}^{-2}$
n <sup>+</sup> -emitter, 3 nm a-Si:H	$N_{\text{DB}}$	$5 \times 10^{20} \text{ cm}^{-3}$	$\leq 1 \times 10^{21} \text{ cm}^{-3}$
	$D_{\text{it}}$	$2 \times 10^{11} \text{ cm}^{-2}$	$(1 \times 10^{11} \dots 3 \times 10^{11}) \text{ cm}^{-2}$

passivated lowly-doped surfaces. However, they comply with the recombination velocities  $S_e = (1 \dots 5) \times 10^3 \text{ cm/s}$ , that were obtained in Reference [87] for boron-diffused emitters that are passivated with the same a-Si:H/SiN<sub>x</sub> double layers as the samples shown in this work.

The best-passivated boron-diffused sample shown in Figure 7.3a features a surface boron concentration of  $N_{\text{surf}} = 3 \times 10^{19} \text{ cm}^{-3}$ , emitter saturation current density  $J_{0e} = 24 \text{ fA/cm}^2$ , and the interface density of states  $D_{\text{it}} = 8 \times 10^{10} \text{ cm}^{-2}$  as simulated with AFORS-HET. This results in the fundamental surface recombination velocity  $S_{n0} = v_{\text{th}}\sigma_n D_{\text{it}} = 8 \times 10^3 \text{ cm/s}$ . Simulations that were performed with the finite-element semiconductor device simulator SENTAURUS in Reference [87], indicate  $S_{n0} = v_{\text{th}}\sigma_n D_{\text{it}} = 7 \times 10^3 \text{ cm/s}$  for a boron diffused emitter with  $N_{\text{surf}} = 3 \times 10^{19} \text{ cm}^{-3}$  that is passivated by the same a-Si:H/SiN<sub>x</sub> double layers that are used in this work. This means that, within the uncertainty interval of the calculations presented in this Section, both methods result in the same interface defect density, which confirms the validity of the defect model derived in Section 5.2.



## 8 Application to solar cells

The COSIMA technique allows for the surface passivation of both, the emitter and the base of solar cells, and for the contact formation at low temperatures  $T \leq 300^\circ\text{C}$ . The solar cell designs shown in this Chapter are modified from bifacial cells developed at ISFH, that feature  $\text{SiN}_x$ -passivation of both, the emitter side (front side) and the base side (rear side) [6, 126]. These cells are named symmetric- $\text{SiN}_x$  cells in this work. In the first step, the rear  $\text{SiN}_x$  layer is substituted by a-Si:H. The resulting design is called the rear-COSIMA cell. Section 8.1 shows the processing sequence, and the current-voltage- and recombination-characteristics of rear-COSIMA solar cells, as compared to those of symmetric- $\text{SiN}_x$  cells.

In the second step, the COSIMA technique is applied to both, the emitter and the base side of solar cells. The resulting design is called the symmetric-COSIMA solar cell. Section 8.2 shows the optimization of the width of the front a-Si:H layer for maximum energy conversion efficiency, and the characteristics of the optimized symmetric-COSIMA solar cells.

### 8.1 Rear-COSIMA solar cells

The performance of rear-COSIMA cells is compared to that of symmetric- $\text{SiN}_x$  cells. Section 8.1.1 explains the considerations that lead to the choice of the contact layout that is applied to the emitter and base. The processing sequences for both kinds of cells are shown in Section 8.1.2. In Sections 8.1.3 and 8.1.4 the rear-surface passivation quality of the cells is discussed, as obtained from the analysis of current-voltage- and quantum efficiency-measurements, respectively.

#### 8.1.1 Contact layout

As shown in Section 2.6, the layout of the rear contact grid has not only an impact on the series resistance of a solar cell, but also on the effective carrier recombination rate and thus the diode saturation current. The same is true for the front contact grid, which must be furthermore designed to minimize shading losses. Therefore, the layouts of the contact grids have to be optimized for a maximum energy conversion efficiency of the solar cell, for each specific kind of surface passivation and

contact formation according to the specific values of the local surface recombination velocities  $S_{\text{met}}$  and  $S_{\text{pass}}$ , and of the contact resistivity  $\rho_c$ .

The layout of stripe-shaped front and rear contact grids of symmetric-SiN<sub>x</sub> solar cells was experimentally optimized by Hübner et al., as shown in Reference [6]. Since the rear-COSIMA solar cells feature the same front side as the symmetric-SiN<sub>x</sub> cells, the design of the front contact grid is taken from Reference [6] for this work. The emitter contacts and busbar cover 4% of the cell area.

In order to find the optimum layout of the local contacts to the COSIMA-processed base, the following questions have to be considered:

- **Dot- or stripe-contact layout:** As shown in Section 2.6.5, a solar cell with dot-contact layout features a larger base series resistance, but smaller base saturation current density than with a stripe-contact layout of the same coverage  $f$  and period length  $p$ . These two effects adversely affect the efficiency of a cell. Catchpole and Blakers have shown by three-dimensional numerical modeling, that the maximum possible energy conversion efficiency of PERC-cells is indeed the same for dot- and stripe contact layouts if the respective optimum values of  $f$  and  $p$  are applied [47].

Stripe-shaped contacts and their connecting busbar can be evaporated onto the passivating a-Si:H layer through a shadow mask, in one single process step. In contrast, the application of a dot-contact layout would require at least the deposition of a masking layer onto the a-Si:H film, and its structuring to define the contact areas. A stripe-contact layout is therefore chosen for the solar cells that are developed in this work, to keep the process sequence simple.

- **Contact coverage and spacing:** A stripe-shaped base contact grid was already optimized by Hübner et al. [6], for Al contacts that were evaporated onto the base before the deposition of the passivation layer. Section 3.2.3 shows that the contact resistivity  $\rho_c$  achieved with the COSIMA technology is the same as for the contact formation applied in Reference [6]. Therefore, Hübner's optimum base grid design would result in approximately the same series resistance when applied to rear-COSIMA cells, and to symmetric-SiN<sub>x</sub> cells.

Furthermore, the silicon nitride layers that were used by Hübner et al. for surface passivation exhibit similar SRVs as the a-Si:H layers shown in this work,  $S_{\text{pass}} \approx 5 \text{ cm/s}$  at  $\Delta n = 10^{15} \text{ cm}^{-3}$  [6].<sup>1</sup> In both cases, the surface areas

---

<sup>1</sup>A SiN<sub>x</sub> double layer structure was used, with a thin Si-rich SiN<sub>x</sub> layer (refractive index 2.3) for surface passivation, which was capped by a SiN<sub>x</sub> layer with lower Si content (refractive index 2.05). The surface passivation quality of Hübner's cells is therefore close to that of the a-Si:H-passivated cells discussed in this work.

below the local base contacts are non-passivated, with  $S_{\text{met}} \approx 10^6$  cm/s. It is therefore obvious from Equation 2.65 that the optimum grid design of Reference [6] would result in approximately the same base saturation current when applied to rear-COSIMA cells, and to symmetric-SiN<sub>x</sub> cells, respectively. The design of the rear contact grid is therefore adopted from Reference [6] for the solar cells that are developed in this work.

In conclusion, the layouts of the front- and rear-contact grid are taken from Reference [6], because they are found to be also the optimum layouts for the rear-COSIMA solar cells, according to the model shown in Section 2.6. The contact coverage and stripe spacing of the rear contact grid are  $f = 5\%$ , and  $p = 2$  mm, for a specific resistivity of the  $p$ -type base of  $\rho = 0.5 \Omega\text{cm}$ .

### 8.1.2 Processing sequence

The structure of a rear-COSIMA solar cell is schematically shown in Figure 8.1. (100)-oriented boron-doped FZ-Si wafers with a thickness of  $300 \mu\text{m}$  and a resistivity of  $0.5 \Omega\text{cm}$  are used as base material. The cell area is  $4 \text{cm}^2$  and includes the entire metalization, with the front and rear busbars.

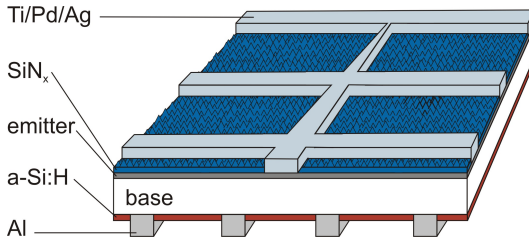


Figure 8.1: *Schematic structure of a rear-COSIMA solar cell. The base is passivated by a 10 nm-thick a-Si:H film deposited at 230°C, and features COSIMA-annealed local Al contacts. The emitter is passivated by a SiN<sub>x</sub> film that is deposited at 325°C.*

The cell area is defined by a 200 nm-thick thermally grown oxide film that is removed within a  $2 \times 2 \text{cm}^2$  large square on the front surface of the wafer. The front side is textured by randomly distributed pyramids that are formed by anisotropic etching in a KOH/isopronanol solution. Subsequently, an  $n^+$ -doped emitter with a sheet resistivity of  $90 \Omega/\square$  is formed by phosphorus-diffusion, as described in Section 4.2.1. Both, surface texture and emitter diffusion are restricted to the cell area by the masking oxide.

After removal of the masking oxide in diluted HF, solar cells with two different rear configurations are prepared, featuring an a-Si:H- or a SiN<sub>x</sub>-passivated rear surface. The base of the rear-COSIMA cells is covered by a 10 nm thick a-Si:H film, deposited by PECVD at 225°C as shown in Section 3.1. Subsequently, 15 μm of Al is evaporated onto the rear side, through a shadow mask that features the optimum grid design as described above. The Ti/Pd/Ag front contact grid (80 nm Ti, 50 nm Pd, 10 μm Ag) is also applied by electron-beam evaporation of the pure metals through a shadow mask.

The front SiN<sub>x</sub> layer which acts as surface-passivating anti-reflective coating, is deposited by PECVD at 325°C. The cells are heated to  $T > 300^\circ\text{C}$  for about 5 min during the SiN<sub>x</sub> deposition, which is enough to complete the COSIMA-annealing of the Al base contacts. Thus, the formation of the rear contacts, and the deposition of the front antireflective coating are performed in one single process step.

Symmetric-SiN<sub>x</sub> cells are prepared for comparison. They feature the same front side, and the same Al rear contact grid layout as the rear-COSIMA cells. In contrast to the a-Si:H-passivated cells, the base is passivated by a 60 nm thick SiN<sub>x</sub> layer with refractive index  $n = 2.1$ , that is deposited by remote-PECVD at 400°C as described in Section 3.1.

### 8.1.3 Current-voltage characteristics

Figure 8.2 shows the current-voltage curve of the best rear-COSIMA solar cell, as measured at Fraunhofer ISE CalLab under standard testing conditions (25°C, 100 mW/cm<sup>2</sup>, AM1.5-global spectrum). The short-circuit current density is  $J_{sc} = 38.0 \text{ mA/cm}^2$ , and the open-circuit voltage  $V_{oc} = 657 \text{ mV}$ . The energy conversion efficiency is  $\eta = 20.1\%$ . The high fill factor of  $FF = 80.5\%$  of the a-Si:H-passivated cell demonstrates the low resistivity of the COSIMA contacts.

The lumped series resistance  $R_s = (0.4 \pm 0.05) \Omega\text{cm}^2$  in maximum power point conditions is obtained from the voltage shift between the dark- and the illuminated-current-voltage curve, as described in Reference [127]. This value of  $R_s$  is in the same range as series resistances that were obtained for PERL- (passivated emitter and rear locally diffused) solar cells with an efficiency of 22% [127].

Sets of eight solar cells each are prepared with a-Si:H-passivated rear, and with SiN<sub>x</sub>-passivated rear. The mean values of the short circuit current density and of the open-circuit voltage of the SiN<sub>x</sub>-passivated cells are reduced by  $\Delta J_{sc} = (0.5 \pm 0.1) \text{ mA/cm}^2$ , and  $\Delta V_{oc} = (4 \pm 2) \text{ mV}$  when compared to the mean values of the rear-COSIMA cells (not shown in the Figure). Analysis of the internal quantum efficiency shows that this effect is due to shunting of the base contacts and the charge-induced inversion layer below the passivating SiN<sub>x</sub> film.

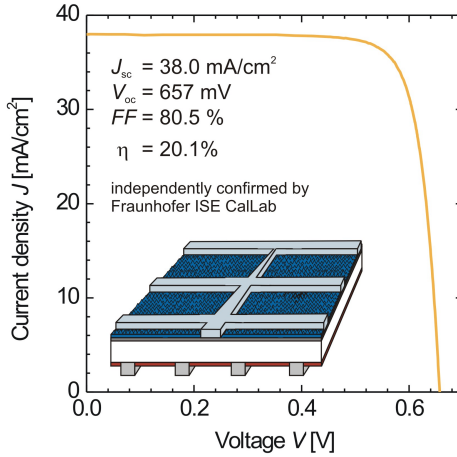


Figure 8.2: *Current-voltage characteristics of the best rear-COSIMA solar cell. The energy conversion efficiency is 20.1% under standard test conditions (25°C, 100 mW/cm<sup>2</sup>, AM1.5 global), as measured at the Fraunhofer ISE CalLab. The cell area is 4 cm<sup>2</sup>.*

### 8.1.4 Internal quantum efficiency

The internal quantum efficiency (*IQE*) of the rear-COSIMA cells, and of the symmetric-SiN<sub>x</sub> cells is obtained from measurements of the spectral response and of the reflectance of the cells. The internal quantum efficiency is defined as the spectrally resolved ratio of collected carriers to absorbed photons. It is experimentally obtained from

$$IQE(\lambda) = \frac{hc J_{sc}(\lambda)}{q\lambda \Phi_{in}(\lambda)(1 - R(\lambda))}, \quad (8.1)$$

where  $J_{sc}(\lambda)$  is the short-circuit current density under monochromatic illumination,  $\Phi_{in}$  is the intensity of the illumination in [Wm<sup>-2</sup>], and  $R$  is the reflectance of the solar cell. The value  $J_{sc}(\lambda)/\Phi_{in}(\lambda)$  is the spectral response, and  $hc/\lambda$  is the photon energy.

The inverse absorption coefficient  $\alpha^{-1}$  denotes the penetration depth of the incident light. It changes from the order of  $\mu\text{m}$  for incident light in the ultraviolet wavelength range, to a few cm for light in the infrared wavelength range. The internal quantum efficiency is therefore sensitive to the depth-profile of the carrier

recombination rate within a solar cell. Carrier recombination in the base, and at its surface, determines the  $IQE$  for wavelengths with a penetration depth in Si that is large when compared to the depth of the  $pn$ -junction, but smaller than the thickness of the cell,  $z_{\text{jct}} \ll \alpha^{-1} \ll W$ . For  $\alpha^{-1} \geq W$ , the  $IQE$  is controlled also by the optical properties of the rear side [128].

Figure 8.3 shows the internal quantum efficiencies of a rear-COSIMA cell and a symmetric-SiN<sub>x</sub> cell, as a function of the wavelength  $\lambda$ . White bias light with an intensity of 0.3 suns was applied during the measurement. The effective diffusion

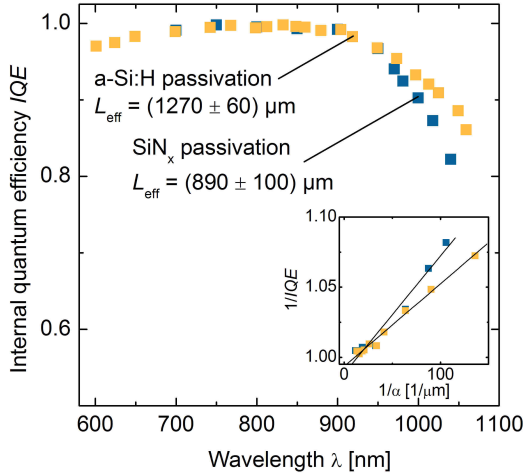


Figure 8.3: Near-infrared internal quantum efficiency  $IQE$  of a rear-COSIMA solar cell, and a reference cell with SiN<sub>x</sub>-passivated base. The inset shows the inverse  $IQE$  as a function of the penetration depth  $\alpha^{-1}$  in the range  $800 \text{ nm} < \lambda < 1000 \text{ nm}$ . The effective diffusion length  $L_{\text{eff}}$  is determined from the slope of the fitted lines.

length  $L_{\text{eff}}$  in the base as a measure of the rear passivation quality, is obtained from the  $IQE$  in the near infrared wavelength range  $800 \text{ nm} < \lambda < 1000 \text{ nm}$ . It is given by [128, 129]

$$IQE^{-1} = 1 + \frac{\cos \theta}{L_{\text{eff}}} \alpha^{-1}, \quad (8.2)$$

where  $\theta = 41.8^\circ$  is the angle between the random-pyramid surface and the incident light. The value of  $L_{\text{eff}}$  is thus obtained from the slope of a linear fit to the inverse



$IQE$  as a function of the inverse absorption coefficient  $\alpha^{-1}$ , as shown in the inset of Figure 8.3.

## Results

The effective diffusion length  $L_{\text{eff}}$  determines the base saturation current density  $J_{0\text{b}}$  and the effective rear surface recombination velocity  $S_{\text{eff}}$ , respectively, by Equation 2.28. Table 8.1 shows the values of  $L_{\text{eff}}$ ,  $J_{0\text{b}}$ , and  $S_{\text{eff}}$  that are obtained from the  $IQE$  curves shown in Figure 8.3. The uncertainty interval of the effective diffusion length  $L_{\text{eff}}$  is determined from the confidence interval of the linear fit to the inverse  $IQE$ . Carrier recombination in the bulk is assumed to be Auger-limited. The value  $S_{\text{pass}}$  denotes the local SRV in the non-metalized areas of the base,

Table 8.1: *Effective diffusion length  $L_{\text{eff}}$ , base saturation current  $J_{0\text{b}}$ , and effective rear SRV  $S_{\text{eff}}$  determined from the internal quantum efficiency of the rear-COSIMA cell and the symmetric-SiN<sub>x</sub> cell shown in Figure 8.3.*

	Rear-COSIMA cell	Symmetric-SiN <sub>x</sub> cell
$L_{\text{eff}}$ [ $\mu\text{m}$ ]	$1270 \pm 60$	$890 \pm 100$
$J_{0\text{b}}$ [ $\text{fA}/\text{cm}^2$ ]	$83 \pm 5$	$120 \pm 30$
$S_{\text{eff}}$ [ $\text{cm}/\text{s}$ ]	$190 \pm 15$	$300 \pm 60$
$S_{\text{pass}}$ [ $\text{cm}/\text{s}$ ]	$30 \pm 15$	$140 \pm 60$

as obtained from the base saturation current by the interpolation model shown in Section 2.6.5. The local SRV below the base contact stripes is assumed to be  $S_{\text{met}} = 10^6$  cm/s, as is experimentally shown in Section 3.3.

The internal quantum efficiency of the a-Si:H-passivated solar cell in the near-infrared wavelength range outperforms that of the SiN<sub>x</sub>-passivated reference cell, due to the more effective surface passivation by a-Si:H, than by SiN<sub>x</sub>. The local SRV  $S_{\text{pass,a-Si:H}} = (30 \pm 15)$  cm/s that is obtained from  $J_{0\text{b,a-Si:H}} = (83 \pm 5)$  fA/cm<sup>2</sup> by Equation 2.65, agrees with the effective SRV that is obtained in Section 6.1.1 for a-Si:H-passivated wafers after Staebler-Wronski degradation. The local SRV in the passivated surface areas of the symmetric-SiN<sub>x</sub> cell is significantly larger,  $S_{\text{pass,SiN}_x} = (140 \pm 60)$  cm/s.

The larger surface recombination velocity of the SiN<sub>x</sub>-passivated cells is mainly due to shunting of the charge-induced floating junction below the SiN<sub>x</sub> film, and the rear metal contacts, as shown in References [1, 2]: The floating junction is caused by the high density of fixed positive charges in the SiN<sub>x</sub> film that leads to the formation of an inversion layer at the rear surface of the  $p$ -type base. An electron in the inversion layer can either be re-injected into the base, or flow towards

the base contacts where it recombines with a hole. In the latter case it does not contribute to the cell current. Thus, shunting of the inversion layer and the base contacts generates an additional recombination path at the rear surface. This effect increases the local SRV  $S_{\text{pass}}$  of a  $\text{SiN}_x$ -passivated solar cell when compared to a non-contacted device, like  $\text{SiN}_x$ -coated *c*-Si wafers that are typically used for lifetime measurements. The value of  $S_{\text{pass, SiN}_x} = (140 \pm 60)$  cm/s was also shown in Reference [2] for solar cells that feature the same rear-side layout as the symmetric- $\text{SiN}_x$  cells shown in this Section.

Since the a-Si:H passivation layer contains no fixed charges [3], no floating junction forms at the rear surface of rear-COSIMA cells. The local SRV at the a-Si:H-passivated surface regions is therefore the same, as on the non-contacted devices used for the characterization of the a-Si:H/*c*-Si interface in Sections 4, 6, and 7.

### Comparison to current-voltage characteristics

Both, the open-circuit voltage and the short-circuit current of the symmetric- $\text{SiN}_x$  cells are reduced when compared to the results obtained for rear-COSIMA cells, as shown in Section 8.1.3. This effect can be understood in terms of the higher rear surface recombination velocity of the  $\text{SiN}_x$ -passivated cells: Since both types of cells feature the same front side with the same optical properties, the difference in their short-circuit current can be calculated from the internal quantum efficiency,

$$\Delta J_{\text{sc}} = q \int (IQE_{\text{a-Si:H}} - IQE_{\text{SiN}_x}) \Phi_{\text{AM1.5G}} d\lambda, \quad (8.3)$$

where  $IQE_{\text{a-Si:H}}$  is the internal quantum efficiency of the rear-COSIMA solar cell,  $IQE_{\text{SiN}_x}$  is the internal quantum efficiency of the symmetric- $\text{SiN}_x$  cell, and  $\Phi_{\text{AM1.5G}}$  is the photon flux defined by the AM1.5G-spectrum. Equation 8.3 results in  $\Delta J_{\text{sc}} = 0.4$  mA/cm<sup>2</sup> with the quantum efficiencies shown in Figure 8.3. This result agrees with the range  $(0.5 \pm 0.1)$  mA/cm<sup>2</sup> that is obtained from the current-voltage characteristics of the cells, as shown above.

The emitter saturation current  $J_{0e} = (240 \pm 15)$  fA/cm<sup>2</sup> of the front side is analogously to Equation 2.27 given by

$$J_{0e} = \left[ \frac{\exp\left(\frac{qV_{\text{oc}}}{kT}\right) - 1}{J_{\text{sc}}} \right]^{-1} - J_{0b, \text{a-Si:H}}, \quad (8.4)$$

where the base saturation current density  $J_{0b, \text{a-Si:H}}$  is obtained from the  $IQE$  analysis of the rear-COSIMA cell, and the short-circuit current density  $J_{\text{sc}}$  and the open-circuit voltage  $V_{\text{oc}}$  are given by its current-voltage characteristics. The difference  $\Delta V_{\text{oc}}$  of the open circuit voltages that is due to the different rear passivation

schemes of the rear-COSIMA cell and the symmetric-SiN<sub>x</sub> cell is then

$$\Delta V_{oc} \approx \frac{kT}{q} \ln \left( \frac{J_{sc}}{J_{sc} - \Delta J_{sc}} \frac{J_{0e} + J_{0b, SiN_x}}{J_{0e} + J_{0b, a-Si:H}} \right) = (3 \pm 2) \text{ mV}, \quad (8.5)$$

which agrees with the value of  $\Delta V_{oc} = (4 \pm 2) \text{ mV}$  that is obtained from the current-voltage characteristics of the cells, as shown above.

The higher open-circuit voltage and short-circuit current of the rear-COSIMA solar cells compared to the symmetric-SiN<sub>x</sub> cells, are therefore attributed to the better passivation of the base by amorphous silicon compared to silicon nitride. The different infrared quantum efficiency of both cell types explains their different current-voltage characteristics.

## 8.2 Symmetric-COSIMA solar cells

Amorphous silicon films are applied to both, the emitter side and the base side the of symmetric-COSIMA solar cells. An overview of the processing steps is given in Section 8.2.1. Amorphous silicon absorbs light in the visible-wavelength range. It is therefore necessary to keep the a-Si:H film as thin as possible to minimize absorption while maintaining optimum surface passivation, when the a-Si:H layer is placed on the illuminated front side of a solar cell. Section 8.2.2 shows the optimization of the front-a-Si:H layer thickness for optimum energy conversion efficiency of symmetric-COSIMA solar cells. The optimized COSIMA-surface passivation leads to energy conversion efficiencies above 20%, which is shown in Section 8.2.3.

### 8.2.1 Processing sequence

Figure 8.4 shows the schematic structure of a symmetric-COSIMA solar cell, featuring the same rear side design as the rear-COSIMA cells. The processing sequence is the same as for the rear-COSIMA cells, except for the treatment of the emitter surface: The diffused emitter on the front side is covered by an a-Si:H-layer deposited at 225°C. The front Al grid is deposited by electron beam evaporation, with the same grid layout as for the rear-COSIMA cells. A SiN<sub>x</sub> antireflective layer is deposited by PECVD at a low temperature,  $T = 230^\circ\text{C}$ . Finally, the cells are annealed for 5 min at 300°C to form COSIMA contacts to both, emitter and base. The cell area is  $4 \text{ cm}^2$ , and includes the entire contact grids and busbars.

Symmetric-COSIMA solar cells without front texture are prepared to optimize the thickness of the front a-Si:H film for maximum efficiency. The front texture is

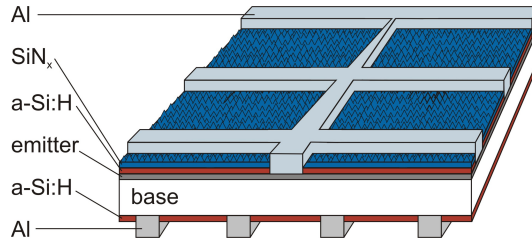


Figure 8.4: *Schematic structure of the symmetric-COSIMA solar cells. Both sides are passivated by a-Si:H, and feature local Al contacts. The thickness of the front a-Si:H layer is varied,  $1 \text{ nm} < d < 30 \text{ nm}$ . The base is passivated by a 10 nm-thick a-Si:H film. The front SiN<sub>x</sub> capping layer serves as an anti reflective coating. Both, the a-Si:H and SiN<sub>x</sub>-films are deposited at 230°C.*

omitted to simplify the interpretation of quantum efficiency measurements. The thickness of the a-Si:H film is varied in the range  $1.5 \text{ nm} \leq d \leq 30 \text{ nm}$ .

A second set of cells is prepared with a textured front side, and a front a-Si:H film of the optimum thickness, to show the efficiency potential of the symmetric-COSIMA technique. The equivalent thickness of the a-Si:H layer on a planar wafer is  $d = 6.5 \text{ nm}$ .

## 8.2.2 Optimum thickness of the front a-Si:H film

Figure 8.5a shows the open-circuit voltage of non-textured symmetric-COSIMA solar cells as a function of the thickness  $d$  of the front a-Si:H layer, under standard test conditions ( $25^\circ\text{C}$ ,  $100 \text{ mW}/\text{cm}^2$ , AM1.5-global spectrum). All cells feature the same a-Si:H passivated rear side. Each data point in Figure 8.5a represents the mean value of a set of four cells, and their statistical standard deviation is indicated by the error bars. The open-circuit voltage increases from  $V_{oc} = (653 \pm 1) \text{ mV}$  for  $d = 1.5 \text{ nm}$  to  $V_{oc} = (664 \pm 1) \text{ mV}$  for  $d = 6.5 \text{ nm}$ . Increasing  $d$  further has no effect on the open-circuit voltage.

This behavior agrees with the results shown in Section 4.2.2: The saturation current density of the  $n^+$ -emitter decreases with increasing layer thickness in the range  $d \leq 6.5 \text{ nm}$ , due to the increasing quality of the emitter surface passivation. The optimum emitter passivation results in the minimum saturation current density, which is obtained for  $d \geq 6.5 \text{ nm}$  as shown in Figure 4.4. Since the open-circuit voltage  $V_{oc}$  is determined by the emitter saturation current density as shown by Equation 2.27, it is obvious that  $V_{oc}$  must increase with increasing  $d$  for  $d \leq 6.5 \text{ nm}$ ,

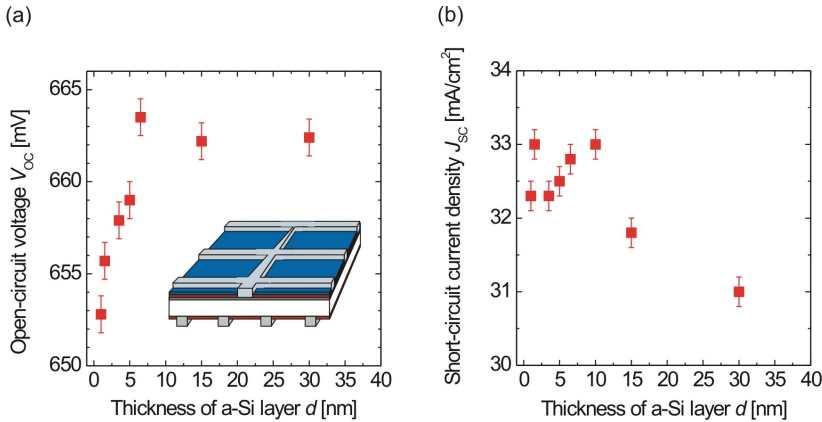


Figure 8.5: (a) Open-circuit voltage  $V_{oc}$ , and (b) short-circuit current density  $J_{sc}$  of non-textured symmetric-COSIMA solar cells. The optimum thickness of the front a-Si:H layer,  $5 \text{ nm} < d < 10 \text{ nm}$ , allows for both, high-quality surface passivation and low parasitic absorption of the incident light.

in the same way as the saturation current density  $J_{0e}$ .

Figure 8.5b shows the short-circuit current density  $J_{sc}$  of the non-textured symmetric-COSIMA cells, as a function of the thickness  $d$  of the front a-Si:H film. The short circuit current density is constant,  $J_{sc} = (32.8 \pm 0.5) \text{ mA/cm}^2$  in the range  $1.5 \text{ nm} \leq d \leq 10 \text{ nm}$ . Further increase of  $d$  up to 30 nm reduces  $J_{sc}$  by 4.5%.

The optimum a-Si:H thickness is in the range of  $5 \text{ nm} < d < 10 \text{ nm}$ , where both  $V_{oc}$  and  $J_{sc}$  are high. A cell with  $d = 6.5 \text{ nm}$  shows the maximum efficiency of  $\eta = 17.9\%$  with a planar front surface.

### Internal quantum efficiency

The internal quantum efficiency  $IQE$  of the symmetric-COSIMA solar cells is measured in order to determine the impact of surface passivation and parasitic absorption by the front a-Si:H film, on the short-circuit current  $J_{sc}$ . Figure 8.6 shows the  $IQE$  in the short-wavelength range  $\lambda \leq 750 \text{ nm}$ , for  $1.5 \text{ nm} \leq d \leq 30 \text{ nm}$ . The internal quantum efficiency of cells with  $d \geq 10 \text{ nm}$  decreases with increasing thickness  $d$  of the a-Si:H layer. However, the  $IQE$  of cells with  $d < 10 \text{ nm}$  shows only a small dependence on the a-Si:H thickness.

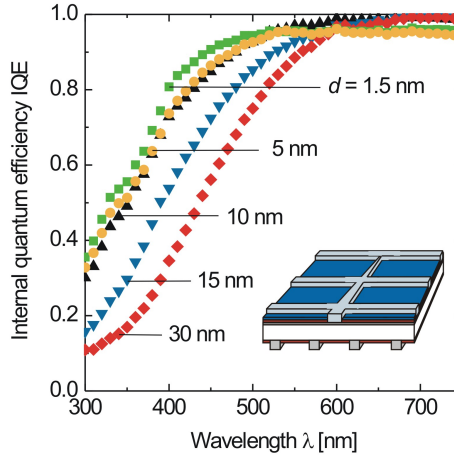


Figure 8.6: *Short-wavelength internal quantum efficiency IQE of non-textured symmetric-COSIMA solar cells. Due to less parasitic absorption in the a-Si:H film, the IQE increases with decreasing thickness of the front a-Si:H layer, for  $10 \text{ nm} < d < 30 \text{ nm}$ . For thinner a-Si:H layers, less absorption is compensated by an increase of the emitter surface recombination velocity.*

## Discussion

The optical bandgap energy  $E_{g, \text{a-Si:H}} \approx 1.7 \text{ eV}$  of hydrogenated amorphous silicon corresponds to a wavelength of  $\lambda_{g, \text{a-Si:H}} \approx 750 \text{ nm}$ . Photons of this wavelength have a penetration depth of  $7.5 \mu\text{m}$  in crystalline silicon, which is still in the vicinity of the *pn*-junction. Therefore, the IQE in the wavelength range  $\lambda < 750 \text{ nm}$  is sensitive to carrier recombination at the emitter surface.

The penetration depth of light in a-Si:H is given by the inverse absorption coefficient  $\alpha^{-1}$ , and increases with increasing wavelength [130]. At  $\lambda = 600 \text{ nm}$ , the penetration depth is  $\alpha^{-1} \approx 0.3 \mu\text{m}$ , which is 10 times larger than the largest a-Si:H thickness  $d_{\text{max}} = 30 \text{ nm}$  applied to the symmetric-COSIMA cells. Absorption of light in the front a-Si:H layer is therefore negligible for  $\lambda > 600 \text{ nm}$ .

The IQE measurement shown in Figure 8.6 covers two regimes: In the **short-wavelength range**  $\lambda < 600 \text{ nm}$ , the penetration depth is  $\alpha^{-1} \leq d_{\text{max}}$ . The IQE in this range is sensitive to both, absorption of the incident light in the front a-Si:H

layer, and to carrier recombination at the emitter surface. In the **long-wavelength range**  $\lambda > 600$  nm, the penetration depth is  $\alpha^{-1} \gg d_{\max}$ . The *IQE* in this range is therefore only sensitive to carrier recombination at the emitter surface.

The qualitative analysis of the *IQE* in the short- and long-wavelength range allows to separate the impact of surface passivation and absorption by the different front-a-Si:H films, on the performance of the cells:

- In the **long-wavelength range**  $\lambda > 600$  nm, cells with  $d \geq 10$  nm exhibit an almost optimum internal quantum efficiency  $IQE \approx 1$ . In contrast, cells with thinner front a-Si:H films,  $d \leq 5$  nm, show an *IQE* that is reduced by 5%.

The increase of the long-wavelength *IQE* with increasing a-Si:H thickness  $d$ , is explained by the emitter surface recombination velocity being a function of  $d$ , as shown in Section 4.2.2: The quality of the emitter passivation increases with increasing thickness  $d$ , until the optimum surface passivation is achieved for  $d \geq 6.5$  nm. The long-wavelength *IQE* is therefore optimum for the cells with  $d = 10, 15,$  and  $30$  nm, while it is reduced by the increased carrier recombination at the emitter surface for cells with  $d = 1.5$  and  $5$  nm. This explanation agrees with the results obtained from the measurements of the open-circuit voltage shown above.

- In the **short-wavelength range**  $\lambda < 600$  nm, the *IQE* is determined by both, carrier recombination at the emitter surface, and absorption of light in the a-Si:H layer. The short-wavelength quantum efficiency of the optimally passivated cells with  $d \geq 10$  nm therefore decreases with increasing layer thickness  $d$ , due to the increasing absorption of the incident light within the a-Si:H film. However, the benefit of less absorption with decreasing  $d$  is almost compensated by the increasing emitter saturation current density in the range  $d \leq 5$  nm.

### Comparison to current-voltage characteristics

Figure 8.7 shows the short-circuit current density  $J_{sc,short}$  that is collected in the short-wavelength range  $300 \text{ nm} \leq d \leq 750 \text{ nm}$ , as compared to the short-circuit current density  $J_{sc}$  that is obtained from the current-voltage characteristics of the non-textured symmetric-COSIMA cells. The short-circuit current density is calculated from the internal quantum efficiency,

$$J_{sc,short} = q \int_{300 \text{ nm}}^{750 \text{ nm}} IQE(\lambda) \Phi_{\text{AML.5G}}(\lambda) d\lambda, \quad (8.6)$$

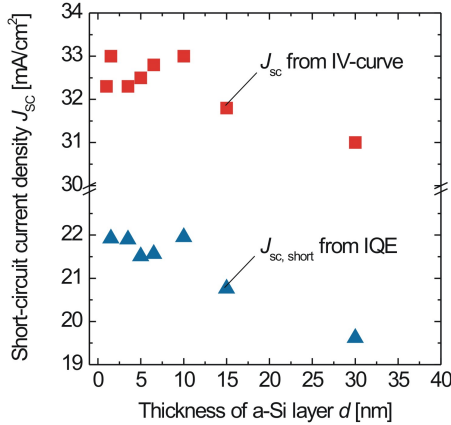


Figure 8.7: Short-circuit current density  $J_{sc}$  of non-textured symmetric-COSIMA solar cells. The current density  $J_{sc,short}$  is calculated by Equation 8.6, from the short-wavelength IQE shown in Figure 8.6. Both currents show the same absolute decrease with increasing  $d$ .

where  $\Phi_{AM1.5G}$  is the photon flux defined by the AM1.5G-spectrum.

The calculated short-wavelength short-circuit current  $J_{sc,short}$  shows the same absolute decrease as  $J_{sc}$ . It is therefore apparent that the decrease of the short circuit current for  $d \geq 10$  nm is due to the increasing absorption of the incident light in the front a-Si:H film, with increasing thickness of the a-Si:H film. The short-circuit current does not depend on the thickness  $d$  if  $d \leq 10$  nm, because the benefit of less absorption with decreasing  $d$  is almost compensated by the increasing emitter saturation current density, as shown above.

In conclusion, the change of the electrical and optical properties of the passivating a-Si:H film with its thickness  $d$ , determines how the short-circuit current density  $J_{sc}$  varies with varying layer thickness. The maximum cell efficiency is obtained in the range of  $5 \text{ nm} < d < 10 \text{ nm}$ , where both  $V_{oc}$  and  $J_{sc}$  are maximum due to a low emitter saturation current density, and low absorption within the front a-Si:H layer.



### 8.2.3 Front-textured symmetric-COSIMA solar cells

Figure 8.8 shows the current-voltage characteristics of the best symmetric-COSIMA solar cell with a textured front side, under standard testing conditions ( $25^{\circ}\text{C}$ ,  $100\text{ mW}/\text{cm}^2$ ).

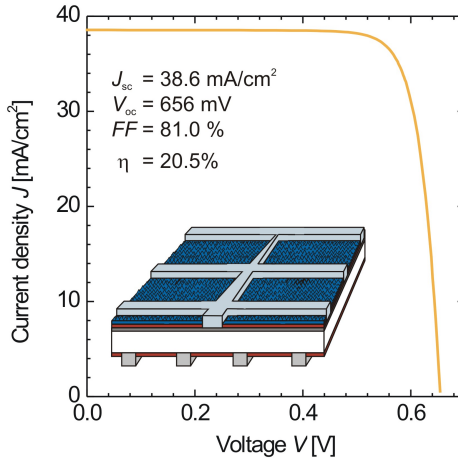


Figure 8.8: *Current-voltage characteristics of the best symmetric-COSIMA solar cell. The energy conversion efficiency is 20.5% under standard test conditions ( $25^{\circ}\text{C}$ ,  $100\text{ mW}/\text{cm}^2$ , AM1.5 global). The cell area is  $4\text{ cm}^2$ .*

The short-circuit current density is  $J_{\text{sc}} = 38.6\text{ mA}/\text{cm}^2$ , and the open-circuit voltage  $V_{\text{oc}} = 655\text{ mV}$ . The energy conversion efficiency is  $\eta = 20.5\%$ . The high fill factor of  $FF = 81\%$  of the a-Si:H-passivated cell demonstrates the low resistivity of the COSIMA contacts to both, the emitter and the base.

The lumped series resistance,  $R_s = (0.4 \pm 0.05)\ \Omega\text{cm}^2$  in maximum power point conditions, is obtained from the voltage shift between the dark- and the illuminated-current-voltage curve after Reference [127]. The obtained value of  $R_s$  is the same as for the rear-COSIMA-cells shown in Section 8.1. Since both kinds of cells feature the same rear side, it is concluded that the resistivity of the COSIMA-emitter contacts must be the same as for the Ti/Pd/Ag-emitter contacts applied to the rear-COSIMA cells. This result confirms the analysis of the COSIMA- and Ti/Pd/Ag-contact resistivities shown in Section 3.2.3.

The solar cells shown in this Section did not exhibit any degradation of their current-voltage characteristics during storage under indoor illumination for six months. It was already mentioned in Section 8.1.4 that the effective SRV of the a-Si:H passivated base of the cells is in the same range,  $S_{\text{pass}} = (30 \pm 15) \text{ cm/s}$  that was obtained *after* the light-induced Staebler-Wronski degradation of lifetime samples as shown in Section 6.1. It is therefore concluded that the amorphous silicon films that were applied for surface passivation, were already in their stable, degraded state after fabrication of the COSIMA solar cells.

### 8.3 Conclusion

The COSIMA technique combines high-quality surface passivation of c-Si solar cells with a low process temperature,  $T_{\text{max}} \leq 325^\circ\text{C}$  even for contact formation. An independently confirmed energy conversion efficiency of 20.1% under one-sun standard testing conditions is achieved with a rear-COSIMA solar cell. This is the highest confirmed efficiency for a homojunction crystalline silicon solar cell with a-Si:H-passivated base.

Rear-COSIMA solar cells exhibit an enhanced infrared response when compared to cells with a  $\text{SiN}_x$ -passivated rear side. This result is shown to be due to the lower effective SRV of the a-Si:H-passivated base. In case of  $\text{SiN}_x$  single-layer passivation of the base, shunting of the charge-induced inversion layer and the base contacts leads to a significantly larger recombination rate than with a-Si:H passivation.

The symmetric-COSIMA technique of applying a-Si:H passivation and contact formation by annealing at low temperatures to both, the emitter and the base, yields high efficiencies in a simple process. The optimum thickness of the front-side a-Si:H film is in the range of  $5 \text{ nm} < d < 10 \text{ nm}$ , to allow for maximum open-circuit voltage and short-circuit current of the cells. Absorption within the amorphous silicon is minimized. An efficiency of 20.5% under one-sun standard testing conditions is achieved with a symmetric-COSIMA solar cell that features a 6.5 nm-thick a-Si:H passivation on the front side.

## 9 Summary

The deposition of intrinsic, hydrogenated amorphous silicon (a-Si:H) allows for the same excellent passivation of crystalline (c-Si) silicon surfaces as thermal oxidation, that is applied as a standard process both in the microelectronics industry, and for the fabrication of high-efficiency solar cells. Furthermore, the application of a-Si:H for surface passivation of c-Si devices has the advantage of a lower process temperature ( $T < 250^\circ\text{C}$ ) when compared to thermal oxidation ( $T \approx 1000^\circ\text{C}$ ). Surface passivation by a-Si:H therefore reduces the energy consumption and risk of impurity diffusion into the bulk material.

Whereas the high quality of a-Si:H-passivation of lowly-doped c-Si surfaces is described in literature, this work showed the first-time surface passivation of highly-doped c-Si by amorphous silicon. The focus lay on the characterization of recombination centers at the a-Si:H/c-Si interface, in particular on the quantitative analysis of their formation and passivation during illumination and thermal annealing. Surface passivation by a-Si:H of both, the highly-doped emitter and the lowly-doped base were implemented in the fabrication of solar cells exceeding an efficiency of 20%.

Applying a-Si:H passivation to the illuminated emitter surface of solar cells required both, the minimization of parasitic absorption within the a-Si:H layer, and its combination with an anti reflective coating. A double-layer passivation scheme was therefore developed, that comprised a thin a-Si:H film for surface passivation, and an anti reflective silicon nitride ( $\text{SiN}_x$ ) capping layer on top of the a-Si:H film. The minimum nominal thickness  $d = 6.5$  nm of the a-Si:H film ensured that pin-holes were closed, thus allowing for the optimum surface passivation. The effective surface recombination velocity (SRV) as extracted from quasi-steady state photo-conductance measurements, was  $S_{\text{eff}} < 5$  cm/s for both, lowly-doped  $n$ - and  $p$ -type c-Si with a resistivity of  $1.5 \Omega\text{cm}$ , and diffused  $n^+$ - and  $p^+$ -type emitters with a surface dopant concentration of  $(2 \dots 3) \times 10^{19} \text{ cm}^{-3}$ . The first-time successful passivation of diffused emitters by a-Si:H was thus shown.

A comparison of the injection-dependent effective SRV of lowly-doped c-Si wafers featuring a-Si:H single-layer passivation and a-Si:H/ $\text{SiN}_x$  double layer passivation, showed that the  $\text{SiN}_x$  capping layer had no influence on the recombination characteristics. Analysis of the short-wavelength quantum efficiency and current-voltage characteristics of solar cells with an a-Si:H-passivated emitter on the illuminated

front side, revealed an optimum thickness of the front-side a-Si:H film in the range of  $6.5 \text{ nm} \leq d < 10 \text{ nm}$ . Absorption within the amorphous silicon was thus minimized, while ensuring the optimum surface passivation.

An analytic model was derived for the distribution functions and capture cross sections of recombination centers, both in the a-Si:H bulk and at the a-Si:H/c-Si interface. This model was used to obtain the densities of dangling bonds  $N_{\text{DB}}$  in the bulk, and  $D_{\text{it}}$  at the interface, by fitting the measured injection-dependent surface recombination velocities (SRV) of a-Si:H passivated wafers with the device simulation software AFORS-HET. Calculations of the depth-resolved recombination rate showed that the effective SRV is controlled by both, carrier recombination through interface defects and recombination through a-Si:H bulk defects. However, transport of excess carriers across the band edge offsets from c-Si to a-Si:H controls the carrier recombination rate within the a-Si:H layer. High defect densities are thus allowed in the a-Si:H bulk while still maintaining the excellent surface passivation.

A slight increase of the effective SRV of a-Si:H-passivated c-Si wafers was observed during low-intensity illumination in the visible spectrum. The passivation reached a stable state with  $S_{\text{eff}} = (14 \pm 5) \text{ cm/s}$  at  $\Delta n = 10^{15} \text{ cm}^{-3}$  after 15 months of illumination, and fully recovered to the initial state with  $S_{\text{eff}} = (3.5 \pm 0.6) \text{ cm/s}$  by annealing at  $300^\circ\text{C}$ . Fitting the defect model to the experimental data revealed that both, the density of the interface dangling bonds and the density of the dangling bonds in the a-Si:H bulk, increased by about an order of magnitude during the 15 months of illumination. This reversible light-degradation of the a-Si:H surface passivation was explained by the formation of dangling bond states due to the dissociation of weak Si-Si bonds, in analogy to the Staebler-Wronski effect.

Annealing of a-Si:H-passivated c-Si wafers at  $300^\circ\text{C}$  maintained the excellent passivation quality of as-deposited samples, and restored their passivation after illumination. In contrast, annealing at temperatures larger than  $400^\circ\text{C}$  led to an increase of the bulk and interface defect densities, thus degrading the surface passivation. This behavior was explained by the temperature-dependence of the diffusivity of hydrogen within the amorphous silicon: Annealing at low temperatures  $T \approx 300^\circ\text{C}$ , allowed for the re-arrangement of Si-H bonds, thus reducing the density of dangling bonds when compared to the illuminated state. Upon annealing at higher temperatures,  $T \geq 400^\circ\text{C}$ , the creation of dangling bonds at the interface and in the a-Si:H bulk due to hydrogen desorption, led to the observed degradation of the surface passivation.

Applying an anti reflective  $\text{SiN}_x$  capping layer on top of the passivating a-Si:H layer enhanced the thermal stability of the passivation, because the  $\text{SiN}_x$  layer acted as a source of additional hydrogen atoms that diffused freely within the double layer structure. Fitting the defect model to reproduce the measured surface

recombination velocities, showed that the formation rate of dangling bonds during annealing at 500°C was by a factor of 15 lower for a-Si:H/SiN<sub>x</sub> double-layer passivated samples, than for a-Si:H single-layer passivated samples.

The COSIMA technique (contact formation to a-Si:H-passivated solar cells by means of annealing) which was developed in this work, comprised (i) the deposition of an amorphous silicon film onto the emitter and/or the base of a solar cell, for surface passivation, and (ii) the deposition and annealing of aluminum, for the formation of local contacts.

Transmission electron microscopy and energy-dispersive x-ray analysis of the elemental composition of the Al/c-Si interface region showed that the a-Si:H film below the local Al contacts dissolves in the aluminum during annealing. The resistivities of COSIMA contacts to the lowly-doped base and the highly-doped emitter were the same, or even lower than values that were obtained for reference samples processed without the a-Si:H interlayer. No lateral diffusion of Al atoms occurred within the amorphous silicon film, so the passivation of the non-metalized fraction of the solar cell surface was not affected by the contact-annealing step.

A model was derived that allowed to analytically calculate the base saturation current density  $J_{0b}$  of solar cells featuring a passivated, locally contacted base, in order to optimize the contact layout for a maximum energy conversion efficiency. The model was experimentally verified for technologically relevant contact spacings  $1\text{ mm} \leq p \leq 5\text{ mm}$ , and contact coverages  $0 \leq f \leq 1$ , by extracting the base saturation current density of COSIMA-processed c-Si wafers with dot- and stripe-like contact geometries from measurements of their effective carrier lifetime.

Rear-COSIMA solar cells exhibited an enhanced infrared quantum efficiency when compared to cells with a SiN<sub>x</sub>-passivated rear side, due to the better passivation of the base by amorphous silicon compared to silicon nitride. In case of SiN<sub>x</sub> single-layer passivation of the base, shunting of the charge-induced inversion layer and the base contacts led to a significantly larger recombination rate than with a-Si:H passivation. The different infrared quantum efficiency of both cell types explained their different current-voltage characteristics.

An independently confirmed energy conversion efficiency of 20.1% under one-sun standard testing conditions was achieved with a rear-COSIMA solar cell. This was the highest confirmed efficiency for a homojunction crystalline silicon solar cell with a-Si:H-passivated base.

The symmetric-COSIMA technique of applying a-Si:H passivation and contact formation by annealing at low temperatures to both, the emitter and the base, yielded high efficiencies in a simple process. An efficiency of 20.5% was achieved under one-sun standard testing conditions with a symmetric-COSIMA solar cell that featured a-Si:H/SiN<sub>x</sub> double-layer passivation, in its stable state after illumination-

induced degradation.

The suitability of a-Si:H films for the surface passivation of both, the emitter and the base of high-efficiency solar cells at low temperatures was thus shown. Furthermore, the improved understanding of the formation and passivation processes for a-Si:H/c-Si interface defects provided by this work was implemented for developing the a-Si:H/SiN<sub>x</sub> double layer passivation scheme that shows improved thermal stability and optical properties.

## References

- [1] B. Lenkeit, *Elektronische und strukturelle Eigenschaften von Plasma-Siliziumnitrid zur Oberflächenpassivierung von siebgedruckten, bifazialen Silizium-Solarzellen*, PhD thesis, University of Hannover (2002). (Papierflieger Verlag) pp. 170-175.
- [2] S. Dauwe, L. Mittelstädt, A. Metz, and R. Hezel, Experimental evidence of parasitic shunting in silicon nitride rear surface passivated solar cells, *Prog. Photovolt.: Res. Appl.* **10**, 271 (2002).
- [3] S. Dauwe, J. Schmidt, and R. Hezel, Very low surface recombination velocities on p- and n-type silicon wafers passivated with hydrogenated amorphous silicon films, *Proc. 29th IEEE PVSC*, p. 1246 (2002).
- [4] H. Takakura, K. Miyagi, T. Kanata, H. Okamoto, and Y. Hamakawa, Device physics and optimum design of a-Si/poly-Si tandem solar cells, *Proc. 4th Int. PVSEC*, p. 403 (1989).
- [5] A. Terakawa, T. Asaumi, S. Kobayashi, Y. Tsunomura, T. Yagiura, M. Taguchi, Y. Yoshimine, H. Sakata, E. Maruyama, and M. Tanaka, High efficiency hit<sup>tm</sup> solar cells and the effects of open circuit voltage on temperature coefficients, *Proc. 15th Int. PVSEC*, p. 661 (2005).
- [6] A. Hübner, A.G. Aberle, and R. Hezel, Novel cost-effective bifacial silicon solar cells with 19.4% front and 18.1% rear efficiency, *Appl. Phys. Lett.* **70**, 1008 (1997).
- [7] P.P. Altermatt, A. Schenk, F. Geelhaar, and G. Heiser, Reassessment of the intrinsic carrier density in crystalline silicon in view of band-gap narrowing, *Appl. Phys. Lett.* **93**, 1598 (2003).
- [8] A.B. Sproul, M.A. Green, and A.W. Stephens, Accurate determination of minority carrier- and lattice scattering-mobility in silicon from photoconductance decay, *J. Appl. Phys.* **72**, 4161 (1992).

- [9] H. Schlangenotto, H. Maeder, and W. Gerlach, Temperature dependence of the radiative recombination coefficient in silicon, *Phys. Stat. Sol. A* **21**, 357 (1974).
- [10] J. Dzewior and W. Schmid, Auger coefficients for highly doped and highly excited silicon, *Appl. Phys. Lett.* **31**, 346 (1977).
- [11] M.J. Kerr and A. Cuevas, General parameterization of Auger recombination in crystalline silicon, *J. Appl. Phys.* **91**, 2473 (2002).
- [12] W. Shockley and W.T. Read, Statistics of the recombination of electrons and holes, *Phys. Rev.* **87**, 835 (1952).
- [13] R.N. Hall, Electron-hole recombination in germanium, *Phys. Rev.* **87**, 387 (1952).
- [14] M.A. Green, Intrinsic concentration, effective density of states, and effective mass in silicon, *J. Appl. Phys.* **67**, 2944 (1990).
- [15] I.E. Tamm, Über eine mögliche Art der Elektronenbindung an Kristalloberflächen, *Physik. Z. Sowjetunion* **1**, 733 (1932).
- [16] W. Shockley, On the surface states associated with a periodic potential, *Phys. Rev.* **56**, 317 (1939).
- [17] W. Mönch. *Semiconductor surfaces and interfaces*, chapter 9 and 14. Springer series in surface science. Springer-Verlag, Berlin/Heidelberg, 3rd Edition, (2001).
- [18] R.B.M. Girisch, R.P. Mertens, and R.F. de Keersmaecker, Determination of the Si – SiO<sub>2</sub> interface recombination parameters using a gate-controlled point-junction diode under illumination, *IEEE Trans. Electron. Devices* **35**, 203 (1988).
- [19] S. Dauwe, *Low-temperature surface passivation of crystalline silicon and its application to the rear side of solar cells*, PhD thesis, University of Hanover (2004).
- [20] R. Stangl, M. Kriegel, and M. Schmidt, AFORS – HET, version 2.2, A numerical simulation program for simulation of heterojunction solar cells and measurements, *Proc. 4th World PVSEC, Hawaii* p. 1350 (2006).
- [21] H. Nagel, C. Berge, and A.G. Aberle, Generalized analysis of quasi-steady-state and quasi-transient measurements of carrier lifetimes in semiconductors, *J. Appl. Phys.* **86**, 6218 (1999).



- [22] R. Sinton and A. Cuevas, Contactless determination of current-voltage characteristics and minority carrier lifetimes in semiconductors from quasi-steady state photoconductance data, *Appl. Phys. Lett.* **69**, 2510 (1996).
- [23] R. Brendel, Note on the interpretation of injection-level-dependent surface recombination velocities, *Appl. Phys. A* **60**, 523 (1995).
- [24] J. Schmidt, Measurement of differential and actual recombination parameters on crystalline silicon wafers, *IEEE Trans. Electron. Devices* **46**, 2018 (1999).
- [25] B. Fischer, *Loss analysis of crystalline silicon solar cells using photoconductance and quantum efficiency measurements*, PhD thesis, University of Konstanz (2003). (Cuvillier Verlag) Chapter 4.
- [26] M. Bail, *Ladungsträger-Lebensdauer in kristallinem Silicium für die Photovoltaik*, PhD thesis, University of Erlangen (2002).
- [27] R. Schropp and M. Zeman. *A-Si and  $\mu\text{-Si}$  Solar Cells*, p. 183. Kluwer Academic Publishers, (1998).
- [28] M. Schmidt, A. Schoepke, O. Milch, T. Lussky, and W. Fuhs, Photoelectron spectroscopic investigations of very thin a-Si : H layers, *Mat. Res. Soc. Symp. Proc.* **762**, 125 (2003).
- [29] K. Tanaka, E. Maruyama, T. Shimada, and H. Okamoto. *Amorphous Silicon*, 124–126. John Wiley & Sons, Chichester, (1999).
- [30] K.L. Luke and L.J. Cheng, Analysis of the interaction of a laser pulse with a silicon wafer: Determination of bulk lifetime and surface recombination velocity, *J. Appl. Phys.* **61**, 2282 (1987).
- [31] G.S. Kousik, Z.G. Ling, and P.K. Ajmera, Nondestructive technique to measure bulk lifetime and surface recombination velocities at the two surfaces by infrared absorption due to pulsed optical excitation, *J. Appl. Phys.* **72**, 141 (1992).
- [32] M. Schöfthaler, *Transiente Mikrowellenreflexion zur kontaktlosen Trägerlebensdauer an Silizium für Solarzellen*, PhD thesis, University of Stuttgart (1995). (Shaker Verlag).
- [33] A.B. Sproul, Dimensionless solution of the equation describing the effect of surface recombination on carrier decay in semiconductors, *J. Appl. Phys.* **76**, 2851 (1994).

- [34] P.P. Altermatt, G. Heiser, A.G. Aberle, A. Wang, J. Zhao, S.R. Robinson, S. Bowden, and M.A. Green, Spatially resolved analysis and minimization of resistive losses in high-efficiency Si solar cells, *Prog. Photovolt.: Res. Appl.* **4**, 399 (1996).
- [35] M.A. Green. *Solar Cells*, chapter 4. University of New South Wales, (1992).
- [36] A.L. Fahrenbruch and R.H. Bube. *Fundamentals of solar cells*. Academic Press, New York, (1983).
- [37] D.E. Kane and R.M. Swanson, Measurement of the emitter saturation current by a contactless photoconductivity decay method, *Proc. 18th IEEE PVSC*, p. 578 (1985).
- [38] A. Cuevas, The effect of emitter recombination on the effective lifetime of silicon wafers, *Sol. En. Mat.* **57**, 277 (1999).
- [39] P.P. Altermatt, J.O. Schumacher, A. Cuevas, M.J. Kerr, S.W. Glunz, R.R. King, G. Heiser, and A. Schenk, Numerical modeling of highly doped Si : P emitters based on fermi–dirac statistics and self-consistent material parameters, *J. Appl. Phys.* **92**, 3187 (2002).
- [40] M.V. Fischetti, Effect of the electron-plasmon interaction on the electron mobility in silicon, *Phys. Rev. B* **44**, 5527 (1991).
- [41] SENTAURUS, Synopsys Inc. Mountain View CA, [www.synopsys.com/products/tcad/tcad.html](http://www.synopsys.com/products/tcad/tcad.html), ()
- [42] B. Lenkeit, *Elektronische und strukturelle Eigenschaften von Plasma-Siliziumnitrid zur Oberflächengenpassivierung von siebgedruckten, bifazialen Silizium-Solarzellen*, PhD thesis, University of Hannover (2002). (Papierflieger Verlag) pp. 91-94.
- [43] F. Shimura. *Semiconductor crystalline silicon technology*, p. 149. Academic Press, San Diego, (1989).
- [44] J. Zhao, A. Wang, and M.A. Green, Recent advances of high-efficiency single crystalline silicon solar cells in processing technologies and substrate materials, *Prog. Photovolt.: Res. Appl* **7**, 471 (1999).
- [45] A.W. Blakers, A. Wang, A.M. Milne, J. Zhao, and M.A. Green, 22.8% efficient silicon solar cell, *Appl. Phys. Lett.* **55**, 1363 (1989).

- [46] G. Heiser, P.P. Altermatt, A. Williams, A. Sproul, and M.A. Green, Optimisation of rear contact geometry of high-efficiency silicon solar cells using three dimensional numerical modelling, *Proc. 13th EU-PVSEC*, p. 447 (1995).
- [47] K.R. Catchpole and A.W. Blakers, Modelling of the PERC structure with stripe and dot back contacts, *Proc. 16th EU-PVSEC*, p. 1719 (2000).
- [48] U. Rau, Three dimensional simulation of the electrical transport in high-efficiency solar cells, *Proc. 12th EU-PVSEC*, p. 1350 (1994).
- [49] B. Fischer, *Loss analysis of crystalline silicon solar cells using photoconductance and quantum efficiency measurements*, PhD thesis, University of Konstanz (2003). (Cuvillier Verlag) Chapter 2.3.
- [50] P. Basore, Extended spectral analysis of internal quantum efficiency, *Proc. 23rd IEEE PVSC*, p. 147 (1993).
- [51] M. Schöfthaler, U. Rau, and J.H. Werner, Direct observation of the scaling effect on effective minority carrier lifetimes, *J. Appl. Phys.* **76**, 4168 (1994).
- [52] R.D. Brooks and H.G. Mattes, Spreading resistance between constant potential surfaces, *Bell Sys. Techn. J.* **50**, 775 (1971).
- [53] K. Kotsovos and K. Misiakos, Three-dimensional simulation of carrier transport effects in the base of rear point contact silicon solar cells, *J. Appl. Phys.* **89**, 2491 (2001).
- [54] B. Gelmont and M. Shur, Spreading resistance of a round ohmic contact, *Sol. State El.* **36**, 143 (1993).
- [55] B. Gelmont, M. Shur, and R.J. Mattauch, Disk and stripe capacitances, *Sol. State El.* **38**, 731 (1995).
- [56] I.S. Gradshteyn and I.M. Ryzhik. *Tables of Integrals, Series and Products*, p. 905. Academic Press, New York, (1983).
- [57] T. Lauinger, J.D. Moschner, A.G. Aberle, and R. Hezel, Optimization and characterization of remote plasma-enhanced chemical vapor deposition silicon nitride for the passivation of p-type crystalline silicon surfaces, *J. Vac. Sci. Technol. A* **16**, 530 (1998).
- [58] B. Lenkeit, *Elektronische und strukturelle Eigenschaften von Plasma-Siliziumnitrid zur Oberflächenpassivierung von siebgedruckten, bifazialen Silizium-Solarzellen*, PhD thesis, University of Hannover (2002). (Papierflieger Verlag) pp. 18-19.

- [59] K. Tanaka, E. Maruyama, T. Shimada, and H. Okamoto. *Amorphous Silicon*, 85–89. John Wiley & Sons, Chichester, (1999).
- [60] T. Shimizu, K. Nakazawa, M. Kumeda, and S. Ueda, Incorporation scheme of H reducing defects in a-Si studied by NMR and ESR, *Physica B* **117/118**, 926 (1983).
- [61] M. Tosolini, L. Colombo, and M. Peressi, Atomic-scale model of c-Si/a-Si:h interfaces, *Phys. Rev. B* **69**, 075301–1 (2004).
- [62] S.J. Pearton, J.W. Corbett, and M. Stavola. *Hydrogen in Crystalline Semiconductors*. Springer series in materials science 16. Springer-Verlag, (1992).
- [63] M.J. Kerr, *Surface, emitter and bulk recombination in silicon and development of silicon nitride passivated solar cells*, PhD thesis, Australian National University (2002).
- [64] J.D. Moschner, J. Henze, J. Schmidt, and R. Hezel, High-quality surface passivation of silicon solar cells in an industrial-type inline plasma silicon nitride deposition system, *Prog. Photvolt: Res. Appl.* **12**, 21 (2004).
- [65] T. Lauinger, J. Schmidt, A.G. Aberle, and R. Hezel, Record low surface recombination velocities on 1 ohmcm p-silicon using remote plasma silicon nitride passivation, *Appl. Phys. Lett.* **68**, 1232 (1996).
- [66] M.J. Kerr and A. Cuevas, Recombination at the interface between silicon and stoichiometric plasma silicon nitride, *Semicond. Sci. Technol.* **17**, 166 (2002).
- [67] S.W. Glunz, A. Grohe, M. Hermle, M. Hofmann, S. Janz, T. Roth, O. Schultz, M. Vetter, I. Martin, R. Ferre, S. Barmejo, W. Wolke, W. Warta, R. Preu, and G. Willeke, Comparison of different dielectric passivation layers for application in industrially feasible high-efficiency crystalline silicon solar cells, *Proc. 20th EU-PVSEC*, p. 814 (2005).
- [68] J.L. Murray and A.J. McAllister, The Al-Si (aluminum-silicon) system, *Bull. Alloy Phase Diagrams* **5**, 74 (1984).
- [69] O. Nast, T. Puzzer, L.M. Koschier, A.B. Sproul, and S.R. Wenham, Aluminum-induced crystallization of amorphous silicon on glass substrates above and below the eutectic temperature, *Appl. Phys. Lett.* **73**, 3214 (1998).
- [70] O. Nast and S.R. Wenham, Elucidation of the layer exchange mechanism in the formation of polycrystalline silicon by aluminum-induced crystallization, *J. Appl. Phys.* **88**, 124 (2000).

- [71] S. Gall, M. Muske, I. Sieber, O. Nast, and W. Fuhs, Aluminum-induced crystallization of amorphous silicon, *J. Non-Cryst. Sol.* **299-302**, 741 (2002).
- [72] C. Ornaghi, G. Beaucarne, J. Poortmans, J. Nijs, and R. Mertens, Aluminum-induced crystallization of amorphous silicon: influence of material characteristics on the reaction, *Thin Solid Films* **451-452**, 476 (2004).
- [73] M.S. Haque, H.A. Naseem, and W.D. Brown, Interaction of aluminum with hydrogenated amorphous silicon at low temperatures, *J. Appl. Phys.* **75**, 3928 (1993).
- [74] M.S. Haque, H.A. Naseem, and W.D. Brown, Aluminum-induced crystallization and counter-doping of phosphorous-doped hydrogenated amorphous silicon at low temperatures, *J. Appl. Phys.* **79**, 7529 (1996).
- [75] D.K. Schroder. *Semiconductor Material and Device Characterization*, 2nd edition. Wiley, New York, (1998).
- [76] H.H. Berger, Contact resistance and contact resistivity, *J. Electrochem. Soc.* **119**, 507 (1987).
- [77] D.K. Schroder and D.L. Meier, Solar cell contact resistance - a review, *IEEE Trans. Electron. Devices* **31**, 637 (1984).
- [78] M.A. Green, A.W. Blakers, J. Zhao, A.D. Milne, A. Wang, and X. Dai, Characterization of 23-percent efficient silicon solar cells, *IEEE Trans. Electron. Devices* **37**, 331 (1990).
- [79] B. Fischer, *Loss analysis of crystalline silicon solar cells using photoconductance and quantum efficiency measurements*, PhD thesis, University of Konstanz (2003). (Cuvillier Verlag) Chapter 2.4.
- [80] A.G. Aberle, P.P. Altermatt, G. Heiser, S.J. Robinson, A. Wang, J. Zhao, U. Krumbein, and M.A. Green, Limiting loss mechanisms in 23% efficient silicon solar cells, *J. Appl. Phys.* **77**, 3491 (1995).
- [81] M. Stocks, A. Cuevas, and A. Blakers, High efficiency, reduced rear contact area multicrystalline silicon solar cells, *Proc. 14th EU-PVSEC*, p. 766 (1997).
- [82] J. Schmidt, J.D. Moschner, J. Henze, S. Dauwe, and R. Hezel, Recent progress in the surface passivation of silicon solar cells using silicon nitride, *Proc. 19th EU-PVSEC*, p. 391 (2004).
- [83] F.W. Chen, T.A. Li, and J.E. Cotter, Effect of the electron-plasmon interaction on the electron mobility in silicon, *Appl. Phys. Lett.* **88**, 263514 (2006).

- [84] R. Petres, J. Libal, R. Kopecek, R. Ferre, I. Martin, D. Borchert, I. Röver, K. Wambach, and P. Fath, Passivation of  $p^+$ -surfaces by PECVD silicon carbide films - a promising method for industrial silicon solar cell applications, *Proc. 15th Int. PVSEC*, p. 128 (2005).
- [85] E. Peiner, A. Schlachetzki, and D. Krüger, Doping profile analysis in Si by electrochemical capacitance-voltage measurements, *J. Electrochem. Soc.* **142**, 576 (1995).
- [86] A. Bentzen, A. Ulyashin, A. Suphellen, E. Sauar, D. Grambole, D.N. Wright, E.S. Marstein, B.G. Svensson, and A. Holt, Surface passivation of silicon solar cells by amorphous silicon/silicon nitride dual layers, *Proc. 15th Int. PVSEC*, p. 316 (2005).
- [87] P.P. Altermatt, H. Plagwitz, R. Bock, J. Schmidt, R. Brendel, M.J. Kerr, and A. Cuevas, The surface recombination velocity at boron-doped emitters: comparison between various passivation techniques, *Proc. 21st EU-PVSEC*, p. 647 (2006).
- [88] International Electrotechnical Commission Standard IEC61345 for UV tests of PV modules, ().
- [89] P.C.F. DiStefano, T. Frank, G. Angloher, M. Bruckmayer, C. Cozzini, D. Hauff, F. Pröbst, S. Rutzinger, W. Seidel, L. Stodolsky, and J. Schmidt, Textured silicon calorimetric light detector, *J. Appl. Phys.* **94**, 6887 (2003).
- [90] H. Jin, K.J. Weber, and A.W. Blakers, The effect of a post oxidation in-situ nitrogen anneal on silicon surface passivation, *Proc. 4th IEEE WCPEC*, p. 1071 (2006).
- [91] A. Stesmans and V.V. Afanas'ev, Thermally induced interface degradation in (100) and (111) Si/SiO<sub>2</sub> analyzed by electron spin resonance, *J. Vac. Sci. Technol. B* **16**, 3108 (1998).
- [92] P.K. Hurley, B.J. O'Sullivan, F.N. Cubaynes, P.A. Stolk, F.P. Widdershoven, and J.H. Das, Examination of the Si(111)-SiO<sub>2</sub>, Si(110)-SiO<sub>2</sub>, and Si(100)-SiO<sub>2</sub> interfacial properties following rapid thermal annealing, *J. Electrochem. Soc.* **149**, G194 (2002).
- [93] F.M. Schuurmans, A. Schönecker, J.A. Eikelboom, and W.C. Sinke, Crystal-orientation dependence of surface recombination velocity for silicon nitride passivated silicon wafers, *Proc. 25th IEEE PVSC*, volume 149, p. 485 (1996).

- [94] W. Füssel, M. Schmidt, H. Angermann, G. Mende, and H. Flietner, Defects at the Si/SiO<sub>2</sub> interface: their nature and behaviour in technological processes and stress, *Nuclear Instruments and Methods in Physics Research A* **377**, 177 (1996).
- [95] E.H. Nicollian and J.R. Brews. *MOS Physics and Technology*, chapter 7. Wiley, New York, (1982).
- [96] [www.hmi.de/bereiche/se/se1/projects/asicsi/afors-het](http://www.hmi.de/bereiche/se/se1/projects/asicsi/afors-het), ().
- [97] R. Stangl, M. Kriegel, and M. Schmidt, AFORS – HET, a numerical PC-program for simulation of (thin-film) heterojunction solar cells, version 2.0 (open-source on demand), to be distributed for public use, *Proc. 20th EU-PVSEC*, p. 814 (2005).
- [98] J.M. Dorkel and P. Leturcq, Carrier mobilities in silicon semi-empirically related to temperature, doping and injection level, *Solid-State Electron.* **24**, 821 (1981).
- [99] D. Weaire and M.F. Thorpe, Electronic properties of an amorphous solid I. A simple tight-binding theory, *Phys. Rev. B* **4**, 2508 (1971).
- [100] B. von Roedern, L. Ley, and M. Cardona, Photoelectron spectra of hydrogenated amorphous silicon, *Phys. Rev. Lett.* **39**, 1576 (1977).
- [101] K. Winer and L. Ley, Surface states and the exponential valence-band tail in a-Si:h, *Phys. Rev. B* **36**, 6072 (1987).
- [102] B. von Roedern, L. Ley, M. Cardona, and F.W. Smith, Photoemission studies of in situ prepared hydrogenated amorphous silicon films, *Phil. Mag. B* **40**, 433 (1979).
- [103] W.B. Jackson, S.M. Kelso, C.C. Tsai, J.W. Allen, and S.J. Oh, Energy dependence of the optical matrix element in hydrogenated amorphous and crystalline silicon, *Phys. Rev. B* **31**, 5187 (1985).
- [104] K. Tanaka, E. Maruyama, T. Shimada, and H. Okamoto. *Amorphous Silicon*, 104–110. John Wiley & Sons, Chichester, (1999).
- [105] S. Aljishi, J.D. Cohen, S. Jin, and L. Ley, Band tails in hydrogenated amorphous silicon and silicon-germanium alloys, *Phys. Rev. Lett.* **64**, 2811 (1990).
- [106] K. Tanaka, E. Maruyama, T. Shimada, and H. Okamoto. *Amorphous Silicon*, 111–118. John Wiley & Sons, Chichester, (1999).

- [107] M.J. Powell and S.C. Deane, Improved defect-pool model for charged defects in amorphous silicon, *Phys. Rev. B* **48**, 10815 (1993).
- [108] M.J. Powell and S.C. Deane, Defect-pool model and the hydrogen density of states in hydrogenated amorphous silicon, *Phys. Rev. B* **53**, 10121 (1996).
- [109] A. Froitzheim, K. Brendel, L. Elstner, W. Fuhs, K. Kliefoth, and M. Schmidt, Interface recombination in heterojunctions of amorphous and crystalline silicon, *J. Non-Cryst. Solids* **299-302**, 663 (2002).
- [110] K. Tanaka, E. Maruyama, T. Shimada, and H. Okamoto. *Amorphous Silicon*, 187–200. John Wiley & Sons, Chichester, (1999).
- [111] S.R. Elliott, Defect states in amorphous silicon, *Phil. Mag. B* **38**, 325 (1978).
- [112] D. Adler, Density of states in the gap of tetrahedrally bonded amorphous semiconductors, *Phys. Rev. Lett.* **41**, 1755 (1978).
- [113] Y. Bar-Yam and J.D. Joannopoulos, Dangling bonds in a-Si:ZZH, *Phys. Rev. Lett.* **56**, 2203 (1986).
- [114] P.W. Anderson, Model for the electronic structure of amorphous semiconductors, *Phys. Rev. Lett.* **34**, 953 (1975).
- [115] J.E. Northrup, Effective correlation energy of a Si dangling bond calculated with the local-spin-density approximation, *Phys. Rev. B* **40**, 5875 (1989).
- [116] S. Yamasaki, H. Ohkushi, A. Matsuda, K. Tanaka, and J. Isoya, Origin of optically induced electron-spin resonance in hydrogenated amorphous silicon, *Phys. Rev. Lett.* **65**, 756 (1990).
- [117] K. Tanaka, E. Maruyama, T. Shimada, and H. Okamoto. *Amorphous Silicon*, 147–150. John Wiley & Sons, Chichester, (1999).
- [118] M. Sebastiani, L. DiGaspere, G. Capellini, and F. Evangelisti, Low-energy yield spectroscopy as a novel technique for determining band offsets: application to the c-Si(100)/a-Si:h heterostructure, *Phys. Rev. Lett.* **75**, 3352 (1995).
- [119] K. von Maydell, M. Schmidt, L. Korte, A. Laades, E. Conrad, R. Stangl, M. Scherff, and W. Fuhs, Basic electronic properties and optimization of TCO/a-Si:h(n)/c-Si(p) hetero solar cells, *Proc. 31st IEEE PVSC*, p. 1225 (2005).



- [120] A.G. Aberle, S. Glunz, and W. Warta, Impact of illumination level and oxide parameters on Shockley-Read-Hall recombination at the Si-SiO<sub>2</sub> interface, *J. Appl. Phys.* **71**, 4422 (1992).
- [121] D.L. Staebler and C.R. Wronski, Reversible conductivity changes in discharge-produced amorphous Si, *Appl. Phys. Lett.* **31**, 292 (1977).
- [122] M. Stutzmann, W.B. Jackson, and C.C. Tsai, Light-induced metastable defects in hydrogenated amorphous silicon: A systematic study, *Phys. Rev. B* **32**, 23 (1985).
- [123] M. Stutzmann, Annealing of metastable defects in hydrogenated amorphous silicon, *Phys. Rev. B* **34**, 63 (1986).
- [124] C.C. Tsai, M. Stutzmann, and W.B. Taylor, The Staebler-Wronski effect in undoped a-Si:H: Its intrinsic nature and the influence of impurities, *AIP Conference Proceedings* **120**, 242 (1984).
- [125] R.A. Street, J. Kakalios, C.C. Tsai, and T.M. Hayes, Thermal-equilibrium processes in amorphous silicon, *Phys. Rev. B* **35**, 1316 (1987).
- [126] A. Hübner, A.G. Aberle, and R. Hezel, 20% efficient bifacial silicon solar cells, *Proc. 14th EU-PVSEC*, p. 92 (1997).
- [127] A.G. Aberle, S.R. Wenham, and M.A. Green, A new method for accurate measurements of the lumped series resistance of solar cells, *Proc. 23rd IEEE PVSC*, p. 133 (1993).
- [128] M. Hübner, U. Rau, and J.H. Werner, Analysis of internal quantum efficiency and a new graphical evaluation scheme, *Sol. State El.* **38**, 1009 (1995).
- [129] P.A. Basore, Extended spectral analysis of internal quantum efficiency, *Proc. 23rd IEEE PVSC*, p. 147 (1993).
- [130] K. Tanaka, E. Maruyama, T. Shimada, and H. Okamoto. *Amorphous Silicon*, 118–124. John Wiley & Sons, Chichester, (1999).



## List of symbols and acronyms

Symbol	Unit	Description
$a$	$\mu\text{m}$	Width of contact stripes
$B$	$\text{cm}^3 \text{s}^{-1}$	Coefficient of radiative recombination
$C_n, C_p$	$\text{cm}^6 \text{s}^{-1}$	Auger coefficients for electrons and holes
$\Delta E_V, \Delta E_C$	$\text{meV}$	Valence- and conduction-band offsets
$\Delta n, \Delta p$	$\text{cm}^{-3}$	Excess electron and hole density
$\Delta n_s$	$\text{cm}^{-3}$	Excess electron density at the surface
$\Delta n_b$	$\text{cm}^{-3}$	Excess electron density in the bulk
$d$	$\text{nm}$	Thickness of a-Si:H films
$D_{it}$	$\text{cm}^{-2}$	Interface density of states
$D_a$	$\text{cm}^2 \text{s}^{-1}$	Ambipolar diffusion coefficient
$D_n, D_p$	$\text{cm}^2 \text{s}^{-1}$	Diffusion coefficients for electrons and holes
$\eta$	%	Energy conversion efficiency
$\eta_{\text{text.}}, \eta_{\text{planar}}$	1	Efficiency of surface passivation
$E$	$\text{eV}$	Energy
$E_V, E_C$	$\text{eV}$	Energy level of valence-/conduction-band edges
$E_F$	$\text{eV}$	Fermi level
$E_g$	$\text{eV}$	Bandgap energy
$f$	%	Contact coverage
$FF$	%	Fill factor
$G$	$\text{cm}^{-3} \text{s}^{-1}$	Carrier generation rate
$I$	$\text{mA}$	Current
$J$	$\text{mA cm}^{-2}$	Current density
$J_0$	$\text{fA cm}^{-2}$	Diode saturation current density
$J_{0e}, J_{0b}$	$\text{fA cm}^{-2}$	Contributions of emitter and base to $J_0$
$J_L$	$\text{mA cm}^{-2}$	Photogenerated current density
$J_{sc}$	$\text{mA cm}^{-2}$	Short-circuit current density
$k$	$8.62 \times 10^{-5} \text{ eV K}^{-1}$	Boltzmann constant
$\lambda$	$\text{nm}$	Wavelength
$l$	$\text{mm}$	Length of contact stripes

Symbol	Unit	Description
$L_b$	$\mu\text{m}$	Carrier diffusion length in the bulk
$L_{\text{eff}}$	$\mu\text{m}$	Effective carrier diffusion length
$m$	1	Diode ideality factor
$n$	$\text{cm}^{-3}$	Electron concentration
$n_0$	$\text{cm}^{-3}$	Electron concentration in thermal equilibrium
$n_i$	$\text{cm}^{-3}$	Intrinsic carrier concentration
$n$	1	Refractive index
$N_{\text{dop}}$	$\text{cm}^{-3}$	Dopant concentration
$N_A, N_D$	$\text{cm}^{-3}$	Acceptor and donor concentration
$N_{\text{DB}}$	$\text{cm}^{-3}$	Bulk density of dangling bonds
$N_{\text{occ}}$	$\text{cm}^{-3}$	Occupied bulk density of states
$p$	mm	Period length of contact layouts
$p$	$\text{cm}^{-3}$	Hole concentration
$p_0$	$\text{cm}^{-3}$	Hole concentration in thermal equilibrium
$q$	$e = 1.6 \times 10^{-19} \text{ As}$	Elementary charge
$\rho$	$\Omega \text{ cm}$	Resistivity
$\rho_c$	$\text{m}\Omega \text{ cm}^2$	Contact resistivity
$\rho_{\text{sheet}}$	$\Omega/\square$	Sheet resistivity
$r$	$\mu\text{m}$	Radius of contact dots
$R$	1	Reflectivity
$R_b$	$\Omega \text{ cm}^2$	Base series resistance
$R_s$	$\Omega \text{ cm}^2$	Series resistance
$R_{\text{spread}}$	$\Omega$	Spreading resistance
$\sigma$	$\text{cm}^2$	Capture cross section
$S$	$\text{cm/s}$	Surface recombination velocity
$S_{\text{eff}}$	$\text{cm/s}$	Effective surface recombination velocity
$S_f, S_r$	$\text{cm/s}$	Front and rear surface recombination velocities
$\tau$	$\mu\text{s}$	Carrier lifetime
$\tau_{\text{Auger}}$	$\mu\text{s}$	Carrier lifetime due to Auger recombination
$\tau_{\text{eff}}$	$\mu\text{s}$	Effective carrier lifetime
$\tau_{\text{SRH}}$	$\mu\text{s}$	Carrier lifetime due to SRH recombination
$\tau_s$	$\mu\text{s}$	Carrier lifetime due to surface recombination
$t$	s	Time
$T$	$^\circ\text{C}$	Temperature
$T_{\text{dep}}$	$^\circ\text{C}$	Substrate temperature during deposition
$U$	$\text{cm}^{-3} \text{ s}^{-1}$	Net carrier recombination rate (indices: see $\tau$ )
$v_{\text{th}}$	$\text{cm/s}$	Thermal carrier velocity

Symbol	Unit	Description
$V$	mV	Applied voltage
$V_{oc}$	mV	Open-circuit voltage
$W$	$\mu\text{m}$	Thickness of wafer or base

Acronym	Description
a-Si:H	Hydrogenated amorphous silicon
AM1.5G	Air mass 1.5 global
BSF	Back surface field
$\delta^+$ , $\delta^0$ , $\delta^-$	Charge states of dangling silicon bonds
EQE	External quantum efficiency
FZ	Float zone (silicon)
hli	High-level injection
HIT	Heterojunction with intrinsic thin layer
IQE	Internal quantum efficiency
lli	Low-level injection
MWPCD	Microwave-detected photoconductance decay
PECVD	Plasma enhanced chemical vapor deposition
QSSPC	Quasi steady-state photoconductance
SiN <sub>x</sub>	Hydrogenated amorphous silicon nitride
SRV	Surface recombination velocity
SRH	Shockley-Read-Hall



# List of publications

*Publications arising from the work in this thesis:*

## Refereed journal papers

1. H. Plagwitz, M. Nerding, N. Ott, H.P. Strunk, and R. Brendel, Low-temperature formation of local Al contacts to a-Si:H-passivated Si wafers, *Prog. in Photovolt.: Research and Applications* **12**, 47 (2004)
2. M. Schaper, J. Schmidt, H. Plagwitz, and R. Brendel, 20.1%-efficient crystalline silicon solar cell with amorphous silicon rear-surface passivation, *Prog. in Photovolt.: Research and Applications* **13**, 381 (2005)
3. H. Plagwitz and R. Brendel, Analytical model for the diode saturation current of point-contacted solar cells, *Prog. in Photovolt.: Research and Applications* **14**, 1 (2006)
4. P. Engelhart, S. Hermann, T. Neubert, H. Plagwitz, R. Grischke, R. Meyer, U. Klug, A. Schoonderbeek, U. Stute, and R. Brendel, Laser ablation of SiO<sub>2</sub> for locally contacted Si solar cells with ultra-short pulses, *Prog. in Photovolt.: Research and Applications*, in press, published online (2007)

## Refereed papers presented at international conferences

1. H. Plagwitz and R. Brendel, COSIMA technology for screen-printed point contacts to the rear of passivated Si solar cells, *Proceedings of the 14th International Photovoltaic Science and Engineering Conference*, 267 (2004)
2. H. Plagwitz, M. Schaper, J. Schmidt, B. Terheiden, and R. Brendel, Analytical model for the optimization of locally contacted solar cells, *Proceedings of the 15th IEEE Photovoltaic Specialists Conference*, 999 (2005)
3. H. Plagwitz, M. Schaper, A. Wolf, R. Meyer, J. Schmidt, B. Terheiden, and R. Brendel, 20%-efficient silicon solar cells with local contacts to the a-Si-passivated surfaces by means of annealing (COSIMA), *Proceedings of the 20th European Photovoltaic Solar Energy Conference*, 725 (2005)

4. H. Plagwitz, A. Wolf, B. Terheiden, and R. Brendel, A-Si:H passivation scheme for monocrystalline silicon thin-film solar cells applying the PSI-process, *Proceedings of the 15th International Photovoltaic Science and Engineering Conference*, 989 (2005)
5. H. Plagwitz, Y. Takahashi, B. Terheiden, and R. Brendel, Amorphous Si/SiN double layers: A low-temperature passivation method for diffused phosphorus as well as boron-emitters, *Proceedings of the 21st European Photovoltaic Solar Energy Conference*, 688 (2006)
6. P.P. Altermatt, H. Plagwitz, R. Bock, J. Schmidt, R. Brendel, M.J. Kerr, and A. Cuevas, The surface recombination velocity at boron-doped emitters: Comparison between various passivation techniques, *Proceedings of the 21st European Photovoltaic Solar Energy Conference*, 647 (2006)
7. P. Engelhart, N.-P. Harder, T. Neubert, H. Plagwitz, B. Fischer, R. Meyer, and R. Brendel, Laser processing of 22% efficient back-contacted silicon solar cells, *Proceedings of the 21st European Photovoltaic Solar Energy Conference*, 733 (2006)

## Patent application

1. R. Brendel and H. Plagwitz, Verfahren zur Herstellung eines Halbleiter-Metallkontaktes durch eine passivierte Siliziumoberfläche, *German patent application no. DE 10346469.7*



# Vielen Dank

all denen, die zum Gelingen dieser Arbeit beigetragen haben:

*Prof. Dr.-Ing. Rolf Brendel* für die hervorragende Betreuung dieser Arbeit erst am ZAE Bayern und später am ISFH, für viele hilfreiche Diskussionen und Anregungen sowie den Freiraum beim Ausgestalten der Arbeit;

*Prof. Dr. Michael Oestreich* für die freundliche Übernahme des Korreferats;

*Prof. Dr. Max Schulz* für die Möglichkeit meine Doktorarbeit am ZAE Bayern zu beginnen, sowie die Anstellung am Institut für Angewandte Physik der Universität Erlangen-Nürnberg;

*Dr. Barbara Terheiden* für die ausgezeichnete wissenschaftliche Betreuung, die vielen lehrreichen Diskussionen zu Physik und Technologie sowie das geduldige Korrekturlesen meiner Manuskripte;

*Dr. Rolf Stangl und Michael Kriegel* vom Hahn-Meitner Institut in Berlin, für die sehr schnelle Implementierung der QSSPC-Auswerteroutine in AFORS-HET und die umfassende Hilfe bei Fragen zum Programm; sowie *Dr. Lars Korte*, ebenfalls vom HMI, für das unkomplizierte Messen von Zustandsdichten;

meinen Mitdoktoranden und den Wissenschaftlern am ISFH, *Dr. Pietro Altermatt, Dr. Michael Bail, Robert Bock, Dr. Karsten Bothe, Dr. Peter Engelhart, Dr. Bernhard Fischer, Adnan Hammud, Dr. Nils-Peter Harder, Sonja Hermann, Jan Hensen, Renate Horbelt, Carmen Laveuwe, Dr. Gunter Müller, Dr. Peter Pohl, Klaus Ramspeck, Martin Schaper, PD Dr. Jan Schmidt und Andreas Wolf* für die kollegiale Zusammenarbeit und die vielen fruchtbaren Diskussionen über Photovoltaik und Physik im allgemeinen;

*Dr. Stefan Dauwe und Mihail Manole* für das Einführen der a-Si:H-Passivierung und der Bordiffusion am ISFH;

*Till Brendemühl, Lotte Ehlers, Renate Horbelt, Anja Lohse, Tobias Neubert, Sabine*

*Kirstein, Martin Schaper und Marita Steinhof* für ihre Hilfe beim Probenprozessieren sowie die Einführung in die Zellprozessierung am ISFH;

*Stefan Beisse, Gerwin Gross, Michael Weiß und Johannes Schlieker* vom Technik- und Werkstatt-Team am ISFH, für die kompetente Instandhaltung der Anlagen und Messtechnik sowie die schnelle Umsetzung meiner Skizzen in funktionierende Messtische;

*Astrid Kidzun, Richard Auer und Dr. Vladimir Gazuz* für die kollegiale Zusammenarbeit und die gute Stimmung am ZAE Bayern;

der *Interessengemeinschaft gemeinsames Forschen und Wohnen* für ihre Gastfreundschaft;

und allen anderen Kolleginnen und Kollegen am ZAE und ISFH für das angenehme und freundliche Arbeitsklima, und natürlich für die ISFH-Grillparties.

## Persönliche Daten

---

<b>Name</b>	Heiko Plagwitz
<b>Anschrift</b>	Rothenberger Str. 2, 90587 Obermichelbach
<b>Geburtsdatum</b>	03. Februar 1977
<b>Nationalität</b>	deutsch
<b>Familienstand</b>	ledig

## Schulbildung

---

<b>1983 - 1987</b>	Erich-Kästner Grundschule in Veitsbronn
<b>1987 - 1996</b>	Wolfgang-Borchert Gymnasium in Langenzenn Abschluss der allgemeinen Hochschulreife im Juni 1996

## Ersatzdienst

---

<b>Juli 1996 - Juli 2002</b>	Bayerisches Rotes Kreuz in Veitsbronn
------------------------------	---------------------------------------

## Universitätsausbildung

---

<b>Oktober 1996 - Juli 2002</b>	Friedrich-Alexander Universität Erlangen-Nürnberg Studium der Physik Diplomprüfung im Juli 2002
---------------------------------	--

## Anstellung

---

<b>August 2002 - September 2004</b>	Lehrstuhl für Angewandte Physik der Friedrich-Alexander Universität Erlangen-Nürnberg und Zentrum für Angewandte Energieforschung (ZAE) Bayern e.V., Abteilung Thermosensorik und Photovoltaik: Wissenschaftlicher Mitarbeiter
-------------------------------------	--

<b>seit Oktober 2004</b>	Institut für Solarenergieforschung (ISFH) Hameln/Emmerthal: Wissenschaftlicher Mitarbeiter im Bereich Silizium-Dünnschichtforschung
--------------------------	--